Karlsruhe Institute of Technology

Philip Scott

A Meta-Surface Optical Cavity for Enhancing Chiral Light-Matter Interactions

2024
Dissertation

A Meta-Surface Optical Cavity for Enhancing Chiral Light-Matter Interactions

Zur Erlangung des akademischen Grades eines
DOKTORS DER NATURWISSENSCHAFTEN (Dr. rer. nat.)
von der KIT-Fakultät für Physik des
Karlsruher Instituts für Technologie (KIT)

genehmigte

DISSERTATION

von

M. Phys. Philip Scott
geboren in Perth

Tag der mündlichen Prüfung: 07.02.2025
Referent: Prof. Dr. Martin Wegener
Korreferent: Prof. Dr. Carsten Rockstuhl

Contents

Publications

Parts of this thesis have already been published ...
... in scientific journals:

- **P. Scott**, X. Garcia-Santiago, D. Beutel, C. Rockstuhl, M. Wegener, and I. Fernandez-Corbaton, “On enhanced sensing of chiral molecules in optical cavities”, Applied Physics Reviews 7 (2020)
- **P. Scott**, M. Nyman, B. Zerulla, A. Franics Pérez Mellor, T. Bürgi, C. Rockstuhl, M. Wegener, and I. Fernandez-Corbaton, "A metasurface based microcavity for enhanced vibrational circular dichroism spectroscopy", in preparation

... at scientific conferences (only own presentations):

- **P. Scott**, X. Garcia-Santiago, D. Beutel, C. Rockstuhl, M. Wegener, and I. Fernandez-Corbaton, "A Simple All-Dielectric Metasurface-Based Cavity for Enhanced Sensing of Chiral Molecules", Metamaterials Congress (online), October 2020
- **P. Scott**, X. Garcia-Santiago, D. Beutel, C. Rockstuhl, M. Wegener, and I. Fernandez-Corbaton, "On enhanced sensing of chiral molecules in optical cavities", SPIE Photonics West (online), March 2021
- **P. Scott**, M. Nyman, B. Zerulla, A. Franics Pérez Mellor, T. Bürgi, C. Rockstuhl, M. Wegener, and I. Fernandez-Corbaton, "A metasurface based microcavity for enhanced vibrational circular dichroism spectroscopy", SPIE Photonics West United States of America, San Fransisco, January 2025 (Abstract accepted)

Additional related work has already been published ...
... in scientific journals:

- D. Beutel, **P. Scott**, M. Wegener, C. Rockstuhl, and I. Fernandez-Corbaton. "Enhancing the optical rotation of chiral molecules using helicity preserving all-dielectric metasurfaces" Applied Physics Letters 118, no. 22 (2021).
- Y. Chen, J.L. Schneider, M.F. Groß, K. Wang, S. Kalt, **P. Scott**, M. Kadic and M. Wegener, "Observation of Chirality-Induced Roton-Like Dispersion in a

3D Micropolar Elastic Metamaterial", Advanced Functional Materials 34, no. 20 (2024): 2302699.

- M. Nyman, X. Garcia-Santiago, M. Krstić, L. Materne, I. Fernandez-Corbaton, C. Holzer, **P. Scott**, M. Wegener, W. Klopper and C. Rockstuhl, "A digital twin for a chiral sensing platform" Laser & Photonics Reviews, p.2300967 (2024).
- Y. Chen, J. Schneider, K. Wang, **P. Scott**, S. Kalt, M. Kadic and M. Wegener, "Anomalous frozen evanescent phonons", Nature Communications, 15(1), 8882 (2024)

List of Figures

Chapter 1

1 Introduction

Chirality, stemming from the Greek word for hand, '*Χειρ*', can be defined as when an object is non-superimposable onto its mirror image through any translation or rotation transformation. The most common example of a chiral object is human hands, as seen in figure 1.1, which depicts two chiral objects in the macro- and microscale. The human hand being the macroscale object and thalidomide being the microscale chiral object. Lord Kelvin was the first to define the term chirality in 1894 in the second Robert Boyle Lecture by stating:

> *"I call any geometrical figure, or group of points, 'chiral', and say that it has chirality if its image in a plane mirror, ideally realised, cannot be brought to coincide with itself."*[1]

but was later refined by Lancelot Law Whyte [2, 3].

Chirality is present everywhere in nature, from chiral molecules to even the twist in spiral galaxies. Although, spiral galaxies are only considered to be chiral when coupled with the direction of their recession velocities [4]. It plays a fundamental role in nature, such as the spiral of the snail shells, where over 90 % have a left-handed spiral and the snails those that have a twist in their shell with the opposite handedness have trouble finding a mate [5]. Mantis shrimp also make use of chirality, who are able to sense circularly polarised light and use this polarised vision to help with hunting in the deep ocean [6, 7], and certain climber plants that have helical growth in their tendrils [8]. There is a chiral imbalance in nature, labelled as homochirality. An example of this chiral imbalance is in natural amino acids, where almost all of the amino acids are left-handed, and sugars are right-handed [9]. The underlying reasons for this chiral imbalance remain largely elusive [10, 11], although some speculate that a reason could be due the preference of one handedness of circularly polarised light emitted from stars and other celestial bodies [12].

Whereas Kelvin was the first to define the word chiral, a phenomenon related to chirality was recognised far prior to this. French scientists, François Arago and

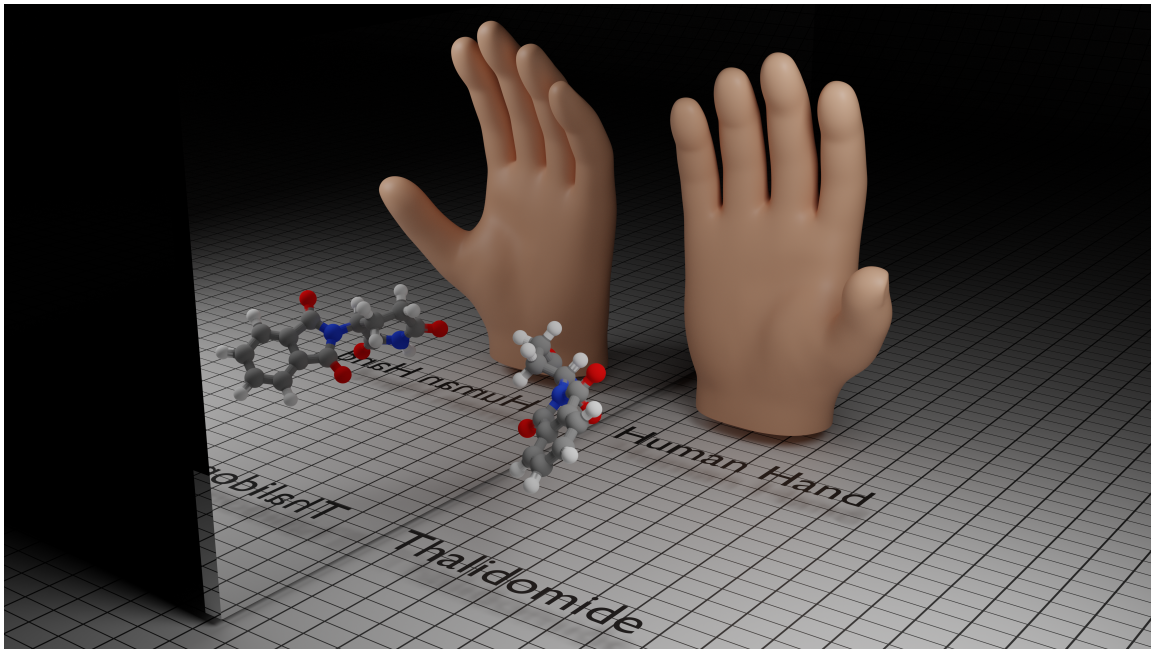

Figure 1.1: Illustration of chiral objects and their mirror image. A macroscale example of a human hand and a microscale example of a thalidomide molecule. Both examples cannot be made congruent with their mirror images by any rotation of translation. These illustrations are not to scale.

Jean-Baptiste Biot observed that quartz crystals [13–15] and natural compounds in solutions [14, 16] were able to rotate the plane of polarisation of linearly polarised light, which is known as optical rotary dispersion [17]. Shortly thereafter, the field of molecular chirality was discovered by Louis Pasteur through investigating the chemical and crystal structures of tartaric acid (TA) and paratarartic acid (PTA). His findings were that the crystals of the PTA contained both left- and right-handedness, therefore discovering the first racemic mixture of chiral molecules.

In molecular chirality, one is interested in the handedness of the molecules, which are known as enantiomers. From Pasteur's work, it is known that the handedness of a molecule can cause some differing properties from it's mirror-image. An example would be the left-handed crystal of tartaric acid (S-TA), with S standing to *Sinsiter* and meaning left in Latin and the right-handed crystal (R-TA), with R standing for *Rectus* meaning right in Latin [18]. Some scientific fields use the naming convention of dextral and sinistral, meaning left and right respectively to describe the different handedness of the chiral objects. Apart from their differences with interacting with light, some chiral molecules also have differing chemical or toxicological properties [19, 20]. For example, Thalidomide is a drug that was used to help treat nausea and morning sickness in pregnant women.

While one handedness of the drug in fact had this effect, the other handedness was teratogenic, meaning that it caused birth defects in newly born babies [21]. Limonene is also a chiral molecule where (S)-Limonene has an piney odour and can be found in caraway and bergamot orange plants. (R)-Limonene, however, is more common than it's mirror-image isomer. It is responsible for the scent and flavour of orange and is found in citrus fruits. Incidentally, since we can perceive the difference in sent between the two isomers of Limonene, the olfactory receptors in our noses are chiral [22]. This is because chiral objects show a fascinating property: they interact differently with other chiral objects depending on their handednesses, but will interact identically with an achiral object.

In 1817, Augustin-Jean Fresnel, although mostly known for his laws describing reflection and transmission of plane waves [23], discovered circularly polarised light (CPL). He discovered CPL by projecting linearly polarised light at 45° through a glass prism that he designed himself [24]. As discussed in which chiral objects have different interactions with other chiral objects depending on their handedness, there is no exception with chiral molecules and chiral light. Circular dichroism (CD) is the differential absorption between left- and right-handed CPL by a chiral molecule. Similarly, as with optical rotary dispersion, this can be used to determine the handedness of a chiral molecule, depending on the sign of the CD signal. Although the signal for CD and ORD is typically very weak as a result of the subtle differences between the chiral molecules and the light, it requires long interaction times and large sample sizes.

This naturally weak signal, combined with the importance in medical use to be able to quickly and accurately determine the handedness of the isomer, much interest in recent years has gone into enhancing the signal without changing the sample size or measurement times. In an attempt to resolve this issue, there have already been many published methods of plasmonic and dielectric structures tailored with the goal of enhancing the CD signal [25–62]. However, many of these presented methods only produce high enhancement in very small regions in the near-field to the structures, typically less than 1 µm from the structures. When trying to enhance the CD signal of a normal volume of chiral analyte, the volume averaged enhancement would tend towards one. Therefore, an intriguing route would be to have an enhancement over a large volume of the chiral analyte.

The basis of this work is therefore on enhancing the signal from chiral molecules but with a slightly different approach: Instead of resonant structures to enhance the signal only in the near field resonances, this approach is based on a helicity preserving cavity constructed of a diffracting array acting as one of the cavity mirrors, and the other being a plain mirror. At the time of conducting this work and writing this dissertation, no reports of such a method for enhancing the circular dichroism enhancement is available in literature to my knowledge. The

experimental realisation of such a method would have signification implications for the pharmaceutical industry, enabling more precise determination of the handedness, or enantiomeric excess of a chiral drug [63]. The mirrors are separated by a distance on the scale of tens of micrometers and can be fine-tuned with a resolution of less than 50 nm through the use of three piezoelectric actuators in a triangular formation. The cavity is designed to work in the mid-infrared wavelength regime, and the diffracting array parameters can vary targeting different vibrational CD (VCD) resonances in the molecules. Previous theoretical work on this method has already been published [51, 64–66]. In contrast to the previously published methods on CD enhancement, this design also has large local enhancements not only in the near field to the structures but also in the far field, allowing for a interactions with a large volume of chiral analyte.

Outline of this Thesis

This thesis is outlined as follows: starting with chapter 2, I will explain the fundamental concepts that allows the reader to follow the discussions in the following chapters. I begin by introducing Maxwell's equations and cover the topics of electromagnetic wave propagation and the polarisation states of such waves. Following, there is a discussion of diffraction from a two dimensional array and how the polarisation states of light can be preserved through diffraction. The chapter concludes with a discussion on chiroptical effects and the mechanism behind them.

In chapter 3, I provide an insight into the theory behind the optical cavities that are presented to enhance the circular dichroism signal. I start with a brief introduction of structures that have been employed for circular dichroism enhancement and their limitations. I continue the discussion to the two cavity configurations and their principles of operation and compare the enhancing capabilities of the two cavity configurations and address the design considerations that were taken into account when altering the cavity design from the original. The chapter is concluded by a detailed description of how the simulations are brought in line with the experimental measurements through implementation of realistic parameters of the materials used and discuss the implications this has for the enhancement capabilities of the cavity.

In chapter 4, I recall the experimental methods employed in this work. The methods used for the fabrication of the silicon cylinder arrays are described in detail. The optimisation procedures employed for each step to ensure high quality structures are shown. Furthermore, the custom microfluidic chamber that was designed and fabricated to house the optical cavity is shown as well as the entire mircofluidic setup used in the experiments. Finally, the experimental setup and

procedure used for measuring the circular dichroism signal of chiral molecules in the chamber is explained in detail.

In chapter 5, the experimental results for the circular dichroism enhancing cavity are presented. There is first a discussion on the CD artefacts produced by the diffracting arrays and cavities through various misalignments. Following are the circular dichroism measurements performed on a series of concentrations of the chiral molecule 1,1'-Bi-2-naphthol (BINOL) in both a plain cavity and the enhancing cavity are presented and discussed. The chapter is concluded with a discussion of the results.

In the final chapter, chapter 6, I summarise the results of this thesis and give an outlook into the possible steps forward on optical cavities for the enhancement of chiroptical signals.

Chapter 2

2 Electromagnetic Waves and Light-Matter Interactions

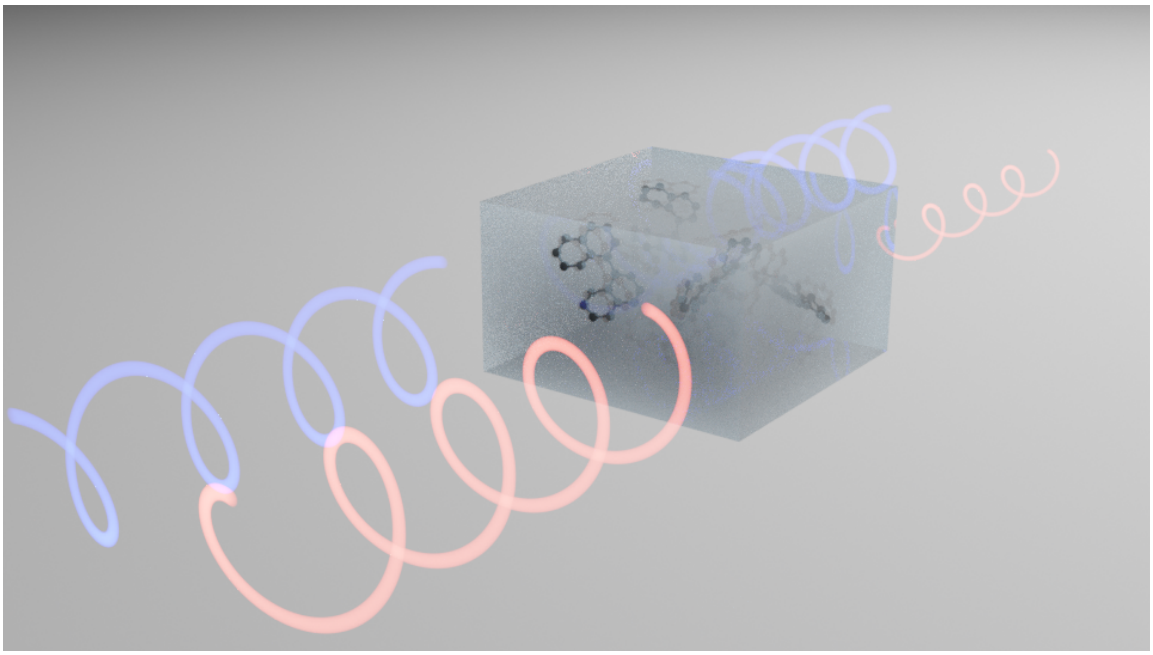

Artistic representation of the differential absorption of circularly polarised light by a solution of chiral molecules

In this chapter, I will describe and explain the fundamental concepts that are required for the reader to follow the work in the following chapters. I begin by starting with the basic concepts of electromagnetic waves, which are described by Maxwell's equations in their macroscopic form, and describing the different polarisation states of light. Using Maxwell's equations, I will derive the wave equation for light in homogeneous media and detail how light interacts with matter through reflection, transmission and absorption. Finally, I will discuss chiroptical activity, explaining the two different methods that can be applied for the detection of chiral molecules.

2.1 Electromagnetic Waves

Electromagnetic waves are the backbone of the work that will be shown in this thesis, from the fabrication of the silicon cylinder arrays to the probing of the chiral molecules relies on electromagnetic waves. The section begins with the description of EM waves through Maxwell's equations, following with explaining the three polarisation states of light defined through the electric field vectors. The contents of this section, including the derivations and statements can be found in many textbooks on optics and photonics [67–69].

2.1.1 *Maxwell's Equations*

The four equations that can be used to explain almost all of classical electromagnetic theory are Maxwell's equations, in their most common form that was derived by Oliver Heaviside [70, 71]. These equations form a relationship between electric and magnetic fields, and can be used to explain the propagation of electromagnetic waves in matter. Together with the Lorentz force law, these form the foundations of classical electromagnetism.

The first of four equations is Gauss's law, which outlines how the electric field relates the distribution of external charges. Gauss's law in its differential form is:

$$\nabla \cdot \mathbf{E}(\mathbf{r}, t) = \frac{\rho(\mathbf{r}, t)}{\epsilon_0}, \tag{2.1}$$

where $\mathbf{E}$ is the electric displacement field and ρ is the electric charge density and $\epsilon_0 \approx 8.854 \cdot 10^{-12}$ Fm^{-1} is the electric permittivity of free space. Similarly to Gauss's law for electric fields, the second of Maxwell's equations is Gauss's law of magnetism, which states that the magnetic flux through any closed surface is equal to zero.

$$\nabla \cdot \mathbf{B}(\mathbf{r}, t) = 0. \tag{2.2}$$

Here, $\mathbf{B}$ is the magnetic flux density. The third equation is Faraday's law of induction and this states that temporal change in the magnetic field will induce an electric field. This law can be written as:

$$\nabla \times \mathbf{E}(\mathbf{r}, t) = -\frac{\partial \mathbf{B}(\mathbf{r}, t)}{\partial t}, \tag{2.3}$$

with $\mathbf{E}$ being the electric field. Finally, the fourth equation is the Ampère-Maxwell law states that a magnetic field can be induced by either a changing electric field or an external current density. The Ampère-Maxwell law is

$$\nabla \times \mathbf{H}(\mathbf{r}, t) = \mathbf{j}(\mathbf{r}, t) + \frac{\partial \mathbf{D}(\mathbf{r}, t)}{\partial t}, \tag{2.4}$$

where **H** is the magnetic field and **j** is the current density. Now we have the complete set of Maxwell's equations. Now we want to look into how the electromagnetic waves propagate in some medium. Firstly, I will look at the simple case of a linear isotropic medium and how the light interacts at an interface between two media. In a later section, a more complicated case which is wave propagation in bianisotropic media will be looked into.

2.1.2 *Wave Propagation in Media*

In this work, the media in question will be free of external currents or charges, therefore $\mathbf{j}(\mathbf{r},t)$ and $\rho(\mathbf{r},t)$ are set to 0. Furthermore, this work only deals with linear isotropic media, where $\mathbf{D}(\mathbf{r},t)$ and $\mathbf{E}(\mathbf{r},t)$ are related through $\mathbf{D}(\mathbf{r},t) = \epsilon\mathbf{E}(\mathbf{r},t)$, where $\epsilon = \epsilon_r\epsilon_0$. ϵ_r is the relative permittivity of the material and ϵ_0 is the permittivity of free space. and $\mathbf{B}(\mathbf{r},t)$ and $\mathbf{H}(\mathbf{r},t)$ are related through $\mathbf{B}(\mathbf{r},t) = \mu\mathbf{H}(\mathbf{r},t)$, where μ is the magnetic permeability of the medium, and is related to the permeability of free space through $\mu = \mu_r\mu_0$ where μ_r is the relative permeability and $\mu_0 = 4\pi \cdot 10^{-7}$ Hm^{-1}.

Using these constitutive relations for linear media, and converting these equations to the frequency domain, which is more applicable for this work, we can reduce the Maxwell's equations above to the following form which also includes the response of the material that the electromagnetic waves are propagating in.

$$\begin{aligned} \nabla \cdot \mathbf{D}(\mathbf{r},\omega) &= 0, \\ \nabla \cdot \mathbf{B}(\mathbf{r},\omega) &= 0, \\ \nabla \times \mathbf{E}(\mathbf{r},\omega) &= i\omega\mathbf{B}(\mathbf{r},\omega), \\ \nabla \times \mathbf{H}(\mathbf{r},\omega) &= -i\omega\mathbf{D}(\mathbf{r},\omega). \end{aligned} \tag{2.5}$$

It is worth noting that this work is focused on chirality and how light interacts with chiral media. For chiral media, the constitutive relations will have additional terms to properly describe this interaction and will be discussed in section 2.3

From the reduced forms of the Maxwell's equations above, we can take the third and fourth equations and for any set frequency, ω_0, the wave equations for the electric and magnetic field in a medium in the time domain can be derived to be:

$$\begin{aligned} \left(\nabla^2 + \frac{\omega^2}{c^2}\right)\mathbf{E}(\mathbf{r},\omega) &= 0, \\ \left(\nabla^2 + \frac{\omega^2}{c^2}\right)\mathbf{B}(\mathbf{r},\omega) &= 0, \end{aligned} \tag{2.6}$$

where c is the speed of light in a medium and is defined as $c(\omega_0) = 1/\sqrt{\epsilon(\omega_0)\mu(\omega_0)}$. The refractive index of the material $n(\omega_0)$ can also be deduced from this relation

as $n(\omega_0) = \sqrt{\epsilon(\omega_0)\mu(\omega_0)}$. The speed of light in vacuum and the speed of light in a medium is related through the refractive index of the medium:

$$c(\omega_0) = \frac{1}{\sqrt{\epsilon_r(\omega_0)\mu_r(\omega_0)\epsilon_0\mu_0}} = \frac{c_0}{\sqrt{\epsilon_r(\omega_0)\mu_r(\omega_0)}} = \frac{c_0}{n(\omega_0)}. \tag{2.7}$$

Since that we have introduced the constitutive relations of the material and derived the wave equations for the **E** and **B** field we can solve the wave equations using plane waves of the form

$$\begin{aligned} \mathbf{E}(\mathbf{r}, t) &= \mathbf{E}_0 e^{i(\mathbf{k}\cdot\mathbf{r} - \omega_0 t)}, \\ \mathbf{B}(\mathbf{r}, t) &= \mathbf{B}_0 e^{i(\mathbf{k}\cdot\mathbf{r} - \omega_0 t)}, \end{aligned} \tag{2.8}$$

where **k** is the wave vector. Inserting the plane wave function for the electric field into the wave equation for the electric field and solving this will produce the dispersion relation of the wave:

$$\omega = \frac{c_0|\mathbf{k}|}{n(\omega)}. \tag{2.9}$$

Here, **k** is the wave vector of the plane wave and defines the direction of propagation. Furthermore, from this dispersion relation, it is possible to calculate the group velocity v_g, and the phase velocity v_p of the EM wave, providing the permittivity and permeability of the medium is known. The group velocity and phase velocity are

$$\begin{aligned} v_g &= \frac{\partial\omega}{\partial k}, \\ v_p &= \frac{\omega}{k}. \end{aligned} \tag{2.10}$$

Now the Maxwell's equations in linear isotropic media have been introduced and derived the wave equations, we will now look at how electromagnetic waves act when encountering an interface between two media. Investigating this phenomenon will introduce us to Fresnel's reflection and transmission coefficients, which are dependent on the polarisation and angle of incidence. The importance of this dependency of the reflection and transmission coefficients in this work is because large angles of incidence can cause the handedness of circularly polarised light to be preserved on reflection. Additionally, a discussion on the polarisation states of light will follow in the next section.

Firstly we consider that the wave originates and propagates in the first dielectric medium with properties n_1, ϵ_1, and μ_1 towards the boundary with the second dielectric medium with properties n_2, ϵ_2, and μ_2. Let the wave propagate towards

the interface at an angle of incidence, θ_i, where the angles, θ are always defined as the angle between the normal of the interface and the direction of propagation of the wave, i.e. the wave vector $\mathbf{k}$. Simply, through the law of reflection and Snell's law, we can determine the angle of reflection θ_r and the angle of transmission θ_t.

$$\theta_r = \theta_i, \qquad \theta_t = \sin^{-1}\left(\frac{n_1}{n_2}\sin(\theta_i)\right). \tag{2.11}$$

Again, if we take the incoming electric field of the form of a plane wave ansatz in equation 2.8, we can calculate the reflected and transmitted electric fields from the incidence field using Maxwell's equations. These three fields are defined as:

$$\begin{aligned} \mathbf{E}_{in}(\mathbf{r},\omega) &= \mathbf{E}_{0in}e^{i(\mathbf{k}\cdot\mathbf{r}-\omega t)}, \\ \mathbf{E}_{r}(\mathbf{r},\omega) &= \mathbf{E}_{0r}e^{i(\mathbf{k}\cdot\mathbf{r}-\omega t)}, \\ \mathbf{E}_{t}(\mathbf{r},\omega) &= \mathbf{E}_{0t}e^{i(\mathbf{k}\cdot\mathbf{r}-\omega t)}, \end{aligned} \tag{2.12}$$

with *in* specifying the incident field, r the reflected field and t the transmitted field. $\mathbf{E}_{0in}$, $\mathbf{E}_{0r}$ and $\mathbf{E}_{0t}$ are the amplitudes of the incident, reflected and transmitted waves respectively. As previously stated, the reflection and transmission coefficients of the waves are dependent on the polarisation of the wave, namely the polarisation parallel and perpendicular to the plane of incidence. The subscripts for the polarisations that we will use here are $\parallel$ to denote the polarisation plane that contains both the wave vector and the normal to the interface, the parallel polarisation, and we will use $\perp$ to denote the perpendicular polarisation. Another notation that is used commonly are the p- and s-polarisations. The notation p meaning parallel and s meaning *senkrecht*, which is the German word for perpendicular.

Now we can continue to calculate the reflection and transmission coefficients. These can be calculated through Maxwell's equations at the interface between the two media. The reflection and transmission coefficients are

$$\begin{aligned} r_{\parallel} &= \left(\frac{\mathbf{E}_r}{\mathbf{E}_i}\right)_{\parallel} = \frac{n_2\cos(\theta_i) - n_1\cos(\theta_t)}{n_2\cos(\theta_i) + n_1\cos(\theta_t)}, \\ t_{\parallel} &= \left(\frac{\mathbf{E}_t}{\mathbf{E}_i}\right)_{\parallel} = \frac{2n_1\cos(\theta_i)}{n_2\cos(\theta_i) + n_1\cos(\theta_t)}, \end{aligned} \tag{2.13}$$

and

$$\begin{aligned} r_{\perp} &= \left(\frac{\mathbf{E}_r}{\mathbf{E}_i}\right)_{\perp} = \frac{n_2\cos(\theta_i) - n_1\cos(\theta_t)}{n_2\cos(\theta_i) + n_1\cos(\theta_t)}, \\ t_{\perp} &= \left(\frac{\mathbf{E}_t}{\mathbf{E}_i}\right)_{\perp} = \frac{2n_1\cos(\theta_i)}{n_2\cos(\theta_i) + n_1\cos(\theta_t)}. \end{aligned} \tag{2.14}$$

In simple terms, the reflection and transmission coefficients are just the ratio between the transmitted or reflected field to the incident field. A special case for the coefficients is for normal incidence. In this case, the magnitude of the reflection and transmission coefficients become equal and independent of the polarisation. The total reflectance and transmittance in this case would then be

$$\begin{aligned} R &= r^2 = \left(\frac{n_2 - n_1}{n_1 + n_2}\right)^2, \\ T &= \frac{n_2}{n_1} t^2 = \frac{4 n_1 n_2}{(n_1 + n_2)^2}. \end{aligned} \tag{2.15}$$

Another important case for this work is when the angle of incidence is at near grazing angles of incidence. Firstly we need to make some statements and some slight changes to the notation that is used here. We then relate the perpendicular and parallel polarisations to the transverse electric (TE) and transverse magnetic (TM) polarisations respectively. Then, again using Snell's law, we can express the reflection coefficients of the TE and TM polarisations in terms of the refractive indicies of the two media and only the angle of incidence [72].

$$\begin{aligned} r_{TE} &= \frac{n_1 \cos(\theta_i) - \sqrt{n_2^2 - n_1^2 \sin^2(\theta_i)}}{n_1 \cos(\theta_i) + \sqrt{n_2^2 - n_1^2 \sin^2(\theta_i)}}, \\ r_{TM} &= \frac{n_2^2 \cos(\theta_i) - n_1 \sqrt{n_2^2 - n_1^2 \sin^2(\theta_i)}}{n_2^2 \cos(\theta_i) + n_1 \sqrt{n_2^2 - n_1^2 \sin^2(\theta_i)}}. \end{aligned} \tag{2.16}$$

As this work is on the measurement of CD, which again is the differential absorption between the two handednesses of circularly polarised light, before continuing, a couple of concepts need to be introduced. The first being circularly polarised light, which can be defined when the resultant electric field draws out a spiral in space and depending on the direction of this spiralling, it can be assigned a handedness. This will be described in more detail in the following section. Within a CD measurement, the handedness of the light needs to remain the same throughout the measurement otherwise it can lead to degradation of the signal. Within a standard Fabry-Pérot optical cavity, the light is usually incident at an angle normal to the mirror, and this is reflection results in a complete flip of the handedness, which is entirely unwanted for CD measurements. To circumvent this, a solution that the handedness of the light is not flipped on reflection is required. The following paragraphs explain how this can be achieved and how this is implemented into a cavity design is described in chapter 3.

What we want to show with these two equations is that if a circularly polarised wave were to impinge on the interface between the two dielectric media, the

helicity will be mostly preserved on near-grazing angles of incidence. For the limit of grazing incidence $\theta_i \to 90°$, both the reflection coefficients for the TE and TM polarisations tend towards -1. But how does this relate to the helicity of the light being preserved? The helicity of circularly polarised light can be defined as the decomposition between the electric and magnetic fields, connected through the Riemann-Silberstein vectors and the impedance of the medium that the are propagating in. This description of the helicity of light will be explained in more detail in the next section. For now, we define the helicity component of the EM wave as $\mathbf{G}$ and it's relation to the $\mathbf{E}$ and $\mathbf{H}$ fields are:

$$\mathbf{G}_{\pm}(\mathbf{r},\omega) = \frac{1}{\sqrt{2}}[\mathbf{E}(\mathbf{r},\omega) \pm iZ(\omega)\mathbf{H}(\mathbf{r},\omega)], \tag{2.17}$$

where $Z(\omega) = \sqrt{\mu(\omega)/\epsilon(\omega)}$ is the frequency dependent impedance of the medium that the wave is propagating in and the notation $\pm$ defines whether the wave is left-handed $(+)$ or right-handed $(-)$. Now we will show why the reflection coefficients tending towards -1 results in helicity conservation on reflection. We can define the complete reflected electric field in terms of the helicity component of the fields and the reflection coefficients:

$$\mathbf{E}_r(\mathbf{r},\omega) = \frac{1}{2}(r_{TE} + r_{TM})\mathbf{G}_{\pm}(\mathbf{r},\omega) + \frac{1}{2}(r_{TE} - r_{TM})\mathbf{G}_{\mp}(\mathbf{r},\omega). \tag{2.18}$$

The first part of the right hand side of the equation relates to the helicity preserved component and the second part relates to the helicity flipped components, therefore we can assign these a helicity conserved and helicity flipped parameter.

$$\begin{aligned} h_c &= \frac{1}{2}(r_{TE} + r_{TM}), \\ h_f &= \frac{1}{2}(r_{TE} - r_{TM}). \end{aligned} \tag{2.19}$$

Simply inputting the values for r_{TE} and r_{TM} for when the angle tends to grazing incidence, we find that the conserved component tends to -1 and the flipped component tends to 0, proving that helicity is preserved on grazing incidence reflections. It is also worth nothing that this result is completely independent of the material parameters. consequently, on normal incidence, the helicity conserved coefficient becomes 0 while the helicity flipped coefficient becomes a maximum, which results in a complete flip in helicity on reflection at normal incidence.

2.1.3 Polarisation States of Light

Now that I have introduced Maxwell's equations, solved the wave equations for light travelling in linear dielectric media and finally shown how the Fresnel reflection and transmission coefficients can explain what happens with electromagnetic

waves when they interact with a boundary between two dielectric media. We proved that for grazing angles of incidence the helicity of light can be preserved. Now we will look into the polarisation states of light, which have already been briefly mentioned in the previous section.

For definitions, we will again use the plane wave solution of an electric field to the Maxwell's equations, shown in equation 2.8, but now including the phase ϕ, of the wave.

$$\mathbf{E}(\mathbf{r}, t) = E_0 e^{i(\mathbf{k}\cdot\mathbf{r} - \omega_0 t + \phi)}, \tag{2.20}$$

We also know from Maxwell's equations that the direction of propagation is perpendicular to the direction of oscillation of the **E** field. Using this, we can define the propagation direction of the wave vector **k** as

$$\mathbf{k} = |\mathbf{k}|\hat{e}_z. \tag{2.21}$$

Then it is possible to write the vectors of the electric field, **E** as a combination of the polarisation vectors in the x and y planes as so:

$$\mathbf{E} = E_{0x}\hat{e}_x + E_{0y}\hat{e}_y. \tag{2.22}$$

Now we almost have all of the information that we need to be able to define the polarisation states. A polarisation state of light is essentially the combination of the ratio of amplitudes of the moduli of the field vectors and the differences in phase between the two electric field vectors in the x and y planes $\Delta\phi = \phi_y - \phi_x$, so the final piece of information we need is the complex coefficients of these electric field vectors in these planes, which are dependent on the phase. The complex coefficients of the electric field vectors are $E_{0x} = |E_{0x}|e^{i\phi_x}$ and $E_{0y} = |E_{0y}|e^{i\phi_y}$.

Linear Polarisation

The first polarisation state that we will look at is linear polarisation. Linear polarisation is often defined as the s- and p-polarisation states or in TE and TM polarisations as stated in the previous section. If $\mathbf{E}_{0x}$ and E_{0y} have the same phase, i.e. $\Delta\phi = 0$, then the resulting wave is a linearly polarised wave with a polarisation vector at a 45° angle, given that E_{0x} and $\mathbf{E}_{0y}$ are of equal magnitude. The angle of which the linearly polarised wave will propagate is defined through the ratio of the two amplitudes, $\theta = \tan^{-1}(E_{0y}/E_{0x})$ This polarisation state can be seen in Figure 2.1. Linear polarisation is also the resultant polarisation state when $\Delta\phi = \pm 2n\pi$ or $\pm(2n+1)\pi$ where n is a positive integer. The electric field for a linearly polarised wave can be written as:

$$\mathbf{E} = (E_{0x}\hat{e}_x + E_{0y}\hat{e}_y)e^{i(\mathbf{k}\cdot\mathbf{r} - \omega t + \phi)}, \tag{2.23}$$

where ϕ is an arbitrary phase of the linearly polarised wave.

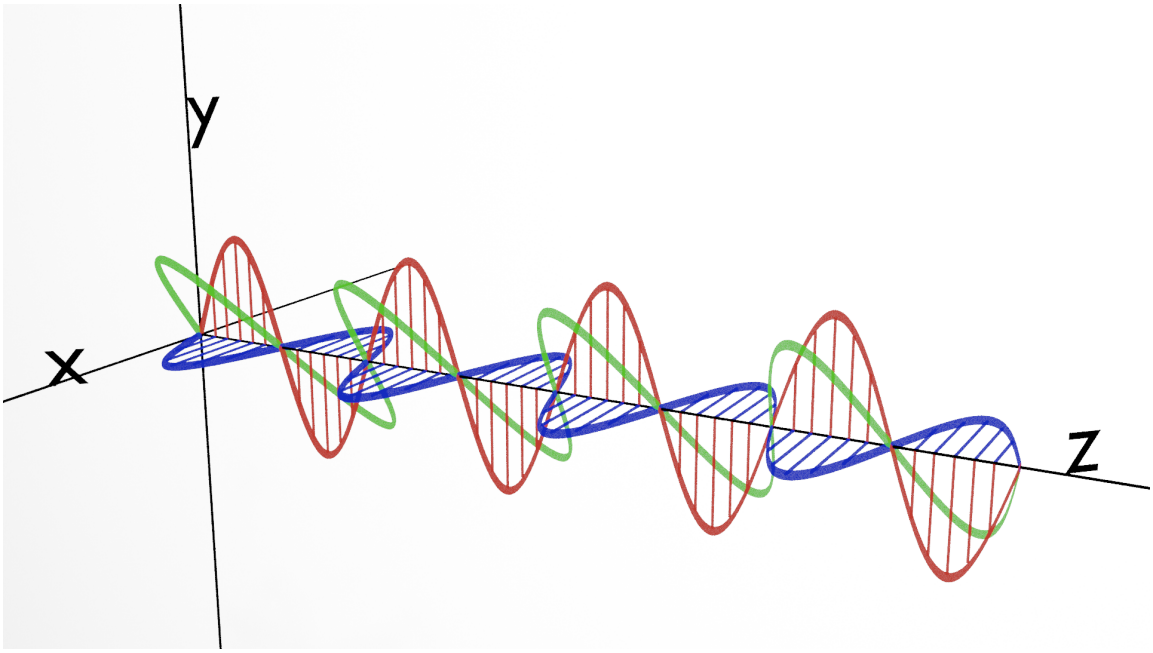

Figure 2.1: Depiction of linearly polarised light. The electromagnetic wave propagates in the $+z$ direction. For linearly polarised light, the electric field vectors in the x and y planes have equal amplitude and phase.

Circular Polarisation

Now we will define the polarisation state for circular polarisation, or circularly polarised light (CPL). A wave becomes circularly polarised when the amplitudes are equal and the phase difference between the fields in the x and y planes are equal to $\pm\pi/2$. Again, the electric field can be defined for circular polarisation as:

$$\mathbf{E} = (\hat{e}_x \pm i\hat{e}_y)E_0 e^{i(\mathbf{k}\cdot\mathbf{r}-\omega t+\phi)}, \tag{2.24}$$

where E_0 is the homologous amplitude, $E_0 = E_{0x} = E_{0y}$. If we take the real parts of equation 2.24, we can obtain the components of the electric field in the x and y planes

$$\begin{aligned} \mathbf{E}_x &= E_0 \cos(\mathbf{k}\cdot\mathbf{r} - \omega t + \phi), \\ \mathbf{E}_y &= \mp E_0 \sin(\mathbf{k}\cdot\mathbf{r} - \omega t + \phi), \end{aligned} \tag{2.25}$$

with ϕ again being the arbitrary phase. When we look at these electric field vectors, for a fixed point in space, these vectors will trace out a circle in time with a frequency of ω. If we take the positive sign for the second equation in 2.25 the circle that is traced out will be rotating in a clockwise direction when viewed from the source, or also denoted as right-handed circularly polarised light.

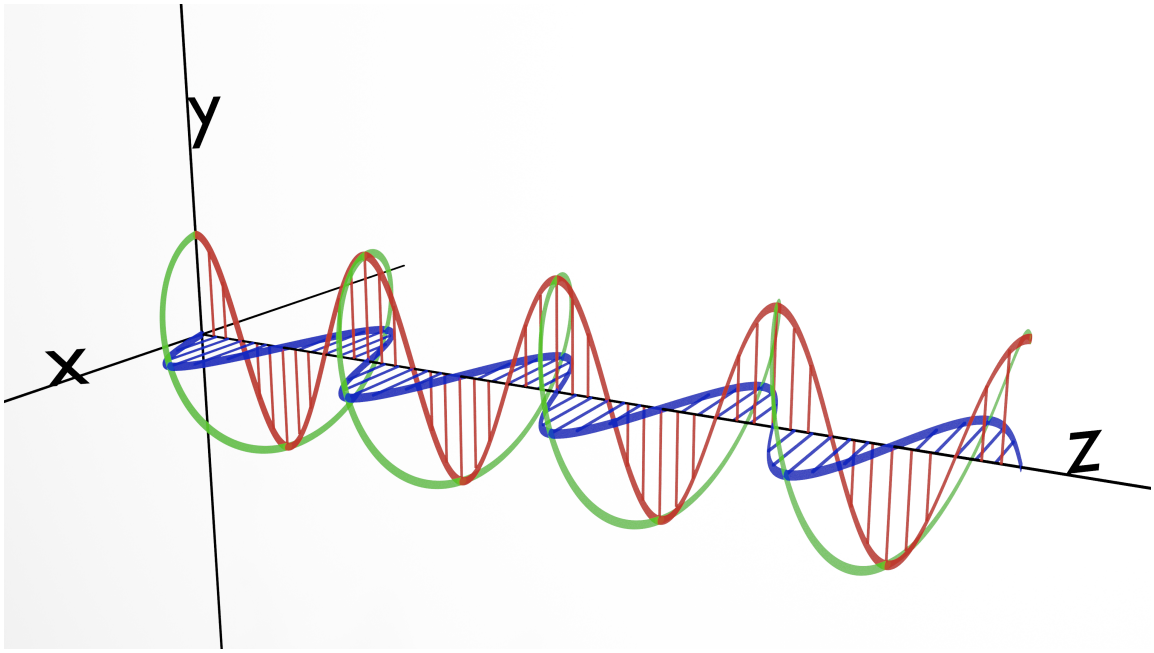

Figure 2.2: Depiction of circularly polarised light. The electromagnetic wave propagates in the $+z$ direction. For linearly polarised light, the electric field vectors in the x and y planes have equal amplitude but a phase difference of $\pi/2$.

Contrary, if we take the negative sign from the same equation, the circle will rotate in a counter-clockwise direction when viewed from the same direction, also named left-handed circularly polarised light. There is another notation for the handedness of CPL that will be referenced in this work. This notation is the helicity basis, where left-handed CPL has positive helicity and right handed CPL has negative helicity. It is also worth noting that the naming of such handedness of CPL can differ depending on where the observed is placed, for example when the observer is placed along the positive z axis, the handedness of the light with be flipped. While this is important to note, this work will only deal with the observer source, following suite with this observer point from [69]. Figure 2.2 illustrates right-handed CPL propagating along the $+z$ axis with at a fixed point in time.

Elliptical Polarisation

When neither of the conditions for linear or circular polarisation are met as discussed above, then the resulting polarisation will be elliptical. For a fixed point in time, the resulting electric field vector will draw out an ellipse along the z-axis, as depicted in Figure 2.3. Elliptical polarisation is an important concept in circular dichroism as it quantifies how elliptical the polarisation of the light has become due to the differential absorbance.

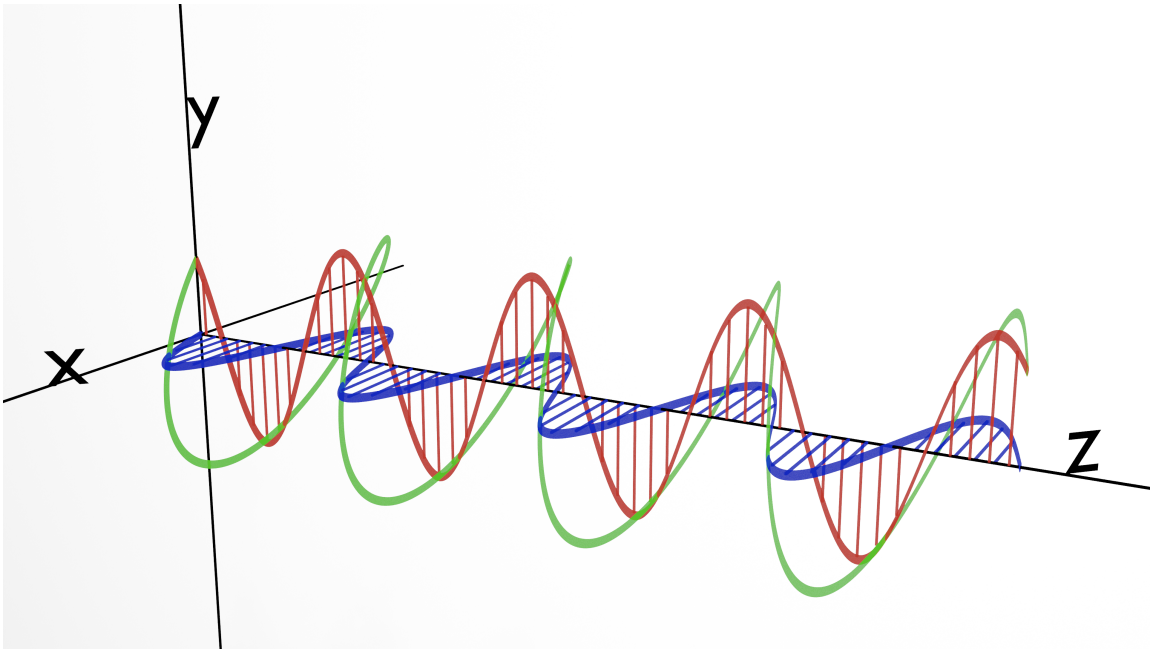

Figure 2.3: Depiction of elliptically polarised light. The electromagnetic wave propagates in the $+z$ direction. Light is considered to be elliptically polarised when neither of the conditions for linear or circular polarisations are met.

Riemann-Silberstein Vectors

As stated in the description of circularly polarised light, the handedness of the CPL can be denoted by the helicity basis, with ± 1 being CPL waves of pure helicity. These waves can also be described by the Riemann-Silberstein vectors. The Riemann-Silberstein vector formalism takes the form as in equation 2.17 where it encapsulates both the electric and magnetic field into a single form. For this work, we will use this formalism to describe the chirality properties of light. The optical chirality density of light can be described using the following relation

$$C = \frac{1}{2}\left(\epsilon_0 \mathbf{E} \cdot (\nabla \times \mathbf{E}) + \frac{1}{\mu_0}(\mathbf{B} \cdot \nabla \times \mathbf{B})\right). \tag{2.26}$$

The optical chirality density can also be written in terms of the Riemann-Silberstein vectors as so

$$C = \frac{\epsilon_0 \omega}{8 c_0}\left(|\mathbf{G}_+|^2 - |\mathbf{G}_-|^2\right), \tag{2.27}$$

then it can be see, that when the two Riemann-Silberstein vectors for the opposite helicities have a larger difference, the greater the optical chirality becomes. A maximum would be when there is only components of either $+$ or $-$ helicity [73].

2.2 Diffraction Theory

The previous section introduced electromagnetic waves, the propagation of such waves in a homogeneous medium including the wave equation and also the three polarisation states of light which were defined through the phase difference and the amplitudes of the electric field vectors. This section will go more in depth into how light interacts with matter. Firstly we will look at the theory of diffraction and the diffraction from 2-dimensional periodic structures. Next, a short description of how the helicity of light can be preserved when light is scattered from such structures. Finally, methods for the enhancement of light-matter interactions are discussed.

2.2.1 *Diffraction from a Two-Dimensional Array*

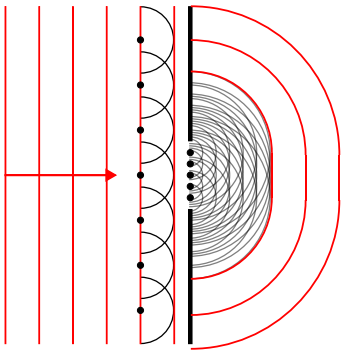

Figure 2.4: A simple illustration of the diffraction of light through a gap in a object as explained using the Huygens-Fresnel principle of light waves.

Diffraction of light is when a light wave propagates towards an object which has a gap in it that is smaller than the wavelength of the wave. A simple, classical description of diffraction is through the Huygens-Fresnel principle, as illustrated in Figure 2.4. The Huygens-Fresnel principle states that every point of a wavefront of light is a source of secondary spherical wavelets that travel at the same speed as the wave. At some later point in time, thought the interaction of these secondary wavelets form a new wavefront. Again, when this wavefront encounters an aperture or gap in some obstacle, some of these wavelet sources will be blocked by the object and some will propagate forward. Following the propagation of the wavelets that are allowed to propagate, they will then from a wavefront that begins to bend around the gap.

Detouring from the simple descriptions of diffraction, which explanations can be found in the following literature: [69, 72, 74]. This work will look into diffraction from 2-dimensional periodic arrays. We can define a periodic structure through its lattice vectors which can be described by its Bravais lattice [75]. The lattice vectors

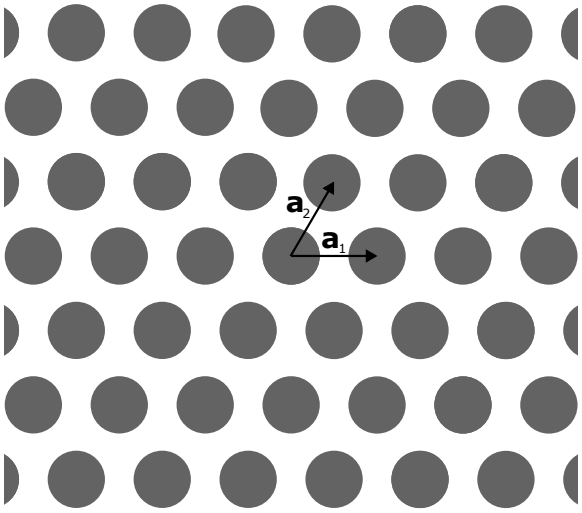

Figure 2.5: Real lattice of a periodic hexagonal array with primitive lattice vectors $|\mathbf{a}_1| = |\mathbf{a}_2| = a$. Both primitive lattice vectors for a hexagonal lattice are of equal lengths and can be separated by an angle of 60° or 120°

for a hexagonal array, which is the diffracting arrays that will be used in this work are

$$|\mathbf{a}_1| = |\mathbf{a}_2| = a, \tag{2.28}$$

where $\mathbf{a}_{1,2}$ are the primitive lattice vectors. The shape of the lattice is also defined through the angle between the two primitive lattice vectors and is defined here as θ. For a hexagonal lattice, $\theta = 60°$ or $120°$. The real lattice for a hexagonal array is illustrated in Figure 2.5. Every point in the real lattice can be defined through a combination of the two lattice vectors

$$\mathbf{R} = n_1\mathbf{a}_1 + n_2\mathbf{a}_2, \tag{2.29}$$

where n_1 and $n_2 \in \mathbb{Z}$. For every real space lattice, there exists also a reciprocal lattice, that is, a Fourier transform of the real lattice. The reciprocal lattice, instead of representing the array in real space, represents the frequency space of the corresponding real lattice. The reciprocal lattice provides information regarding the diffraction properties of the real space lattice. Any point on the reciprocal lattice can be defined, similarly to the real lattice, through its primitive vectors

$$\mathbf{G} = m_1\mathbf{b}_1 + m_2\mathbf{b}_2, \tag{2.30}$$

where m_1 and $m_2 \in \mathbb{Z}$ and $\mathbf{b}_{1,2} = 2\pi/\mathbf{a}_{1,2}$.

An actual periodic array can be constructed by placing some arbitrary structure at each of the lattice points. Let us assign a wave vector to a light wave propagating towards the array as $\mathbf{k}_{\parallel,inc}$. When the incoming light interacts with the array, the light is diffracted at each lattice point and spherical waves are produced, the outgoing wave will have a different wave vector compared to incoming wave. This diffracted wave can be assigned a wave vector to be $\mathbf{k}_{\parallel,diff}$. This change in wave vector can be associated with the lattice vector of the reciprocal lattice and this

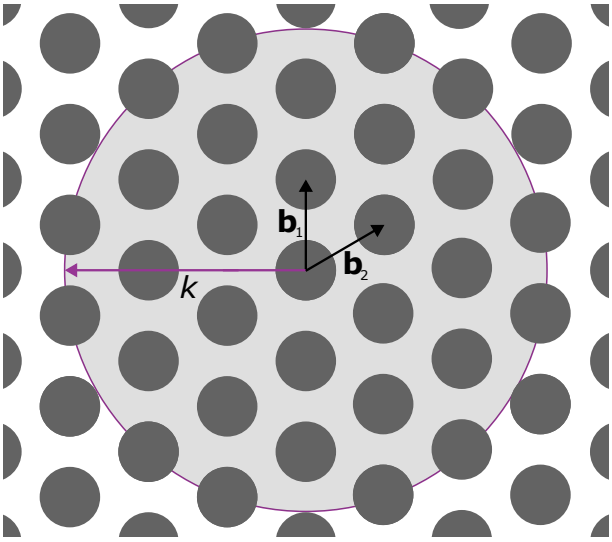

Figure 2.6: Reciprocal lattice of the periodic hexagonal array in Figure 2.5. The primitive vectors of the reciprocal lattice are given by $\mathbf{b}_1 = \mathbf{b}_2 = |\mathbf{b}|$. The reciprocal lattice is the visualisation of the Fourier transform of the real lattice. The propagating diffraction modes are given as all the points within the circle with a radius equal k.

condition tells us that constructive interference will occur, and hence a diffraction order when the difference between the incoming and diffracted wave vectors are equal to a vector of the reciprocal lattice, $\mathbf{G}$ [76]. The Laue equation can be written as

$$\mathbf{G} = \mathbf{k}_{\parallel,diff} - \mathbf{k}_{\parallel,inc} = \Delta\mathbf{k}, \tag{2.31}$$

and therefore the diffraction orders are defined through the integers $m_{1,2}$. Although not all of the diffraction orders will actually be propagating, some will be evanescent. To determine which orders will be propagating and which will be evanescent, we will need to look at the wave vector component of the incoming beam that is perpendicular to the surface of the array, which we can call $\mathbf{k}_\perp$. Due to conversation of the wave vector and the Laue condition, we can derive the component for the perpendicular component of the diffracted wave $k_{\perp,diff}$. The magnitude of the diffracted perpendicular wave vector is then defined as

$$k_{\perp,diff} = \sqrt{k^2 - \mathbf{k}^2_{\parallel,inc}}, \tag{2.32}$$

where k is the wavenumber in the medium. From this, we can deduce that when $\mathbf{k}^2_{\parallel,inc} \leq k^2$, $k_{\perp,diff}$ is real and is able to propagate. For the opposite case $\mathbf{k}^2_{\parallel,inc} > k^2$, $k_{\perp,diff}$ becomes imaginary and will decay in a exponential fashion. This can be visualised by drawing a circle of radius k around the origin point on the reciprocal lattice. The condition for diffraction to occur is defined as when the wavenumber of the wave is just large enough such that diffraction orders larger than the zeroth order, $(0,0)$ can propagate. As higher diffraction orders are allowed to propagate, they travel with non-zero wave vectors in the x and y directions. This is shown in figure 2.7, where the zeroth order propagates with the same direction as the

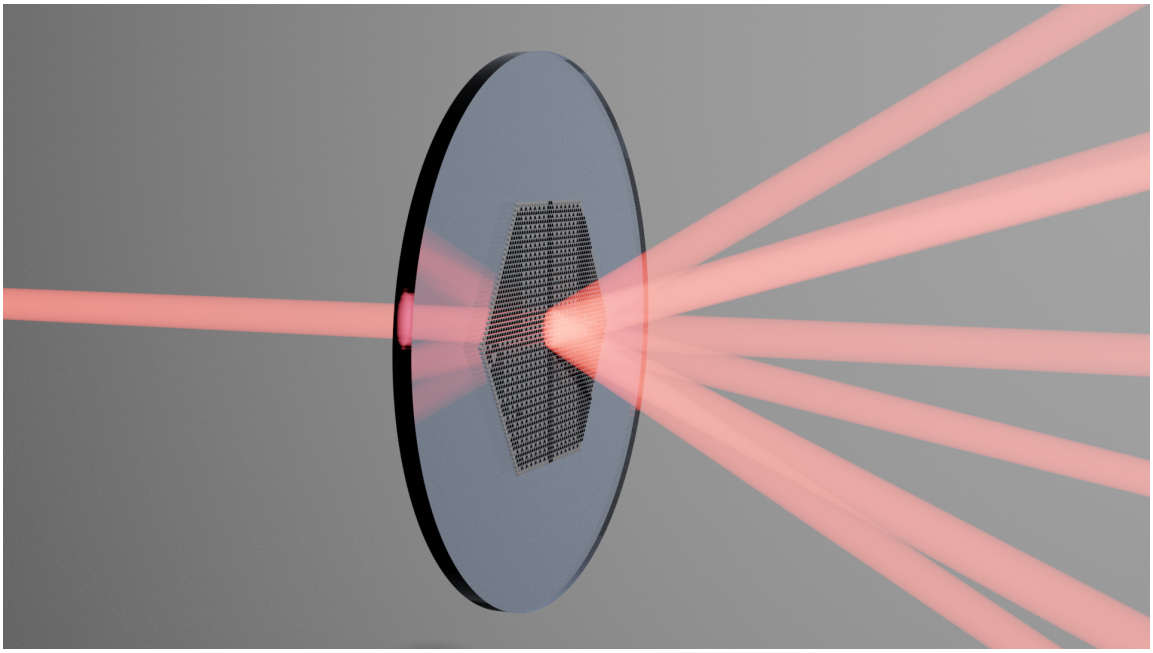

Figure 2.7: Render of monochromatic laser light impinging at normal incidence diffracted onto a hexagonal array of silicon disks, showing the far field diffraction pattern. The zeroth order and six first diffraction orders are shown. Depending on the wavelength of the incoming light and the spacing between the elements in the array, the angle of diffraction will vary.

incoming beam while the six first diffraction orders propagate with a different direction defined through the diffraction angle. The angle between the surface normal and the diffraction order is dependent on the diffraction order number and the angle will be larger for higher diffraction orders. From the reciprocal lattice description, the angles of propagation of the diffraction orders can be calculated by recalling Bragg's Law [77].

2.2.2 *Helicity Preservation Through Diffraction*

Now we have covered the diffraction of light from the 2-dimensional array, now we will look into how this can be applied in this work. For aiming to enhance the circular dichroism signal, some requirements need to be met. One such requirement is that the helicity of the light needs to be preserved throughout the light interactions with the matter in the system. This includes the diffracting array as well as the upon reflection of the light at an interface between two media. The need for helicity preservation on reflection will become clear in chapter 2.3.3 when the cavity designs are discussed. Now we will look at how the helicity of the light

is preserved upon scattering with the diffracting array.

The first possible solution for preserving helicity when light interacts with some matter would be duality [78, 79]. Duality, or dual symmetry, is when the magnetic and electric responses are the same, i.e., the permeability and permittivity of the media are equal. Duality symmetry is also governed by Noether's theorem that states that conserved quantities of a system or object are associated with some symmetry of the system, similarly to the momentum of the system, for example, which is conserved due to the spatial symmetries. Duality symmetry is not a spatial symmetry but rather a symmetry of Maxwell's equations. Helicity preservation can be depicted when some object is illuminated by a wave with a well defined right-handedness, when the object is perfectly dual, only waves that are right-handed will be scattered and this holds only for when $\epsilon = \mu$. when $\epsilon \neq \mu$, there will be components of the wave with left- and right-handedness scattered after interaction with the object. Although, helicity preservation through perfectly dual structures or media is only a concept in theoretical studies as matter does not typically have equal magnetic and electric responses apart from the very narrow spectral regions where they cross. Therefore, another method to achieve helicity preservation through the diffracting arrays must be used.

From the work of Fernandez-Corbaton, it can be shown that the scattering of light from an object that has at least a C_3 rotational symmetry will preserve the helicity on forward scattering, and flip the helicity on backward scattering [80]. This can be understood through calculating the scattering coefficients of the forward and backward directions of a plane wave. Let us first define a plane wave as $|\mathbf{p}\lambda\rangle$ where $\mathbf{p}$ is the momentum and λ is the helicity of the wave. We give the wave a well defined helicity of ± 1, where the wave is right-handed circularly polarised for $\lambda = -1$ and left-handed circularly polarised for $\lambda = +1$. Since only the forward and backward scattering directions are of interest, the plane wave can be defined as $|\pm p\hat{\mathbf{z}}\lambda\rangle$, where $p = |\mathbf{p}|$ and $\hat{\mathbf{z}}$ is the axis of which the light propagates.

To prove that a structure with a C_3 rotational symmetry preserves helicity on forward scattering, one must look at the forward and backward scattering coefficients, $\tau_f^{\lambda\bar{\lambda}}$ and $\tau_b^{\lambda\bar{\lambda}}$ respectively, which are defined through the scattering operator, S. Here, λ is the helicity of the incoming wave and $\bar{\lambda}$ is the helicity of the scattered wave. The forward and backward scattering coefficients are defined through:

$$\tau_f^{\lambda\bar{\lambda}} = \langle \bar{\lambda}\, p\hat{\mathbf{z}}|S|\, p\hat{\mathbf{z}}\, \lambda\rangle, \tag{2.33}$$

$$\tau_b^{\lambda\bar{\lambda}} = \langle \bar{\lambda}\, -p\hat{\mathbf{z}}|S|\, p\hat{\mathbf{z}}\, \lambda\rangle. \tag{2.34}$$

The complete derivation of the following expressions for calculating the forward and back scattering coefficients can be found in [80]. The forward scattering

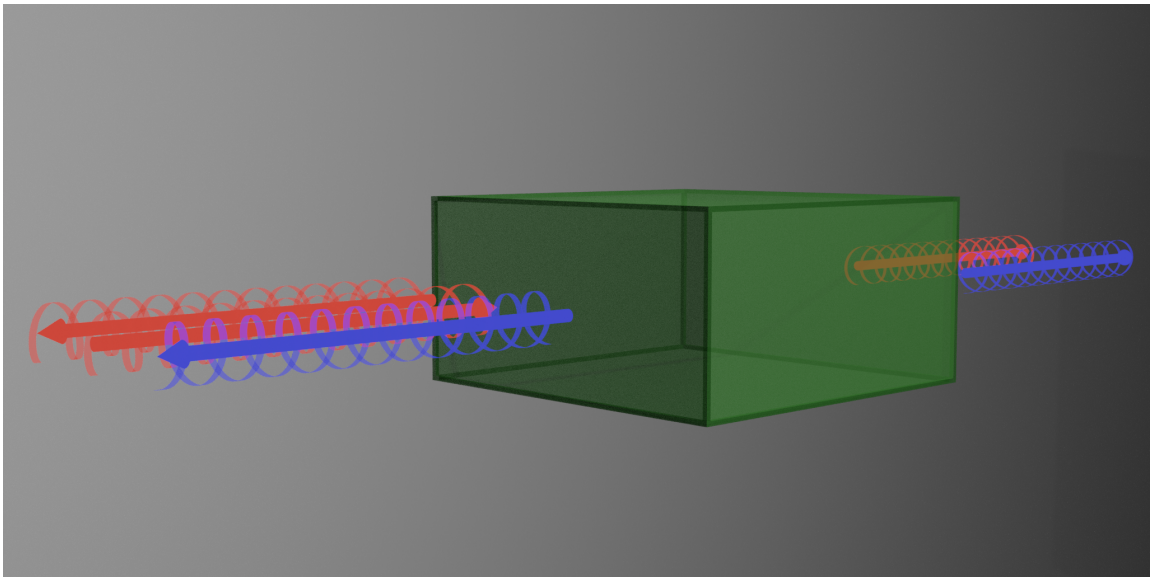

Figure 2.8: Render showing the forward and back scattered circularly polarised light from an object with a C_2 rotational symmetry. The blue light donates right-handed CPL and the red light donates left-handed CPL. As the rotational symmetry of the object is less than 3, both right- and left-handed CPL are produced on forward and backscattering. Adapted from [80] with permission.

becomes

$$\tau_f^{\lambda\bar{\lambda}} = \exp\left(-i(\lambda - \bar{\lambda})\frac{2\pi}{n}\right)\tau_f^{\lambda\bar{\lambda}}. \tag{2.35}$$

Here, n defines the number of discrete rotational symmetries of the system. Now for this relation, what needs to be proved is that there is only helicity preserving scattering and no component of forward scattering containing any helicity change. Helicity preserving is simple as $\lambda = \bar{\lambda}$, which results in $\tau_f^{\lambda\bar{\lambda}} = \tau_f^{\lambda\bar{\lambda}}$. For a component of helicity change, $\lambda = -\bar{\lambda}$, reducing equation 2.35 to

$$\tau_f^{\lambda\bar{\lambda}} = \exp\left(\pm i\frac{4\pi}{n}\right)\tau_f^{\lambda\bar{\lambda}}, \tag{2.36}$$

it is only possible to satisfy this equation in two possible ways. This first being that there is forward scattering, i.e. $\tau_f^{\lambda\bar{\lambda}} = 0$, or there is an integer that is equivalent to the fraction within the exponential, which will be defined as $2\pi k$. This is only satisfied when n is equal to either 1 or 2 and cannot happen for any value of $n \geq 3$, therefore meaning $\tau_f^{\lambda\bar{\lambda}} = 0$ when the system has a 3-fold or greater discrete rotational symmetry. This numerically shows that the forward scattering

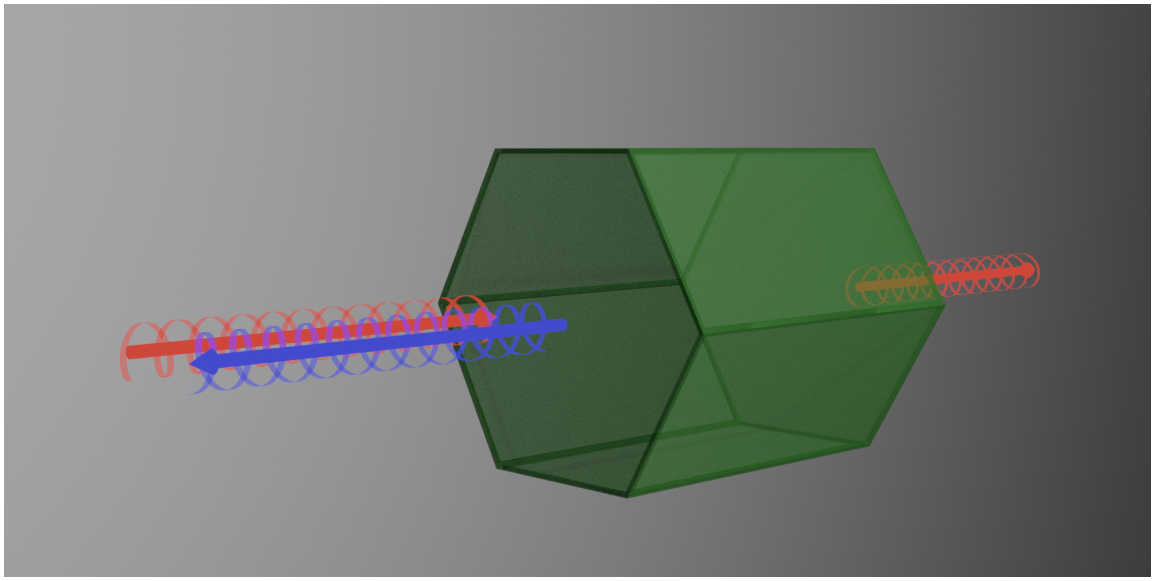

Figure 2.9: Render showing the forward and back scattered circularly polarised light from an object with a C_6 rotational symmetry. The blue light donates right-handed CPL and the red light donates left-handed CPL. As the rotational symmetry of the object is greater than 3, only Left-handed CPL is produced on back scattering and only right-handed CPL is produced on forward scattering. Adapted from [80] with permission.

of a system with a rotational symmetry of C_3 or higher can only contain the preserved helicity components of the incoming waves. The exact same derivations can be done for the back scattering coefficient of the system, showing that only the helicity changing component can be present in the back scattering for the same system. Following similar derivations for the forward scattering coefficient, the back scattering coefficient can be obtained as:

$$\tau_b^{\lambda\bar{\lambda}} = \exp\left(-i(\lambda+\bar{\lambda})\frac{2\pi}{n}\right)\tau_b^{\lambda\bar{\lambda}}. \tag{2.37}$$

It can then be shown using the same arguments as done for the forward scattering that for helicity preserving scattering $\lambda = \bar{\lambda}$ for back scattering when the system has a discrete rotational symmetry of $n \geq 3$. This effect has been shown experimentally in [81, 82]. In this work we apply the same methods to obtain helicity preservation on forward scattering. The designed diffracting array has an overall C_6 symmetry and therefore will preserve the helicity when the light is diffracted in the forward direction.

2.3 Chiroptical activity

We now direct the discussion towards Bi-anisotropic media and also chiroptical effects. The general case of a bi-isotropic medium is firstly discussed in terms of it's coupling constants, and the various different media that can be described whether these coupling constants are 0, real or imaginary. Thereafter, the two mechanisms of probing a chiral media are discussed, which are optical rotation and circular dichroism.

2.3.1 Bi-Isotropic Media

The following discussion is obtained from the works given in these references [83, 84]. A bi-isotropic medium can describe a chiral medium, which can rotate the plane of polarisation of linearly polarised light. A solution containing chiral molecules can be thought of as a bi-isotropic medium, which are defined through following constitutive relations:

$$\begin{aligned} \mathbf{D}(\mathbf{r},\omega) &= \epsilon\mathbf{E}(\mathbf{r},\omega) + \xi\mathbf{H}(\mathbf{r},\omega), \\ \mathbf{E}(\mathbf{r},\omega) &= \mu\mathbf{H}(\mathbf{r},\omega) + \zeta\mathbf{E}(\mathbf{r},\omega), \end{aligned} \tag{2.38}$$

where ζ and ξ are the coupling constants for the electric and magnetic fields. These coupling constants are defined through the reciprocity (Tellegen) parameter, χ and the chirality (Pasteur) parameter κ through

$$\begin{aligned} \xi &= \sqrt{\epsilon\mu}(\chi - i\kappa), \\ \zeta &= \sqrt{\epsilon\mu}(\chi + i\kappa). \end{aligned} \tag{2.39}$$

Additionally, if $\chi = \kappa = 0$, the resulting medium is an isotropic medium as was discussed previously, in section 2.1.

If $\chi = 0$ and $\kappa \neq 0$, the coupling parameters become real values, and the resulting medium is classed as a non-reciprocal medium. An example of a non-reciprocal medium is one that exhibits the Faraday effect, where the polarisation of the light can be rotated when the medium it travels through is subject to an external magnetic field. However, this work will not dive any further into non-reciprocal media.

In the other case, when $\chi \neq 0$ and $\kappa = 0$, the coupling parameters are imaginary. The non-vanishing κ parameter defines the medium to be a chiral medium, also coined as a Pasteur medium. A chiral medium can be thought of as a material that interacts differently to right- or left-handed circularly polarised light, due to the medium having a broken spatial symmetry, which is due to the molecular structure of the bulk medium.

To understand how light travels within chiral media and therefore how certain mechanism can be exploited for sensing applications, we look at the wave numbers for the right- $(+)$ and left-handed $(-)$ polarisation states, travelling through the medium

$$k_{\pm} = (\sqrt{\epsilon\mu} \pm \kappa)\frac{\omega}{c}, \tag{2.40}$$

The refractive index for these two polarisation states are different and can be determined to be

$$n_{\pm} = \sqrt{\epsilon\mu} \pm \kappa = n \pm \kappa. \tag{2.41}$$

This difference in the refractive index for the two polarisation states are the reasoning behind the chiroptical effects. The complex reactive index can be denoted as

$$n_{\pm} = n_{\pm} + ik_{\pm}. \tag{2.42}$$

The difference between the two effects is whether the real, or imaginary part of the refractive index is the dominant factor. Optical rotation is determined by a differing real part of the refractive index between the two polarisation states, while circular dichroism is determined by a differing imaginary part of the refractive index.

2.3.2 *Optical Rotation*

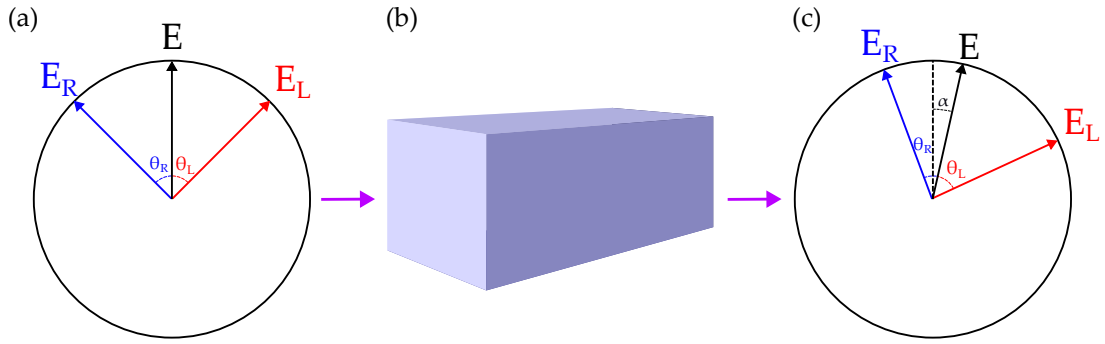

Figure 2.10: Description of optical rotation through the superposition of right- and left-handed CPL. (a) Before travelling through an optically active medium, the electric field components of the right- and left-handed CPL at a given point in space with equal phases are superimposed to create linearly polarised light. The angle between the two electric field vectors are given by θ_R and θ_L. (b) The blue cube represents an optically active medium that the light travels through. (c) The optically active medium induces a differing phase change in the right- and left-handed CPL, resulting in the superimposed linearly polarised light being rotated by an angle α.

Optical rotation (OR), or circular birefringence, is one method to probe into determining the handedness of a solution of chiral molecules. This is because when linearly polarised light is projected through a chiral medium, such as sucrose dissolved in water. The light exiting the solution is still linearly polarised, but the orientation of this polarisation has been rotated. The magnitude and direction of this rotation depends of several factors such as the distance it travels through the solution, the concentration of the molecules in the solution and the handedness of the molecules in the solution.

The difference in the real part of the refractive index between the two polarisation states is what induces the rotation of the linear polarisation. Linearly polarised light can be described as a superposition of both left-handed and right-handed CPL. At a given point in space, the electric field vectors for the right- and left-handed CPL can are set at angles θ_R and θ_L from the y-axis respectively as shown in panel (a) of Figure 2.10. If there is an initial deviation of the linear polarisation from the y-axis, θ_0, is can be defined through θ_R and θ_L as

$$\theta_0 = \frac{1}{2}(\theta_L + \theta_R). \tag{2.43}$$

The difference in the real part of the refractive index is given by $\Delta n = n_+ - n_-$. This difference induces a phase shift between the two polarisation states due to the difference in velocities of the right- and left-handed CPL waves in the medium, which in turn results in a rotation of the linearly polarised light of

$$\alpha = \frac{\omega L}{2c}\Delta n, \tag{2.44}$$

where L is the path length through the solution, c is the speed of light in the medium, and ω is the frequency of the light. The resulting rotated linearly polarised light is illustrated in panel (c) of Figure 2.10.

Optical rotation is now a commonly used method for probing the handedness of chiral molecules. Depending on the direction that an enantiomer of a molecule will rotate the plane polarised wave, the enantiomer can be said to be either dextrorotatory or laevorotatory. When looking at the light source, if the enantiomer rotates the polarisation plane of light clockwise, it is dextrorotatory, and if the rotation is in the opposite direction, anti-clockwise, it is laevorotatory. For a certain molecule, the two enantiomers have opposite absolute configurations, given a constant optical path length through the solution, a rotation of linearly polarised light will have equal magnitude but the direction of rotation will be opposite [85]. Most optical rotation measurements are carried out at the same wavelength, which has been chosen to be at 589 nm, corresponding to the sodium D-line. Given a constant wavelength, a chiral compound has defined specific

rotation associated with them. This specific rotation is how much the compound rotates plane polarised light per unit distance as well as which direction the light is rotated. It is also dependent on the concentration of the compound. For example, D-sucrose has a specific rotation of $+66.37\,\mathrm{deg\,dm^{-1}cm^3g^{-1}}$ [86, 87]. Another form of optical rotation is optical rotary dispersion (ORD), where rather than a singular wavelength, white light is used.

2.3.3 *Circular Dichroism*

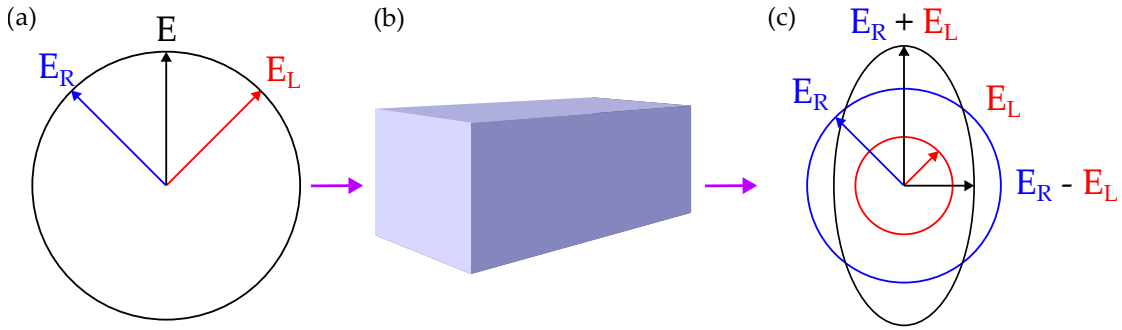

Figure 2.11: Description of circular dichroism depicted through superposition of right- and left-handed CPL. (a) Before travelling through an optically active medium, the right- and left-handed CPL are in phase and have equal amplitudes. The sum of the amplitudes is E. (b) The blue cube represents an optically active medium that the light travels through. (c) The optically active medium induces a differential absorption between right- and left-handed CPL amplitudes, the resulting summation of the amplitudes creates an elliptical polarisation.

Contrary to optical rotation stemming from the difference in the real part of the refractive index, circular dichroism (CD) is due to the difference in the imaginary part of the refractive index. This is also a difference in the absorption of left-handed CPL to right-handed CPL by the medium that they propagate through. CD can also be visualised again by taking the superposition of right- and left-handed CPL. Before travelling through any chiral medium, the two polarisations can be superimposed to create linearly polarised light, as showing in panel (a) of Figure 2.11. When travelling through a medium, they experience different amounts of absorption, resulting in two differing amplitudes for the right- and left-handed CPL. The resulting superposition of the two polarisations forms an ellipse. It's worth noting, that the CD spectrum is sometimes measured in the degree of ellipticity of the resulting polarisation, however, this work will denote the CD in terms of the differential absorption or the differential transmission. The

differential absorption can be simply written as

$$\Delta A = A_L - A_R, \tag{2.45}$$

where ΔA is the difference in absorption and A_L and A_R are the absorption of the left- and right-handed CPL, respectively. This is also known as the absorbance circular dichroism (ACD). In typical measurements, the ACD is defined through the outgoing powers of the left- and right-handed CPL, P_L and P_R, and the total input power, P_0.

$$ACD = \frac{P_L - P_R}{2P_0}. \tag{2.46}$$

Although in theory, absorbance CD is the most commonly seen form of CD, it is not so simple when it comes to actual experiment. This is due to needing to measure the total input power of the light as well as both the reflected and transmitted power from the sample. An easier form of CD to measure experimentally is the transmission CD (TCD), which does not require the reflected power to be measured and only the input power and the transmitted power of the light. The TCD can be defined through

$$TCD = \frac{P_L^{fwd} - P_R^{fwd}}{P_L^{fwd} + P_R^{fwd}}, \tag{2.47}$$

where P_L^{fwd} and P_R^{fwd} are the forward directing transmitted powers from the chiral medium of the left- and right-handed CPL, respectively. The denominator in the fraction is a normalising term which is used to remove signals that arise from the light source or optics in the measurement system, similar to the P_0 term for the ACD.

It is worth noting, that in real life, optical activity and circular dichroism are not completely independent, but a chiral medium will actually show the effects of both. The two are related through the Kramers-Kronig relations [72, 88].

Chapter 3

3 Theory of a Metasurface Cavity for Chiral Sensing

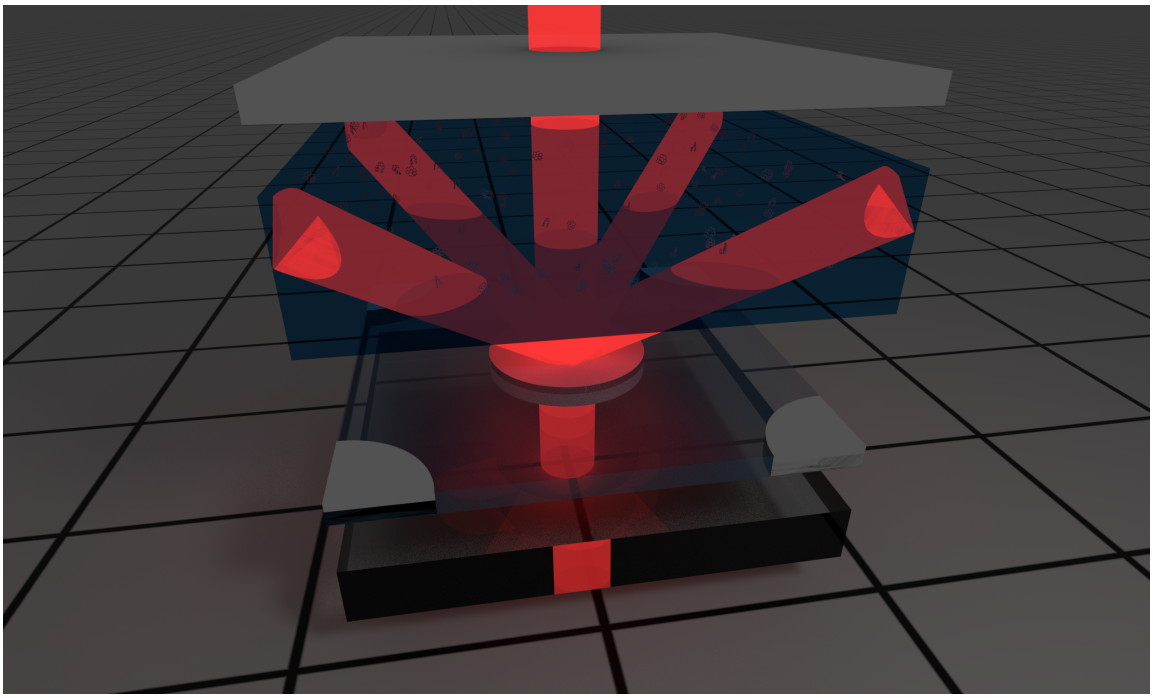

Illustration of the building blocks of the transfer matrix formalism

This chapter details the operating principles behind the cavity design proposed in this work. I will introduce the two cavity designs and discuss the considerations behind the systems and then detail the differences in performance between the two designs. Within, there will be a brief description of how these numerical calculations are performed.

I conclude with the steps taken to bring the numerical calculations into line with the experimentation circumstances, and how the concentration of the molecules in the solvent effects the CD enhancing capabilities of the cavity.

3.1 Structures for Enhancing Chiral Signals

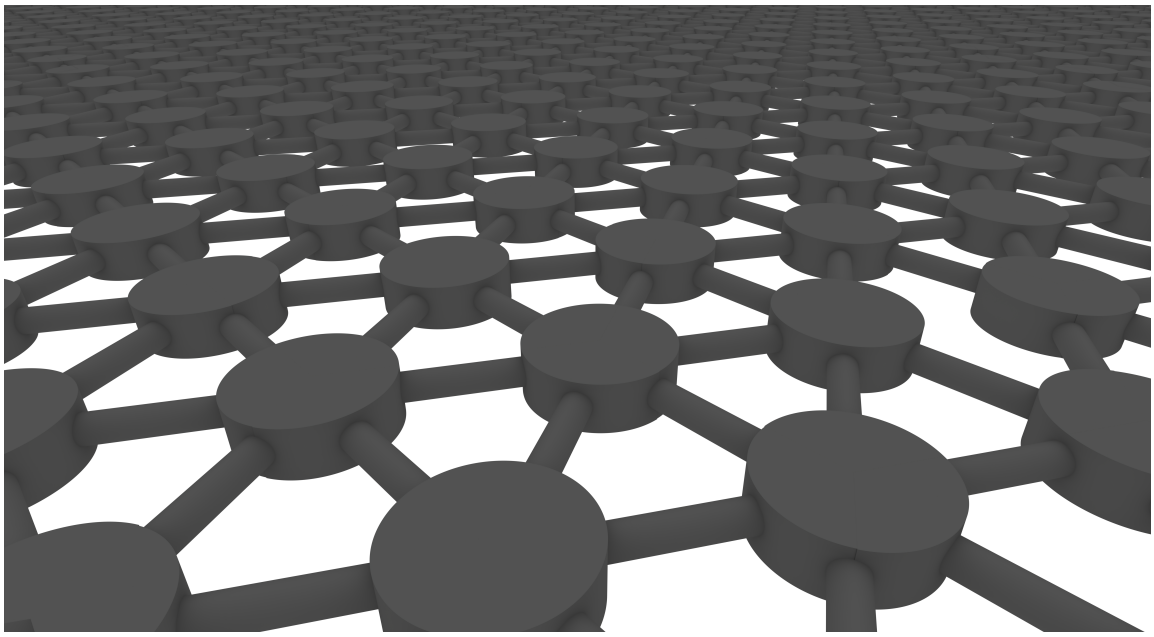

Figure 3.1: Illustration of a 2D periodic silicon cylinder array for chiral sensing. No substrate is used and the cylinders are conjoined by rods to be a stable structure. Adapted from [64] with permission.

A multitude of both theoretical and experimental studies have been reported on the task of enhancing the circular dichroism signal of molecules in the gas, liquid and solid states [25–61].

Let us firstly consider the work published by Graf, *et al.* [64]. Here, an array of silicon cylinders in a square array formation for the enhancement of circular dichroism is reported, although 3.1 shows the structures in a hexagonal array. The principle of operation is tailoring the height and radius of the silicon cylinders such that the near-field magnetic and electric responses become degenerate, meaning that the electric and magnetic responses are the same. The already resonant nature of the cylinders provides the necessary field enhancement and the degeneracy of the magnetic and electric responses provide the preservation of the polarisation of the light. The combination of the intense near fields and the preservation of the polarisation of the light provides the perfect recipe for chiral enhancement. To maximise the accessibility of regions of high field enhancement, the use of a substrate was eliminated and the cylinders were conjoined with bars between the nearest neighbours in the array. An adaption of their design, but in a hexagonal array formation is depicted in Figure 3.1. While the design choice to not use a

substrate has positive implications for the performance, as the volume of chiral analyte that will experience the resonant effects will be greater, a realisation of such a structure would be difficult. The areas of large enhancement only expand some hundreds of nanometres from the structure itself, leading to a small volume of analyte that would feel the enhancing effects.

Numerous plasmonic nano- and microstructures, in both 2D and 3D have been reported for enhanced CD sensing, many of which are chiral [27, 30, 31, 38]. Schäferling et al. reports a review study on various designs of plasmonic structures and discusses their respective CD enhancing properties [28]. Plasmonic structures show strong near-field resonances which produce strong chiral fields that can be therefore used to enhance the CD response of molecules placed within these fields. In general, plasmonic structures report 1-2 orders of magnitude enhancement. However, while previously chiral structures were beneficial for the enhanced detection of chiral molecules [31, 89], it was discovered that the contrary is the case as the chiral nano and microstructures themselves will produce unwanted artificial signals that will drown out the response of the molecules under investigation [34, 45].

Another approach that has been reported for enhanced chiral sensing is through whispering gallery mode (WGM) microcavities [62]. The study here reports enhancement factors of over two orders of magnitude through high Q-factors within the WGM microcavities and show the relation between the thickness of the chiral analyte as well as the gap for the microcavity. While giving promising results, a fundamental issue arises again when the volume of analyte experiencing an enhancing effect is very small.

Therefore, we want to find a system that can provide a large field enhancement over a large volume and preserve the helicity of the light. The paradigmatic system for enhancing light-matter interactions and also providing these resonances over a large volume is an optical cavity.

3.2 Optical Cavities for Circular Dichroism Enhancement

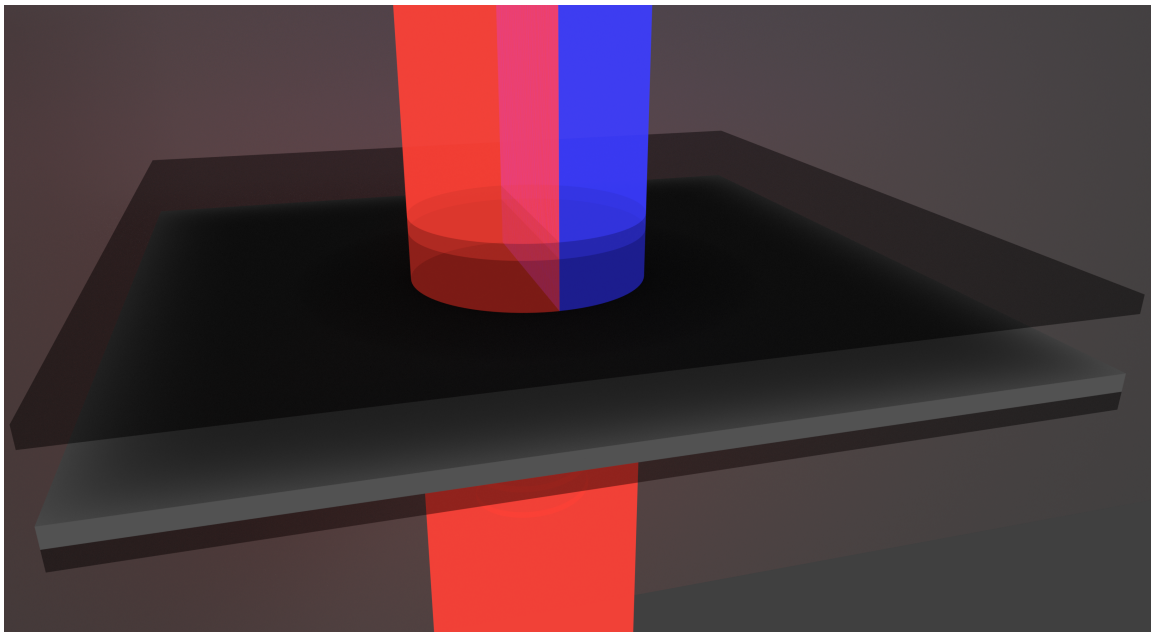

Figure 3.2: Render of a Fabry-Pérot cavity that is illuminated with left-handed CPL (red). A Fabry-Pérot cavity is the paradigmatic system that one would opt for when aiming for strong light-matter interactions. Although not suitable for chiral studies because on normal incidence reflection, the handedness of the light is completely flipped. Left-handed CPL is converted to right-handed CPL (blue) on reflection. Multiple reflections within the cavity result in a perfect mix of left- and right-handed light.

Let us first consider a simple Fabry-Pérot cavity. The Fabry-Pérot cavity is constructed from two plane parallel mirrors separated by a set distance, as depicted in Figure 3.2. Although, with such a cavity, there will be indeed enhanced light-matter interaction due to the strong resonances of the electro-magnetic field within the cavity, if we recall the Fresnel reflection coefficients (equations 2.16), we see that on normal incidence reflections, the helicity of the light will be completely flipped. Within a Fabry-Pérot cavity, there are many reflections and this would lead to an almost perfect mix of helicities within the cavity, resulting in the circular dichroism signal becoming zero [90]. Therefore, we must think of a solution to this issue to avert the helicity flipping on reflection.

To circumvent this issue of helicity mixing through the reflections, we need to think of a different type of optical cavity to achieve enhanced chiral sensing.

3.2.1 *Double-Array Cavity Design*

As stated in section 2.1, the Fresnel refection coefficients show that for near grazing angles of incidence, $\theta \to 90°$, the helicity of light is preserved on reflection. A system that supports resonant modes, with near-grazing angles of incidence would be a plane-parallel waveguide. The only part that is missing for an optical cavity that would be suitable for the type of resonant modes we are interested in, is how the light is coupled in and out of these modes. We need a solution to couple the light into the cavity, such that it matches the angle needed to support these modes. We cannot have the light coming in perpendicular to the mirrors and also cannot simply have the light coming in from the side as there will be implications with the design of the cavity as the ends of the waveguide will be sealed and not allow for light propagation. It is possible to excite these modes by replacing one or both of the cavity mirrors with diffracting arrays. A diffracting array provides the means to couple light that is incoming perpendicular to the cavity mirrors into these planar cavity modes that preserve helicity as well as also functioning to couple the light out of the cavity for detection. This principle of using a diffracting array to couple light in and out of a plane-parallel waveguide is called guided-mode resonance (GMR) and this operation principle is depicted in Figure 3.3. GMRs have been utilised in applications such as wavelength filters, mirrors and as sensors [91–93].

To understand the principle of operation of GMRs, let us first look at the modal condition of a plane-parallel slab waveguide. Let us take two dielectric mirrors with refractive index, n_2, separated by a thickness, d. These two mirrors encase another material with refractive index, n_1. Let us consider a plane wave propagating along the x-axis in the waveguide, with the angle of incidence onto the half-space material, acting as the cavity mirrors being θ. When we consider the modal condition for a propagating mode in this type of waveguide, a stable mode will only propagate when the round trip phase is equal to an integer of 2π. The modal condition for the TE and TM modes are defined as [72]

$$4dk\sin(\theta) + 2\Phi_{TE/TM} = 2\pi l_{TE/TM}, \tag{3.1}$$

where $\Phi_{TE/TM}$ is the phase of the TE and TM polarisation respectively, $l_{TE/TM}$ is an integer mode number and k is the wavenumber in the medium n_1. The phases are defined as

$$\Phi_{TE} = -2\arctan\sqrt{\frac{2\Sigma}{\sin^2(\theta)} - 1}, \tag{3.2}$$

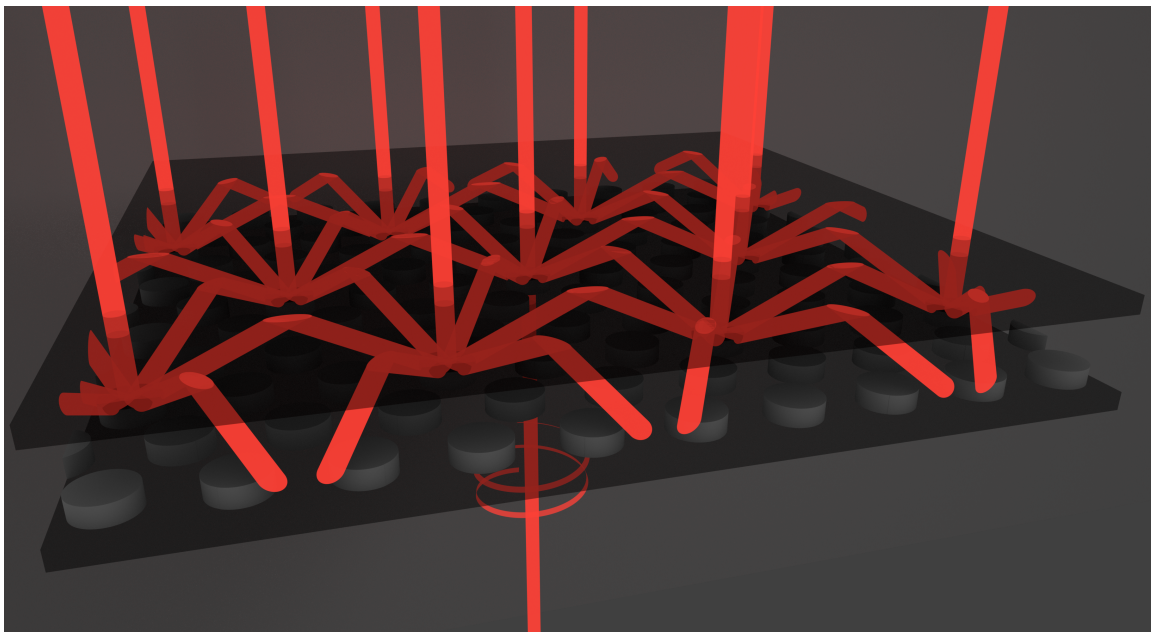

Figure 3.3: Render of a metasurface cavity with one mirror constructed with a hexagonal array of silicon cylinders and the other mirror a conventional mirror. Left handed circularly polarised light propagates toward the cavity at normal incidence from below. On interaction with the diffracting array, the first diffraction orders couple into the waveguide modes. Through another interaction with the diffracting array, they are coupled out of the cavity.

for the TE mode and

$$\Phi_{TM} = -2\arctan\left(\frac{1}{1-2\Sigma}\sqrt{\frac{2\Sigma}{\sin^2(\theta)}-1}\right), \tag{3.3}$$

for the TM mode, where $\Sigma = (n_1^2 - n_2^2)/2n_1^2$ [65, 72]. Recalling back to the condition that we require for the helicity preservation on near-grazing reflections. When $\theta \to \pi/2$, $\Phi_{TE/TM} \to \pi$ and the TE and TM modes become degenerate and therefore preserving helicity on reflection.

Now let us replace the mirrors in the waveguide with two diffracting arrays. The diffracting arrays function as explained in section 2.2. If we recall equation 2.32, we are able to calculate the transverse momentum of the light after interacting with the diffraction grating. Then substituting this into equation 3.1, we can determine the angle of propagation for the diffraction orders as

$$\theta = \cos^{-1}(\frac{k_{\perp,diff}}{k}), \tag{3.4}$$

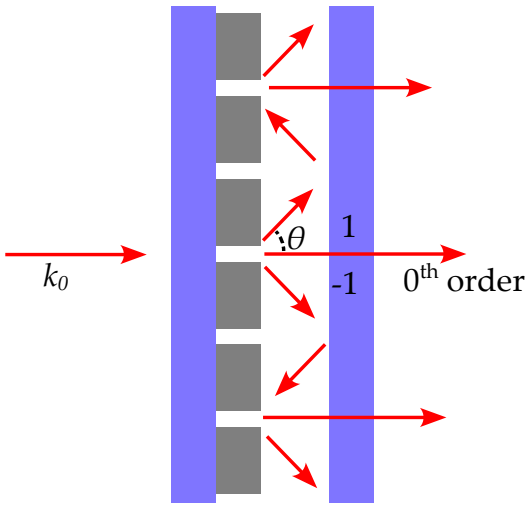

Figure 3.4: Principle of operation for guided mode resonances. A plane wave travels toward the cavity and is diffracted by the diffracted array. When the angle of the diffraction order and the modal condition of the waveguide match, the light propagates within the cavity. k_0 is the wavenumber of the incident light in vacuum and θ is the angle between the normal and the propagation direction of the first diffraction order.

with $k_{\perp,diff}$ as the magnitude wave vector of the diffracted order perpendicular to the array and k is the wavenumber of the light in the medium. Diffraction orders that are higher than the zeroth order have wave vector components that are non-zero in the lateral directions and these are the diffraction orders that we can utilise to couple the light into the waveguide. We excite these modes by matching the diffraction angle of the mode to the angle of which the mode can propagate within the waveguide. An illustration of the principle of operation of guided mode resonances is shown in Figure 3.4.

Now we have the basic principle of operation of this cavity design at hand, we can look to see how this can be tailored for the enhancement of circular dichroism. Let us look at the cavity configuration depicted in Figure 3.5. The two mirrors of the waveguide are replaced by hexagonal arrays of silicon cylinders. We showed in section 2.2 that the scattering off of a system with a rotational symmetry of at least C_3 will be helicity preserving [94], although only in the forward direction. For helicity preservation into the first diffraction order, this cannot be achieved through the symmetry of the system, but tuning the parameters of the diffracting array elements can achieve an equal response of the electric and magnetic responses leading to high helicity preservation into the first diffraction orders. So if we can tailor the parameters of the diffracting arrays such that the diffraction angle of the first order is near grazing and matches the modal angle, and are highly helicity preserving, we can construct an optical cavity that will be helicity preserving and thus an ideal system for enhancing circular dichroism.

The following discussion is based on the findings by Feis et al. [51, 65]. The parameters chosen for the double-array cavity are as follows. The silicon cylinders

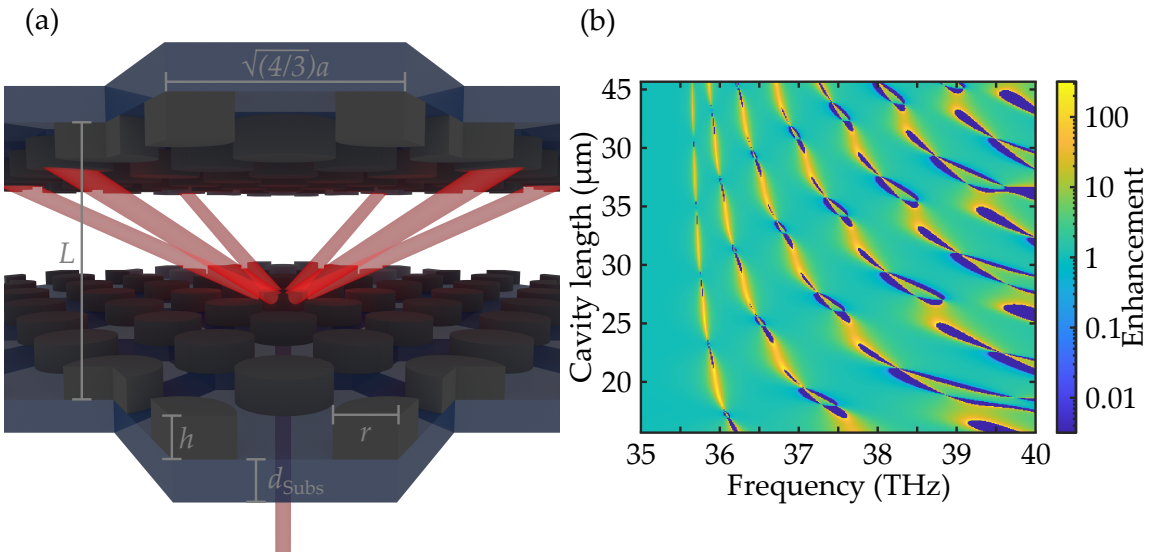

Figure 3.5: (a) Computational render of the double-array cavity configuration depicting two silicon cylinder arrays where $r = 1.92\,\mu m$, $h = 1.32\,\mu m$, and $a = 5.76\,\mu m$ on top of calcium fluoride substrates where $d_{subs} = 2\,\mu m$. L depicts the cavity length. Circularly polarised plane waves enter the cavity from below under normal incidence and diffracts into the six first diffraction orders. The light will reflect off of both the top and bottom mirrors until it again interacts with the diffracting array to couple out of the cavity for detection (only the six diffraction orders without subsequent reflections is shown here). (b) The computed TCD enhancement of the double-array cavity as a function of the cavity length L and the frequency f. There exists negative enhancement values in the blue regions. Adapted from [51, 65] with permission.

to construct the arrays had a height $h = 1320\,nm$, a radius $r = 1920\,nm$, and a pitch $a = 5760\,nm$ and were assigned a permittivity of $\epsilon_{Si} = 11.9$. The diffracting arrays were placed upon a substrate with a thickness $d_{Subs} = 2\,\mu m$ and a permittivity $\epsilon_{Subs} = 2.14$. The cavity is then filled with a chiral medium based on the constitutive relations for a chiral media (equations 2.38) with the following parameters $\epsilon_m = 2.14 + i10^{-4}$, and $\mu_m = 1 + i10^{-4}$, and $\kappa_m = i10^{-4}$. Here, the permeability of all other materials is set to 1.

At this point, it would be useful to explain how these numerical calculations are performed. For the simulations, I would like to thank and give credit to everyone who worked on the simulation aspect of this work in the group of Prof. Dr Carsten Rockstuhl, the individuals that worked on the calculations are Dr. Ivan Fernandez-Corbaton, Dr. Markus Nyman, Dr. Benedikt Zerulla, Dr. Dominik Beutel and Dr. Xavier Garcia-Santiago. The CD enhancement properties of the cavity configurations are calculated using an in house developed script for solving the interaction of the electromagnetic waves in a multilayer optical system

[64, 95], which is the collaborative work with the group of Prof. Dr. Carsten Rockstuhl. The script uses the transfer matrix (T matrix) method that solves the interaction between plane electromagnetic waves and an optical system through the determination of the reflection and transmission of said plane waves by the system [96]. The entire response of the optical system to the plane waves is able to be computed through a single matrix operation. The final piece for the entire optical system is the response of the scatterers. This is solved through the use of a finite element method (FEM) solver JCMSuite [97], provided by JCMWave which uses the multipolar decomposition of the magnetic and electric fields to compute the scattered fields [98]. The interaction of the light and the diffracting array can also be described by a transfer matrix.

Now we will discuss how this cavity design performs for enhancing the circular dichroism signal. But first to note, that these values represent a very idealised version of the optical cavity and are used as the starting point on the investigation into the circular dichroism enhancing cavities. Figure 3.5 shows the transmission CD (TCD) enhancement for this cavity configuration for a broad range of input frequencies f and varying the cavity length L. We see the expected mode lines for a slab waveguide [72] and regions of enhancement. The enhancement in this plot is defined as the ratio of the TCD signal of this chiral medium within the cavity with the array structures and the same chiral medium without. The resonant modes in the enhancement plot shows and alternating fashion of high positive enhancement values and negative enhancement values. This can be explained due to the coupling between the zeroth and first diffraction orders. Although slightly difficult to see in this plot, the best enhancement values lie within the lowest resonant mode, and this is because, with increasing frequency for a fixed set of array parameters, the diffraction angle will increase, leading to more helicity conversion on reflection as the angle of reflection will move away from grazing incidence, which is required for helicity preservation on reflection. This will cause the helicity purity within the cavity to also worsen leading to a lower CD signal. Therefore, we will only concentrate on the lowest resonance mode from now on.

The realisation of this cavity type to the experiment has some difficulties that need to be discussed. First and foremost, a substrate for fabricating the diffracting arrays on cannot be as thin as 2 µm as there are none commercially available for purchase and it will be too fragile for experiments. Another experimental difficultly that we need to consider, is the alignment aspect of the two diffracting arrays. The results of the misalignment between the two cylinder arrays are shown in the supplementary information of [65]. The artificial signals produced by the misalignment of the reach values of up to ± 0.02 for angular misalignments of 7.5°, 15°, 22.5° and lateral misalignments between the two arrays on the scale of a few hundred nanometres. To quantify the effect of the misalignment between the two diffracting arrays, one of them is rotated and offset relative to the other and the

resulting CD signal is recorded. We see that even for very small displacements, the artificial signal can be several orders of magnitude larger than expected signals from chiral molecules. Typical CD signals are in the range of $10^{-4} - 10^{-5}$, so the artificial signals produced from the misalignment is predicted to be at least two orders of magnitude larger that the signals expected from the molecules. A real system that can prevent misalignments between the two diffracting arrays, which is not including parallel misalignments, will be incredibly difficult to realise in experiment. A revised system needs to be constructed to ease the fabrication process in order to realise an optical cavity like this for the enhancement of CD signals. In the next section, we discuss an optical cavity that completely removes this alignment requirement, although not considering the parallel alignment need, and again numerical simulations are performed to quantify it's enhancing capabilities.

3.2.2 *Single-Array Cavity Design*

A plane parallel optical cavity consisting of two diffracting arrays that are in place of the mirrors has already been discussed regarding it's performance on the enhancement of chiral signals. While this cavity configuration reports impressive enhancement values, the artificial signals from the misalignments would completely dominate over the signal from any chiral molecule within the chamber. Therefore, a system to eliminate the sources of these artificial signals is required. This is accomplished through a slight revision and simplification of this double-array cavity.

The solution here is to replace one of the diffracting arrays in the cavity with a silicon thin film as depicted in Figure 3.5 [51]. This completely removes this critical alignment between the two diffracting arrays, and the cavity will remain an achiral structure. The working principle being the cavity remains the same, but the performance on the CD enhancement changes due to this alteration of one of the mirrors. We keep the parameters of the diffracting array the same as for the double-array cavity configuration, and assign a thickness of 1 µm to the silicon thin film.

Now let us look into the differences in performance that occur with this change to one of the mirrors. Due to the implementation of the silicon thin film as a mirror, there now becomes two reflections off of the this mirror. One from the silicon-solvent interface and one from the silicon-substrate interface. The reflection from the silicon-solvent interface is still at near-grazing reflection angles and remains highly helicity preserving but now due to the refractive index difference at the silicon-solvent interface, a percentage of the light is coupled into the silicon thin film. For a angle of incidence on the silicon-solvent interface that is near-grazing,

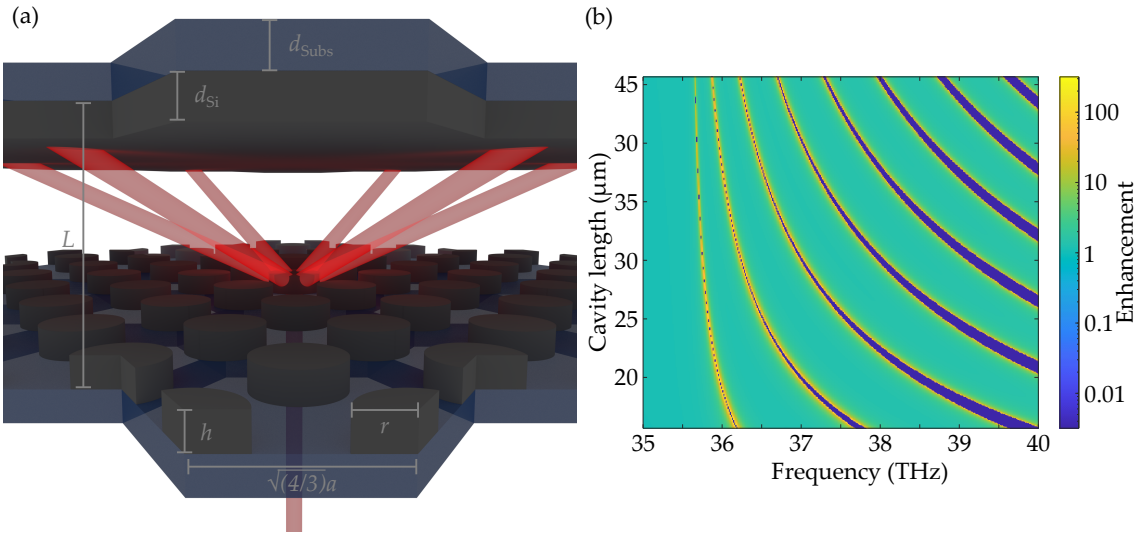

Figure 3.6: (a) Computational render of the single-array cavity configuration depicting two silicon cylinder arrays where $r = 1.92\,\mu m$, $h = 1.32\,\mu m$, and $a = 5.76\,\mu m$ on top of calcium fluoride substrates where $d_{subs} = 2\,\mu m$. The upper silicon cylinder array is replaced by a thin silicon film with a thickness $d_{Si} = 1\,\mu m$. L depicts the cavity length. Circularly polarised plane waves enter the cavity from below under normal incidence and diffracts into the six first diffraction orders. The light will reflect off of both the top and bottom mirrors until it again interacts with the diffracting array to couple out of the cavity for detection (only the six diffraction orders without subsequent reflections is shown here). (b) The computed TCD enhancement of the double-array cavity as a function of the cavity length L and the frequency f. There exists negative enhancement values in the blue regions. Adapted from [51, 65] with permission.

the refracted beam within the silicon thin film would tend towards an angle of 25°. Referring back to the reflection coefficients for the TE and TM modes in equation 2.16, we see that for such an angle there will be splitting of the polarisations and therefore a degradation of the helicity preservation on this reflection. This is visible in the TCD enhancement plot in panel (b) of 3.6. At frequencies near the condition for diffraction, when the wavelength of the light is just larger than the diffracting element, this splitting is not so large and the TE and TM polarisation are still approximately degenerate, but further away from this limit where the diffraction angles are far away from near grazing, this splitting becomes very apparent and regions of low and even negative enhancements appear due to the splitting of these modes [51].

Let us now discuss the differences in the enhancement capabilities between the two cavity configurations. Firstly, let us look at the differences in the mode lines in panel (b) of Figures 3.5 and 3.6. An obvious difference is observed: in the double-

array cavity, the enhancement value oscillates between positive and negative along the mode lines, whereas the single-array cavity shows no such trend. This oscillating trend can be explained through the crossing and anticrossings of the zeroth and first diffraction orders [99]. These occur when the round-trip phase of a mode within such a waveguide is an integer of 2π. Whether the coupling between the modes is an anticrossing or a crossing depends on the relative difference in phase at the point when the modes cross. If the difference in phase is an even integer of 2π, i.e. $2l\pi$ where l is a integer, there is an anticrossing because the two modes have the same parity and therefore experience strong coupling between the modes, leading to these large positive enhancing resonances as the helicity preservation of the mode is kept in tact here. In contrast, if the difference in phase is an odd integer i.e. $(2l+1)\pi$, then there is a crossing. At this crossing, the two modes are out of phase and have opposite parity, leading to weak coupling and a breakdown of the helicity preservation of the mode. This results in these low and negative enhancement regions seen. This coupling of the modes is in fact not seen in the single-array cavity configuration due the removal of one of the diffracting arrays and therefore leads to a breaking of the parity symmetry.

Now that the visual differences in these mode lines are understood, we can compare the differences in enhancement capabilities between the two cavity configurations. It would make sense to make a comparison at the exact same input frequency f and cavity length L, but due to the alteration of one of the mirrors between the two cavities, the position of the modes slightly changes. therefore, to compare the enhancement capabilities between the two cavity configurations, we can compare the maximum enhancement that is calculated. For the double-array cavity, the maximum enhancement of 318 is found at a cavity length of 18.8 µm and a frequency of 36.0 THz, which is the lowest (leftmost) mode in panel (b) of Figure 3.5. The maximum enhancement for the single-array cavity is 197 and is found at a cavity length of 15.7 µm and a frequency of 36.2 THz. Again, this enhancement is within the lowest mode of the single-array cavity as seen in panel (b) of Figure 3.6. It is clear that for this simplification to the cavity design that provides an ease in the fabrication, there is a rather significant detrimental effect to its enhancement capabilities. Despite this decrease to the enhancement factor, the advantage to the fabrication of the single-array cavity outweighs this for the first step in the experimental realisation of such optical cavities.

3.3 Implementation of Realistic Material Parameters

Now that the two cavity configurations have been introduced and their suitability for CD enhancement has been discussed, we now look to how we can bring these numerical calculations in line with the experiment. Up to this point, all of the material parameters in the calculations have been non-frequency dependent values and all absorptions have been neglected.

This section aims to recount how the calculations in the simulations were brought to where they more realistically reflect how the system would be in experiment. In addition to implementing more realistic material parameters for the silicon and substrates, the molecules used in the simulation are calculated using density functional theory [100].

We start by finding the both parts of the complex refractive index of calcium fluoride. Though the real part of the refractive index of calcium fluoride is readily found in literature [101, 102], the complex part is not so easily available. For estimating the complex part of the refractive index, we can look at the transmission of just the calcium fluoride substrate. Within the wavelength range that we are interested (6-8 µm), the transmission of the substrate is above 90 % [103] given a substrate thickness of both 2 mm. Therefore, we can assume that within this wavelength region, the complex part is incredibly small and can be neglected in the simulations.

We face a similar issue when updating the optical constants for the silicon used for the fabrication of the silicon cylinder arrays. While, there also isn't sufficient data available in the literature for amorphous silicon in the wavelength range of interest, the properties of the silicon used in the fabrication of the arrays are dependent on the deposition parameters used for the deposition of the silicon thin film such as the temperature, deposition power and pressure [104–107]. An option to directly measure the optical properties of the deposited silicon thin films is through using ellipsometry [108, 109], but again, the wavelength range of these measurements did not coincide with the region of interest for the CD measurements. To estimate the refractive index of the silicon used within the calculations, the transmission spectrum of several silicon thin films with differing thicknesses was used to estimate the refractive index in the region of interest. To clarify whether the chosen silicon parameters that were chosen were accurate, a transmission measurement was performed on the the silicon cylinder array on top of the calcium fluoride substrate and a comparison was made under the same circumstances with a computation. An agreement between these two measurements ensured that the refractive index of the silicon in the simulations matched with that of the deposited silicon. Figure 3.7 shows the experimental and computed transmission spectra for the silicon cylinder arrays over the region

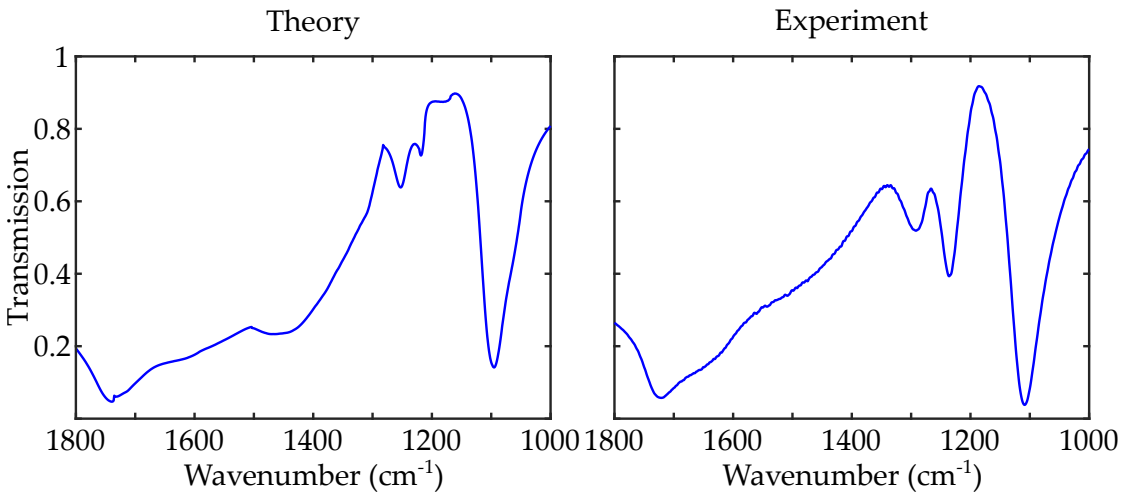

Figure 3.7: Experimental and calculated transmission spectra from the diffracting arrays are shown in the left and right panels, respectively. The transmission spectra is for an array with $h = 1100\,\text{nm}$, $r = 1920\,\text{nm}$, and $a = 5760\,\text{nm}$.

of interest where the vibrational peaks of the chiral molecules would be [110, 111]. The good match between the experimental and theoretical data shows that the parameters used in the calculations closely match the real parameters in experiment and can be implemented for the circular dichroism enhancement calculations, which will be presented with the experimental measurement in section 5.2.

The next component of the system that needs to be brought to a position in the simulations that closely corresponds to its real counterpart is the solvent that the chiral molecules are dissolved in. There are a couple of factors that need to be taken into consideration when choosing a solvent for these measurements. An obvious factor is that the solvent must not be chiral itself. Other requirements are that it must have low or no absorbance in the region of interest, the chiral molecules of interest much be soluble in the solvent and it must be compatible with the other components of the cavity as to not damage them during measurement. Another consideration is the refractive index of the solvent, as the spectral positions of the waveguide resonances are dependent on this value, but it is not so critical as the array parameters can be tailored to achieve a resonance that matches the vibrational resonance of the molecule. There have already been some studies that investigate the effect of the solvent choice on circular dichroism measurements [112–114]. With these considerations in mind, we opted to use deuterated chloroform ($CDCL_3$) as a solvent, due to it being the best choice for fulfilling the

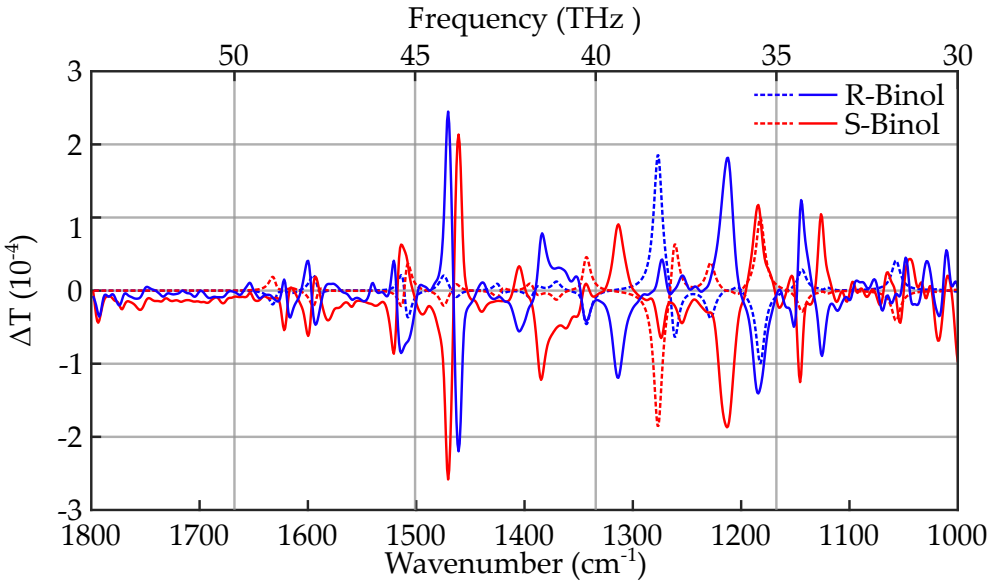

Figure 3.8: Experimental and calculated BINOL circular dichroism spectra. The blue curves represent (R)-BINOL and the red curves represent (S)-BINOL. The solid curves are for the experimental recorded spectra of BINOL molecules at a concentration of 24 mg/mL in a 200 µm path length CaF_2 cuvette. The dashed curves represent the computed CD spectrum of BINOL from the DFT calculated BINOL molecules at a concentration of 0.286 mg/mL.

above described requirements [115]. Although, there again is insufficient data in literature to correctly describe the refractive index of the solvent, we chose to set it to 1.43 as this closely matches what the value should be and further continued to neglect the absorptions.

While realistic parameters for the substrates, solvent and silicon are important to have accurate results in the simulations, an accurate description of the chiral molecules under investigation are arguably the most critical factor. Previously, the chiral medium in the simulations was modelled as a frequency-independent Pasteur medium. To refine the modelling of the chiral molecules, density functional theory (DFT) calculations were performed to determine the structure of the BINOL molecule in a deuterated chloroform solvent.

The results of the DFT calculations were then used to form T matrices of the molecules through their polarisation tensors and were subsequently used to calculate the vibrational CD (VCD) spectrum. Figure 3.8 compares the resultant calculated VCD spectrum of the BINOL molecules through the DFT calculations with the experimentally measured spectrum. When comparing the two spectra, it is obvious that there are some discrepancies but there is an overall good agreement

when comparing the spectra positions and sign of the peaks. This validates the calculated spectra for further use in subsequent simulations. The intricate details of the DFT calculations used to model the BINOL molecules are out of the scope of this work, but are detailed in the supporting information of [100].

With realistic material parameters and the informed solvent choice incorporated into the simulations the impact on the performance of the CD enhancing cavity can be evaluated. Previously, the simulated system was highly idealised, disregarding absorbance effects and frequency dependent parameters, limiting the accuracy of the predictions. The following section presents some calculated results of the enhancing properties of the cavity with the updated conditions.

3.4 Enhancement Dependence on Molecule Concentration

This section aims to detail the effect of the realistic material parameters that have been implemented into the simulations. Precisely, we look into how the enhancement capabilities of the cavity is effected when trying to enhance the CD spectrum of BINOL molecules in the vibrational infrared region.

Despite the DFT calculations to model the molecules, the following discussion on the effect of the concentration of the molecules in the solvent on the enhancement capabilities of the cavity were conducted still using a Pasteur medium, but modelled to replicate the frequency dependent response of the BINOL molecules. While not an exact replication of the response of the molecule, it can still be a sufficient description for calculations [38, 45, 61, 116]. The response of the molecules is determined through deriving the effective frequency dependent parameters; ϵ^{ω}_{eff}, μ^{ω}_{eff} and κ^{ω}_{eff}. We determine these values through considering the microscopic linear polarisability matrix α^{ω}

$$\begin{bmatrix} \mathbf{p}^{\omega}(\mathbf{r}) \\ \mathbf{m}^{\omega}(\mathbf{r}) \end{bmatrix} = \begin{bmatrix} \alpha^{\omega}_{ee} & \alpha^{\omega}_{em} \\ \alpha^{\omega}_{me} & \alpha^{\omega}_{mm} \end{bmatrix} \begin{bmatrix} \mathbf{E}^{\omega}(\mathbf{r}) \\ \mathbf{H}^{\omega}(\mathbf{r}) \end{bmatrix} = \alpha^{\omega} \begin{bmatrix} \mathbf{E}^{\omega}(\mathbf{r}) \\ \mathbf{H}^{\omega}(\mathbf{r}) \end{bmatrix}. \tag{3.5}$$

The polarisability matrix describes an electromagnetic wave, with a frequency ω, is incident on the chiral molecule at a position $\mathbf{r}$. We take this polarisability matrix and assume the quasi-static model for the dipolar resonance from a chiral object which has been obtained from [117] and assume isotropy. We then denote the polarisability matrix to be

$$\alpha^{\omega} = \frac{V}{1 - \overline{\omega}^2 + i\overline{\gamma}\overline{\omega}} \begin{bmatrix} \eta_{ee} & \eta_{em} \\ \eta_{me} & \eta_{mm} \end{bmatrix}, \tag{3.6}$$

where η_{xy} are unitless, real and semi-positive numbers. which are not dependent on frequency. $\overline{\omega} = \omega/\omega_0$ and $\overline{\gamma} = \gamma/\omega_0$, where ω_0 and γ are the spectral position and linewidth of the chosen chiral molecule resonance. V is the volume of the particle. We now bring this into SI units and a form that is dependent on the helicity of the incoming EM wave. We use equation (6.127) from [83] and define $\beta = \eta_{ee}/\eta_{mm}$, which brings equation 3.6 to the following form

$$\alpha^{\omega} = \frac{4\pi V \eta_{ee}}{1 - \overline{\omega}^2 + i\overline{\gamma}\overline{\omega}} \begin{bmatrix} \epsilon & is\frac{\sqrt{\beta}}{c} \\ -is\frac{\sqrt{\beta}}{c} & \beta \end{bmatrix}, \tag{3.7}$$

where s describes the sign of the resonance, e.g. 1 is left-handed and -1 is right-handed, and ϵ is the permittivity of the dielectric solvent that the molecules are embedded in. We now have what we need to describe the chiral molecules.

$$\begin{aligned}
\epsilon_{eff}^{\omega} &= \epsilon\left(1 + \frac{4\pi}{3}\frac{\hat{V}}{1-\overline{\omega}^2 + i\overline{\gamma\omega}}\right), \\
\mu_{eff}^{\omega} &= \mu\left(1 + \frac{4\pi}{3}\frac{\hat{V}\beta}{1-\overline{\omega}^2 + i\overline{\gamma\omega}}\right), \\
\kappa_{eff}^{\omega} &= \frac{4\pi}{3}\frac{\hat{V}s\sqrt{\beta\epsilon_{\mathbf{r}}}}{1-\overline{\omega}^2 + i\overline{\gamma\omega}},
\end{aligned} \tag{3.8}$$

where $\hat{V} = \rho V \eta_{ee}$ is a factor that enframes the influence of the molecules. We already have V and η_{ee} equation 3.6, and ρ correlates to the concentration of the molecules within the dielectric medium they are embedded in. Now that we have the equations needed to describe a more realistic version of the molecules, we can now calculate the influence of them on a CD enhancing system, like the cavities proposed here.

We investigate a particular CD resonance of the chiral molecule, BINOL. From this resonance, we can obtain ω_0, γ, s and β. This only leaves $\hat{V}$ as a variable for calculating κ_{eff}^{ω} in equation 3.7. Recalling that $\hat{V}$ is related to the macroscopic concentration of the molecules in the medium ρ, we can determine the effect of the concentration of the molecules on the CD enhancement of the system. We choose four different concentrations of $\rho = [1, 2, 3, 4]$(Concentration units), and choose the CD resonance of BINOL at a spectral position of $f_0 = \frac{\omega_0}{2\pi} = 44.21\,\text{THz}$. At this resonance peak, we determine $\gamma = 0.258\,\text{THz}$, $s = +1$, and the absolute CD signal at this resonance is $CD^{\omega_0} = 1.34 \times 10^{-3}$. The exact details of the derivations of these values are described in [51].

We present the resultant calculations that demonstrate the effect of the molecule concentration on the CD enhancement of both the double-array and single-array cavities in Figure 3.9.

The array and cavity parameters has been slightly altered compared to the designs shown in Figures 3.5 and 3.6. We have applied a scaling factor to the radius r, height h and pitch a of the diffracting arrays such that the cavity resonances lie on top of the CD resonance of the BINOL molecule. The array parameters for targeting this resonance are $h = 1082\,\text{nm}$, $r = 1574\,\text{nm}$ and $a = 4721\,\text{nm}$. The solvent of choice here was still assumed as lossless and was set with a relative

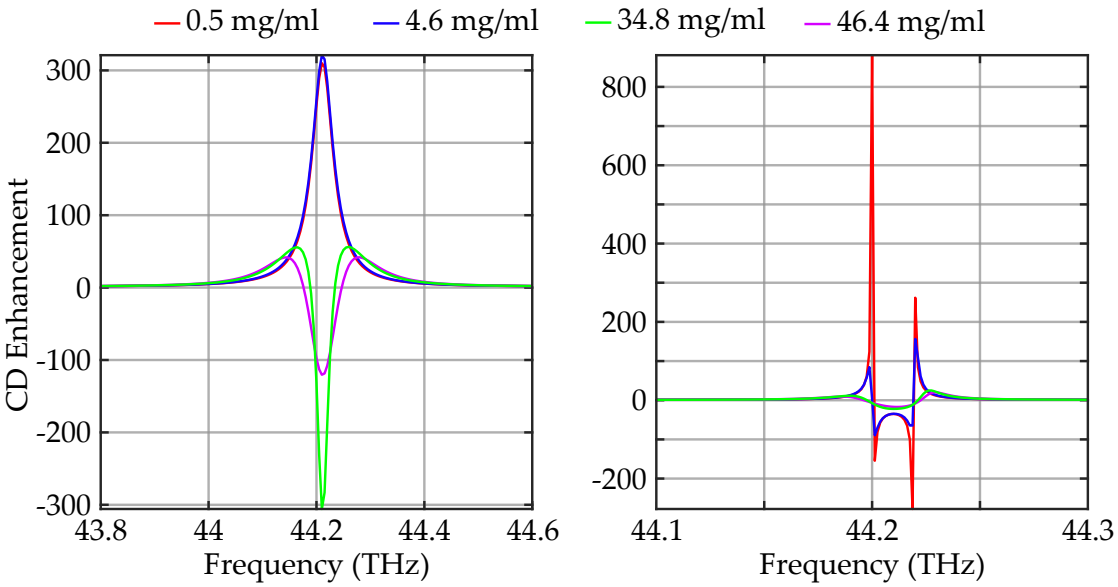

Figure 3.9: CD enhancement properties of the two cavity configurations after realistic molecule parameters are included. (a) CD enhancement of the double-array cavity for increasing chiral molecule concentration in the solvent. (b) CD enhancement of the single-array cavity for increasing chiral molecule concentration in the solvent. For better visibility due to the narrower peaks in the single-array configuration, the x-axis has been reduced. Adapted from [51].

electric permittivity of $\epsilon_s = 2.14$ Due to the slight different mode conditions between the two cavity configurations, the chosen cavity length to match the resonance mode of the cavity to the molecule resonance was 12.80 µm for the double-array cavity and 11.52 µm for the single-array cavity.

Panel (a) of Figure 3.9 shows the effect of the concentration of the chiral molecules in the solvent on the CD enhancing properties of the double-array cavity and panel (b) shows the same results but for the single-array cavity. For the double array cavity, we see that the enhancement peak does not change too greatly for the first three concentrations when considering only the absolute value of the enhancement peak, which stays at approximately 300. A noticeable change however is the flip in sign for the 34.8 mg/mL curve. Before we present an explanation for this sign change, we will initially discuss why the concentration of the molecules effects the CD enhancing performance of the cavities. On an interaction between the propagating within the cavity and a chiral molecule in the solution, if the incoming light is of, say perfectly left handedness, the out coming light after the interaction will have a component of the opposite handedness, as the properties of any molecule does not perfectly conserve the handedness of the light upon interaction. Therefore, if the number of interactions between the light and the

molecules becomes too large, the CD signal starts to degrade due to the helicity purity in the cavity degrading from these interaction. The limit of this is reached at a perfect mix of the two helicities of the light within the cavity which results in a CD signal becoming zero. In the opposite direction, with a lower concentration, the number of interactions is lower and the resultant CD enhancement is therefore not degraded. This explains the degradation of the CD enhancement but does not explain the flipping of the sign seen in panel (a). We attribute this to the splitting of the TE and TM modes within the cavity and results in this negative peak we see here. A similar effect is seen in the single-array cavity in Figure 3.6. For the highest concentration in these simulations we see a sharp drop in the enhancement by a factor of ≈ 3.

For the single-array cavity we see the similar effects but much more pronounced. Already for the 4.6 mg/mL concentration do we see a massive drop in the enhancement factor for this cavity, and even a further reduction for the two largest concentrations. For this cavity configuration, at the lowest concentration, there is an expected enhancement of ≈ 850 at the largest positive peak. Due to the mode splitting in this cavity configuration, there is also a region of negative enhancement which reaches value of ≈ -35 at it's centre most point, and even larger values at the two surrounding peaks. The splitting of the TE and TM modes is already visible in this cavity configuration due ton the silicon thin film used as one of the cavity mirrors, there we do not observe this effect appear due to the concentration dependency.

In summary, we recall that the processes taken to implement more realistic material properties into the numerical simulations and calculate the frequency dependent response of the chiral molecules under investigation. Until now, within the simulations, it was not known how the realistic molecule parameters would effect the enhancing properties of the cavity configurations presented in this work. We have observed that the introduction of the realistic material parameters has a large dependency on the concentration of the chiral molecules that are dissolved in the solvent, resulting in the degradation of the CD signal as well as the CD enhancement factors tending towards zero for increasing concentrations. This reasoning behind this effect has been attributed to excessive interactions between the light in the cavity and the molecules, leading to a decline in the helicity purity within the cavity. A similar study was implemented in [100], which showed the same relation between the molecule concentration and the enhancement factor.

Within the next chapter, I introduce the fabrication methods to construct the cavities proposed here. Thereafter, I describe the design considerations of the microfluidic chamber which considers the alignment needs and material comparabilities. The fabricated design of the microfluidic chamber is shown and the microfluidic system used to flow the solutions of chiral molecules into the

cavity for measurement is explained. The experimental apparatus and methods employed for the CD measurements is also described.

Chapter 4

4 Experimental Methods

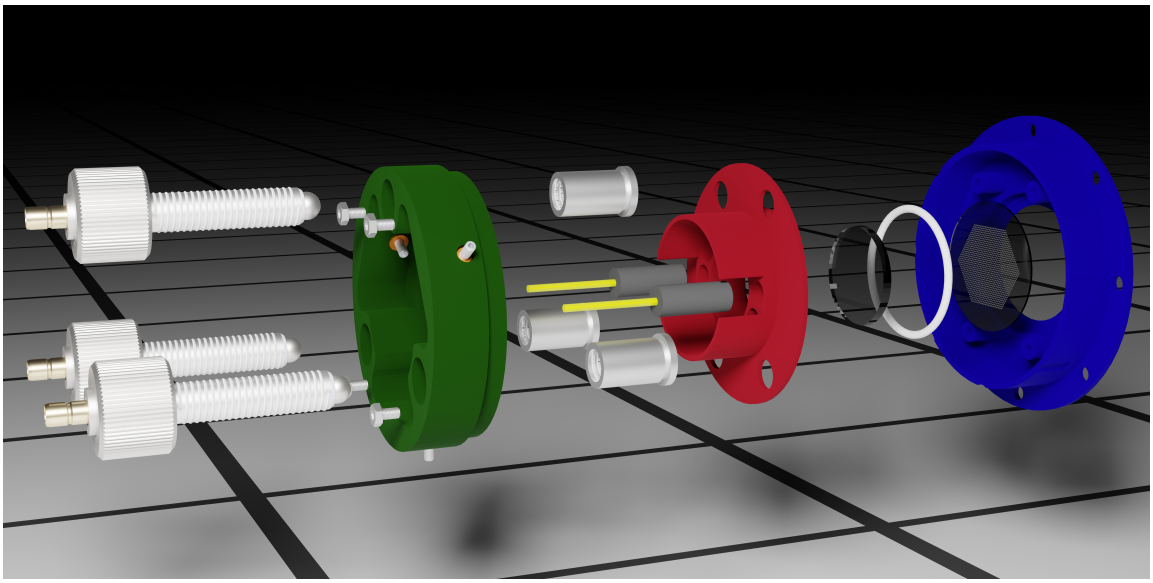

Render of an exploded view of the microfluidic chamber and silicon cylinder array cavity.

In this chapter, I recall the methods that were developed, optimised and applied in this thesis. The methods employed for the fabrication of the silicon cylinder arrays on calcium fluoride are shown, which are used as mirrors in the cavity. The design requirements for the microfluidic chamber are reported and the realisation of such a chamber is shown. The chapter is brought to an end with a description of the circular dichroism spectrometer setup used in combination with the enhancing cavity for measurements on chiral molecules at infrared wavelengths.

4.1 Silicon Film Deposition

4.1.1 Substrate Preparation

Optically polished calcium fluoride (CaF_2) substrates with diameters of 30 mm and 22 mm and a thickness of 2 mm were purchased from Korth Kristalle. The reasoning for the choice of substrate is that it must have a suitable transmission range in both visible wavelengths and mid-infrared (MIR) wavelengths. The visible regime is used for alignment purposes that will be described in chapter 5 and the MIR regime is where the chiral molecules under inspection have large absorption peaks, crucial for the CD measurements. CaF2 having a broad transmission range from around 0.13 µm to 10 µm [101] provides a more than suitable range. Another consideration was the refractive index of the substrate. To allow the light to couple into the optical cavity with high angles and retaining to a high degree the handedness of the light, the refractive index needs to match that of the solvent containing the chiral compound as closely as possible. Obviously, in experiment, matching the refractive index of the substrate and a solvent will not be possible due to frequency dependent refractive index of the different media. CaF_2 has a refractive index ranging from 1.418 at 3 µm to 1.327 at 9 µm [101], and many solvents have refractive indices within this wavelength range that can vary between 1.3 and 1.5 and are suitable for infrared experiments due to low absorptions [118–120] making this substrate choice suitable for a close enough match. An unforeseen property of CaF_2 is that the silicon film adhesion is quite poor, therefore some extra steps in the fabrication needed to be applied to ensure that the silicon film adheres to the substrate and does not delaminate or detach from the substrate in subsequent fabrication steps.

The CaF_2 substrates are received already clean and polished in lint-free packaging therefore no cleaning should be required before preparing them for the silicon deposition process. To verify this, in house cleaning was also performed for some of the substrates to check for a change in cleanliness and quality of the deposited silicon film. Multiple deposition processes showed the additional cleaning did not improve film quality when compared to films without additional cleaning. Once removed from the packaging, they were quickly blown with a stream of nitrogen to remove any possible large particles or dust and then placed into a covered glass container and into an oven at a minimum of 120 °C for at least 30 min to remove any potential residual water that could cause a reactive process when depositing the silicon film (i.e. produce silicon monoxide or silicon dioxide through reactive processes). Some additional BK7 glass substrates with the same diameter are cleaned that will be used to measure the thickness of the silicon film. The glass substrates are cleaned by being placed in acetone and being ultrasonicated at 80 °C for 15 minutes and then placed in isopropanol and ultrasonicated at 80 °C

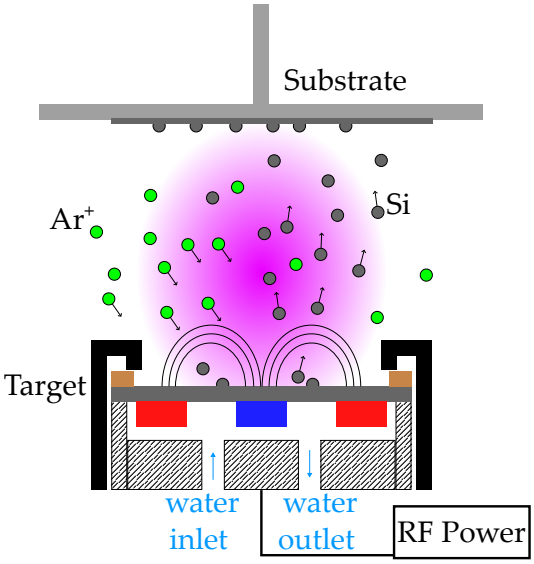

Figure 4.1: Principle of RF magnetron sputter deposition. A RF power at 13.56 MHz is applied to a water cooled magnetron sputtering source. The strong electromagnetic fields around the target cause the positively charged argon ions to bombard the target, resulting in atoms from the target material to be ejected. The induced voltage bias between the target and the substrate accelerates the ejected material towards the substrate and are deposited onto the substrate.

for 15 minutes. The glass substrates are then blow dried with a stream of nitrogen and also placed in an oven to be baked to remove residual water. The following fabrication process is also performed on the samples on glass substrates and then the silicon film thickness is measured with atomic force microscope and scanning electron microscope imaging. Next, the CaF_2 substrates are placed into a plasma oven and plasma treated in an argon atmosphere for 15 min to firstly remove any possible remaining particles on the surface and treat the surface for better adhesion during depositing. The substrates must be clean before the deposition of the silicon thin films because if there is any dust or particles on the surface of the substrates prior to the deposition, the resulting films could become uneven with local maximums in the film or cause detachment of the silicon from the substrate [121].

4.1.2 Magnetron Sputter Deposition

The silicon thin films are deposited using magnetron sputter deposition. A depiction of the magnetron sputtering system is shown in Figure 4.1. The prepared substrates are placed into a BOC Edwards Auto 500 Vacuum Coater chamber at

a distance of 8.5 cm from the silicon target. The chamber is brought down to a base pressure of at least 1×10^{-6} mbar to remove atmospheric gas, preventing any reactive processes. Once the base pressure is reached, inert Argon gas is leaked into the chamber as is it a suitable inert gas that is widely used for non-reactive material deposition. The pressure inside the chamber is controlled via a mass flow controller that regulates that amount of argon that is leaked into the chamber. Due to the nature of silicon, the RF power applied is slowly ramped up and down at a rate of 10 W/min to prevent any damage to the target through thermal shock. The silicon is deposited in two steps, the first step is at a radio frequency (RF) power of 200 W and a pressure of 8.31×10^{-3} mbar which resulted in a deposition rate of 3.19 nm/min. This first step is at a lower deposition rate compared to the rest of the process which also allows for the silicon to better adhere to the CaF_2 substrate. The second step of the deposition is at a power of 200 W and a pressure of 1.74×10^{-3} mbar resulting in a deposition rate of 5.56 nm/min. The deposition is ran until a film thickness of 1550 nm is measured with the quartz crystal thickness sensor inside the chamber. Once the target thickness has been achieved, the power to the silicon target is reduced to 0 W at a rate of 10 W/min. The finished silicon film samples are then left in the chamber under vacuum until they reach room temperature. Once room temperature has been reached, the chamber is then brought back to ambient pressure by flowing nitrogen gas into the chamber. The samples are then placed into sealed containers to prevent any contamination from dust in the air when being transported to a clean room for the next fabrication steps.

4.2 Silicon Cylinder Array Fabrication

4.2.1 Optical Lithography

The following optical lithography processes are performed in ISO 6 and ISO 7 cleanroom labs to minimise contamination from particulates in the atmosphere. Dust and debris contamination on the samples during the lithography steps can lead to defects in the photoresist films, resulting in uneven or unresolved structures after development and etching.

Substrate Cleaning

After the samples have been transported to the cleanroom, the samples are again cleaned in an ultrasonic bath at a low power in spectroscopic grade acetone for 10 min then in spectroscopic grade isopropanol for 10 min. The substrates are then blow dried with a stream of nitrogen and finally baked on a hotplate at 120 °C for 5 min.

Photoresist Spin Coating

The first step of the lithographic process is spin coating a thin film of photoresist onto of the sample. Here, a negative tone UV sensitive photoresist is chosen, which is AZ 15nXT (115 CPS) from Microchemicals. The resist was spincoated onto the substrates in a two step process. The first step is to accelerate the sample at a rate of 6000 RPM/s to a speed of 500 RPM for 5 s which is to evenly spread the resist over the substrate. The second step is to accelerate the sample at the same rate to a speed of 8000 RPM for 30 s to bring the resist film to the desired thickness by throwing off additional resist. This gives a desired film thickness of 2250 nm. After the spin coating, the sample with resist film is placed on a hotplate at 110 °C for 120 s, this is known as a softbake or prebake step. The purpose of this prebake is to remove any remaining solvent in the resist and to dry it out to prevent any sticking to the photomask in the next step. Before the resist was exposed with UV light, a wait time of 10 minutes is done to allow the resist to thermally stabilise.

Resist Exposure

The resist coated samples are placed into a Karl Suess MA6 mask aligner for exposure. The photomask is brought into direct contact with the resist surface using 'hard contact' mode where a stream of nitrogen is used to push the substrate

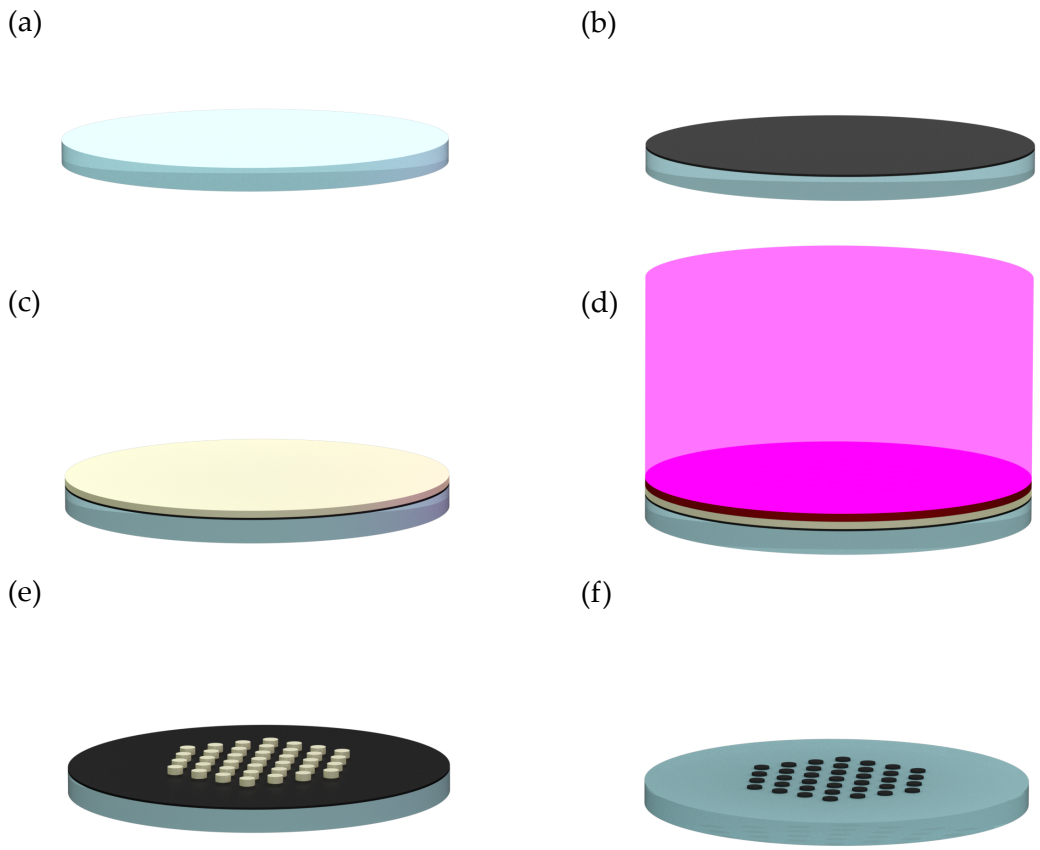

Figure 4.2: Illustration of the workflow from bare substrate to array fabrication. (a) A bare, clean CaF_2 substrate. (b) A silicon thin film is deposited onto the substrate through RF magnetron sputter deposition. (c) A negative tone resist is spincoated on top of the silicon film. (d) Exposure of the photoresist with UV light using a mask aligner system. A photomask is placed directly on top of the photoresist to only expose the desired pattern. (e) After development of the exposed photoresist. Due to the negative tone photoresist, only the exposed areas remain after development. (f) Resulting silicon disk array after etching and photoresist stripping.

against the photomask surface, this is to ensure that there is no gaps between the resist and photomask. Gaps between the resist and photomask will allow the light to diffract and the exposed resist will have defects such as the structures being larger than indented and having 'mouse-bite' artefacts. The resist is exposed with UV light at a wavelength of 365 nm with an intensity of $13\,mJ/cm^2$ for 3.9 s, which accumulates to a dose of 50 mJ. For this chosen resist, which is a chemically

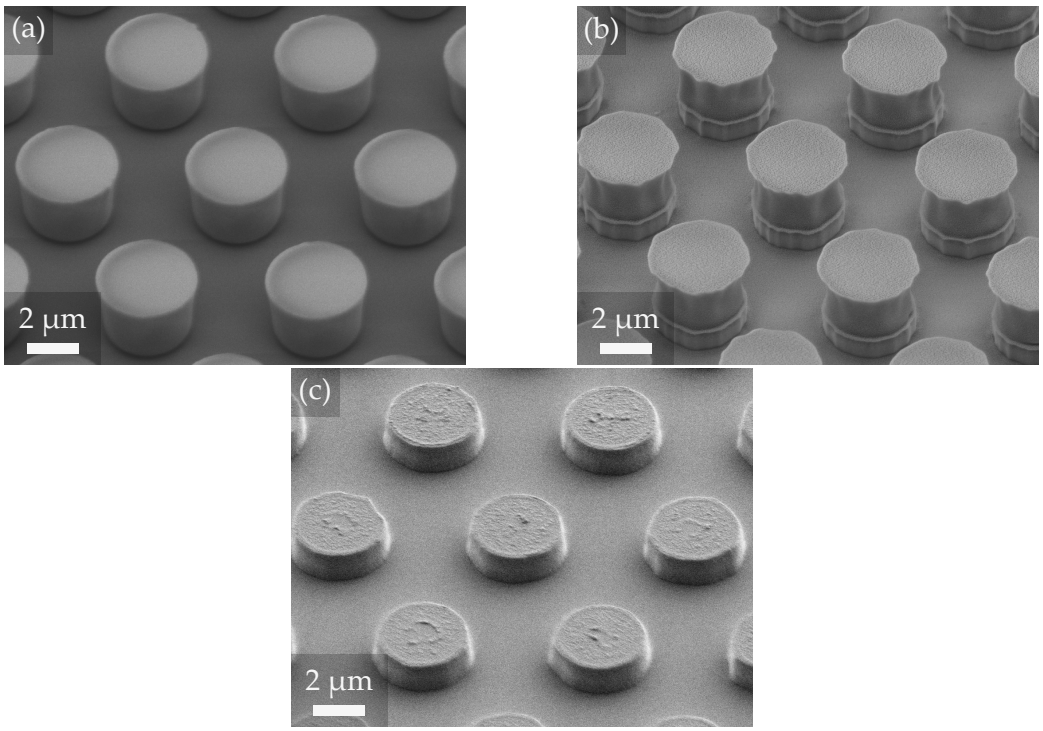

Figure 4.3: Scanning electron micrographs of the silicon cylinder arrays at different steps of the fabrication process. (a) Photoresist cylinder array after exposure and development. (b) Photoresist and silicon cylinders after etching. The resist structures were developed and the silicon was etched to show the transfer of the artefacts from the photoresist to the silicon. (c) Silicon cylinders after etching and removal of the photoresist through oxygen plasma ashing and chemical resist stripping. Without sufficient stripping, remnants of the photoresist remain on top of the silicon.

amplified resist, the UV exposure photoreaction does not completely cross-link or harden the resist but only creates the catalysts required to initiate the cross-linking. Thus the photoreaction process to complete entirely, a post exposure bake (PEB) is required. For this resist, a bake at 120 °C for 60 s completes the cross linking and the exposed areas become hardened. The mouse-bite artefacts can also appear due to overexposure of the photoresist. Figure 4.4 shows two resultant resist structures for two different exposure times with the same development time. Panel (a) shows the developed structures for a exposure time of 4.6 s, and clearly shows overexposure from the uneven edges and a slightly larger diameter at the top of the cylinders. When the exposure time is reduced by 0.7 s, the uneven edges of the cylinders are removed and the developed structures are the intended diameter of 1570 nm.

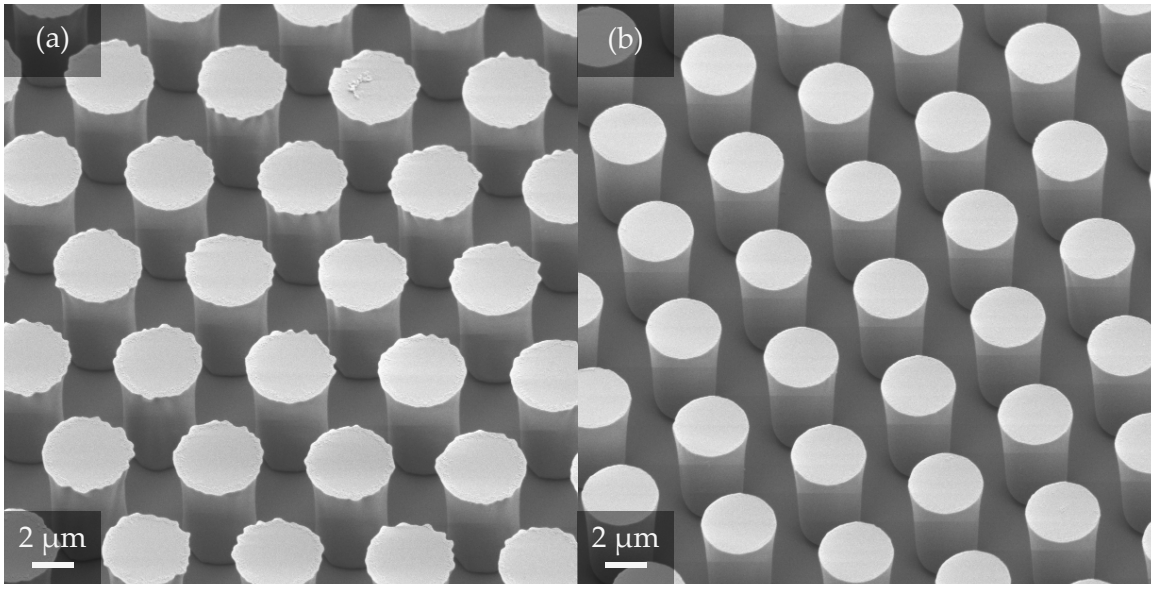

Figure 4.4: SEM micrographs of the AZ15 nXT photoresist used with different exposure times. (a) An exposure time of 4.6 s, resulting in a dose of 60 mJ. The overexposure resulting the mouse-bite artefacts, giving an uneven edge. (b) An exposure time of 3.9 s, resulting in a dose of 50 mJ.

Development

After the exposure and PEB of the resist, the samples need development to reveal the exposure structures and remove the residual unexposed resist. The development step is a very precise process as there are many factors that contribute to the development rate of both the unexposed resist and exposed resist such as: temperature, development time, type of developer used and if the developer has any additives included in its formula. The developer used for this resist is AZ326 MIF, with MIF standing for metal-ion-free. The developer is 2.38 % tetramethylammonium hydroxide (TMAH) in H_2O. The samples were submerged in the AZ326 MIF developer for 30 s at room temperature. To stop the development, the samples are immediately submerged in de-ionised water at room temperature and are then dried with a stream of nitrogen. The developed structures are inspected with a microscope with 50× and 100× magnification to check for quality.

4.2.2 Etching

The samples are then etched to transfer the pattern from the photoresist into the silicon. There are two types of etching; wet etching and dry etching: Wet etching

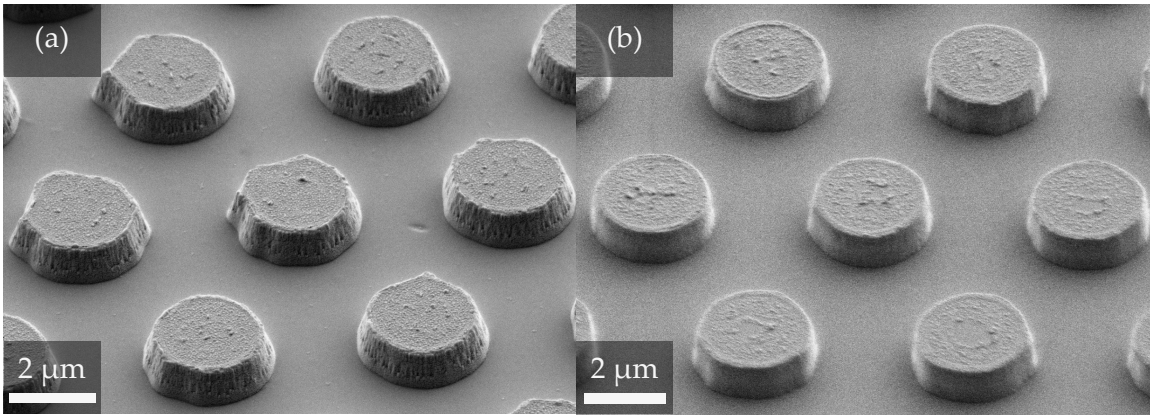

Figure 4.5: SEM micrographs of the silicon cylinders with different RF etching powers. (a) Resulting structures for an RF power of 30 W. This chosen power gave a more isotropic etching profile, producing slanted sidewalls. (b) Resulting structures for an RF power of 40 W. This power gave a better anisotropic etching profile,producing more vertical sidewalls.

is uses a chemical that attacks the material and removes it. Wet etching is a very isotropic process, it will remove material that is underneath the photoresist mask, giving a difference between the size of the photoresist structures and the silicon structures. Dry etching instead uses a plasma to remove material. In this work, a dry etching technique, inductively coupled plasma reaction ion etching (ICP-RIE) is used. In the ICP-RIE process, a high density plasma is excited through an oscillating electromagnetic field that is generated by applying power to inductive coils that surround the chamber at a frequency of 13.56 MHz. Simultaneously, a separate RF power source is connected to the cathode that is below the sample to be etched, which generates a DC bias which accelerates the ions within the plasma towards the samples. ICP-RIE etching incorporates a combination of physical and chemical etching processes to remove the material [122]. ICP-RIE etching processes can produce high quality etched structures through the tunability of the plasma density (ICP power), ion bombardment energy (RF power), and process gas selection, which collectively callow precise control over the etch rate, etch anisotropy and selectivity of the process [123, 124].

An Oxford Plasma Technology Plasmalab 100 ICP180 is used for the etching of the silicon. The chosen process implements a hydrogen bromide (HBr) gas to etch the silicon. HBr is leaked into the chamber with a flow of 15 SCCM giving a chamber pressure of 1 mbar. The RF power is set at 40 W and the ICP power is set at 600 W. The samples were etched for 15 min to remove the entire thickness of the silicon.

Figure 4.5 shows the variation on the results of the etched structures through varying the etching parameters, namely the RF power. This controls the bias voltage that accelerates the ions and radicals towards the samples, which controls

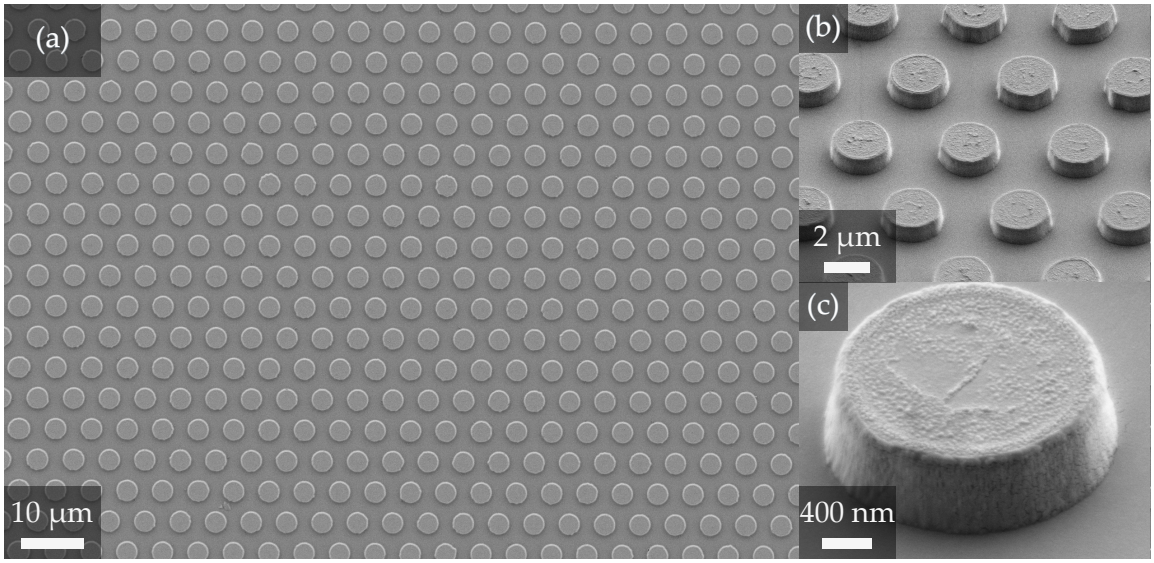

Figure 4.6: SEM micrographs of etched silicon cylinders. (a) Micrograph depicting a section of the total the silicon disk array on a CaF_2 substrate. The entire array consists of over 2 million individual silicon cylinder elements. (b) Showing the silicon cylinder elements that make up the diffracting array from an 45° angle. (c) Singular silicon cylinder element that makes up the diffracting array.

the etch rate and profile. Optimisation of this parameter helps create a vertical sidewall profile. Furthermore, if this power is too large, it will result in the etching becoming too aggressive and damaging the substrate and silicon cylinders.

4.2.3 Resist Stripping

The final step is to remove the remaining resist structures after etching. After the etching steps, the resist becomes hardened due to the excessive heat and ion bombardment, rendering it difficult to remove. Therefore, submersion in a resist stripper is not sufficient. To efficiently remove the photoresist structures without damaging the silicon structures, RIE-ICP is used for the first step of the resist removal by ashing the resist in an O_2 plasma for 5 min. This step removes about 95 % of the resist and only side walls remain as they have been heavily implanted by ions and silicon during the etching. To remove this requires the use of two solvents and ultrasonification. The samples are placed in dimethyl sulfoxide (DMSO) in an ultrasonic bath at 60 °C for 15 min and then in Technistrip NI555 (Technic, purchased from Microchemicals) also at 60 °C for 15 min. The fabricated silicon cylinder arrays are presented in Figure 4.6.

Scanning electron micrographs of different fabrication steps are shown in Figure

4.3. Within every step of the fabrication process, there can be defects that appear in the structures that can arise due to particles on the sample during lithography or edge beads in the photoresist leading to gaps between the photomask and photoresist [125]. Panel (b) in Figure 4.3 shows the silicon structures directly after etching. Edge effects from the structures in the photoresist are directly transferred into the silicon structures, this is prevented through sufficient cleaning of the samples before silicon deposition and before the photolithography process. To compensate for the edge bead effects, the spin-coating process was optimised to remove the edge bead. Panel (c) shows the silicon cylinders after etching and removal of the photoresist, with insufficient photoresist removal, some remnants remain on top of the cylinders. Extended resist stripping is required to remove stubborn residual resist.

4.3 Microfluidic Setup

This section details the last component needed for the microcavity that will be used for the enhanced detection of chiral molecules. Here, the design for the microfluidic chamber as well as the components used to control the flow of the solution of chiral molecules is described.

4.3.1 Requirements

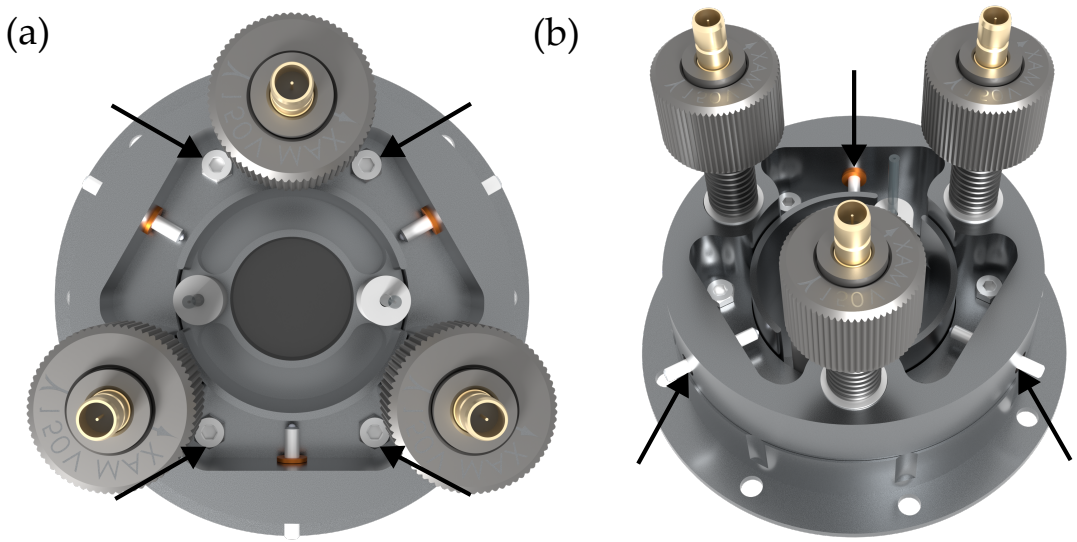

Figure 4.7: Computer rendering of the microfluidic chamber. (a) Top view of the microfluidic chamber. Four M2 hex screws (indicated by the black arrows) are used to hold the entire assembly together. Two fine adjustor screws (indicated by the black arrows) and a spring are used for lateral alignment between the two mirrors in the case of the double array cavity configuration. (b) Oblique view of the microfluidic chamber. Three piezoelectric actuator screws (Polaris-P20A, Thorlabs) are used for parallel alignment of the two mirrors and fine tuning of the cavity length.

The microfluidic chamber, which houses the two mirrors used for the microcavity, seems a simple component, but is crucial to the functionality of the whole device. The chamber needs to be able to hold a volume of solvent or solution of chiral molecules, allow for accurate alignment of the two cavity mirrors and enable variation of the cavity length with a precision of $<50\,\text{nm}$. Additionally, alignment components must be present for aligning the two cavity mirrors in the X-Y axis as well as being able to rotate one of the mirrors with respect to the other such that

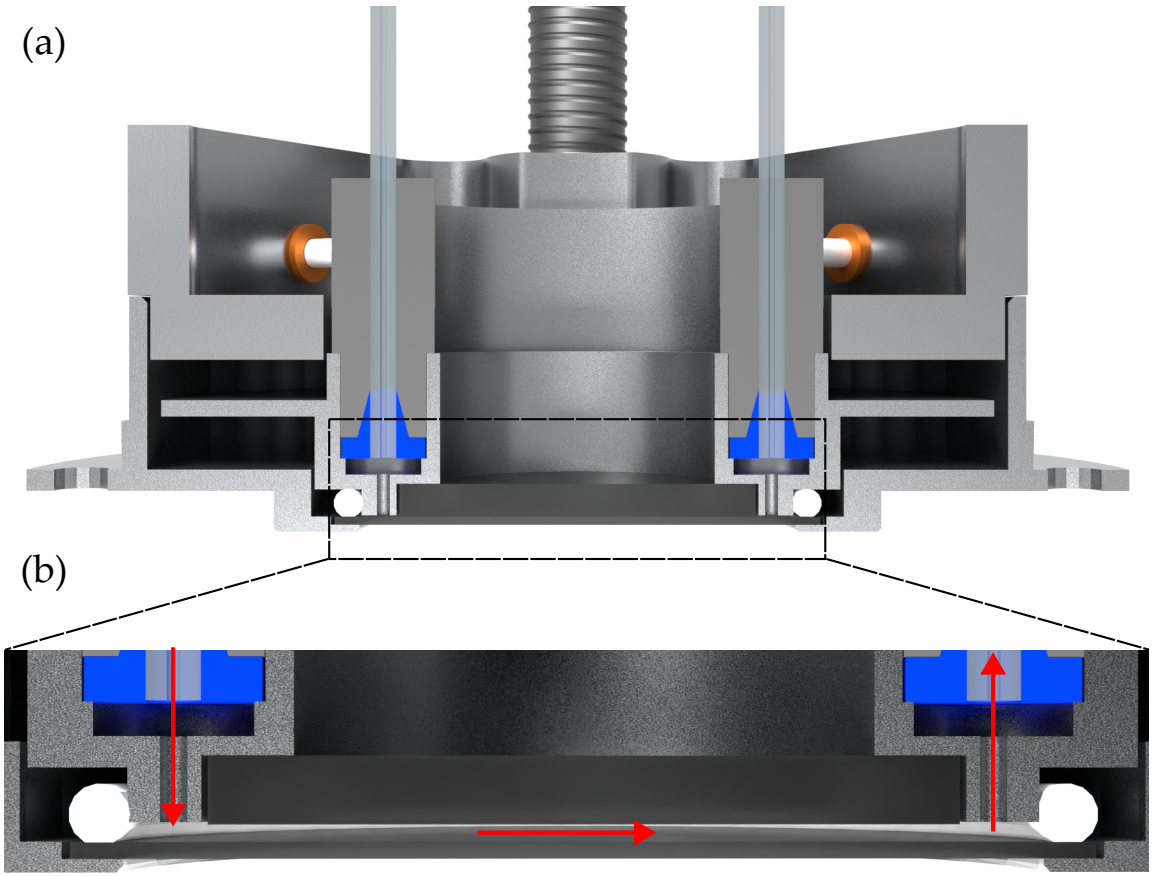

Figure 4.8: Computer rendering of a cross-sectional view of the microfluidic chamber. (a) Cross-section view of the full chamber, showing the two lateral alignment screws and one of the piezoelectric actuators. The chamber is sealed with an O-ring. (b) Zoomed in section of the microfluidic chamber. The red arrows signify the flow direction of the solution through the chamber.

if the cavity is in the 'double-array' configuration, it is possible to align the two arrays such that the whole device is achiral.

4.3.2 *Metal Microfluidic Chamber Design*

The chosen design for the microfluidic chamber is depicted in Figure 4.7, and a cross-sectional view to demonstrate the flow through the chamber is shown in Figure 4.8. The chamber is fabricated out of aluminium in 3 separate pieces, a bottom, middle and top section of the chamber. The bottom section is to hold one of the mirrors with a larger diameter (30 mm) in place and also has four raised cylinders with threaded holes to connect to the top section to fasten the three

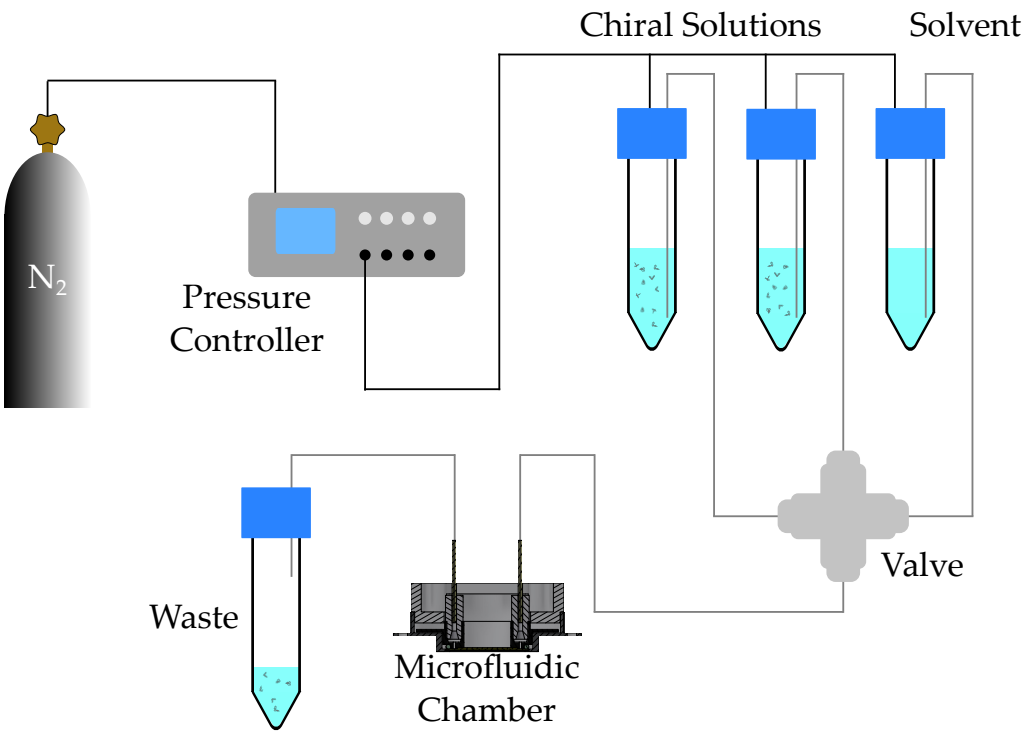

Figure 4.9: Schematic of the microfluidic system used for flowing chiral molecules through the microfluidic chamber. A nitrogen cannister is connected to a pressure controller (Elveflow OB1 MKIII). The pressure controller is used to pressurise the reservoirs filled with the chiral solutions and solvents. The pressure in the reservoirs flows the solutions to out of the reservoirs. The 3-to-1 valve is used to choose which solution is to be flown through the microfluidic chamber for measurement. After measurement, the waste solvents are collected in a reservoir.

sections of the chamber together. The middle section holds the smaller diameter mirror (22 mm) and an O-ring that functions to seal the microfluidic chamber when all parts are screwed together. The O-ring used is of a perfluoroelastomer material which is highly chemically resistant and has an inner diameter of 26.7 mm and a thickness of 1.78 mm. Additionally, the middle section has two $1/4 - 28$ threaded connectors for the microfluidic inlet and outlet. The final top section has four holes, which four M2 hex screws to assemble the three sections together, with the middle section being sandwiched between the two. The top section is also designed such that three piezoelectric actuators can be inserted into the top section. These actuators are for aligning the two mirrors and adjusting the cavity length. Also, they hold the middle section in place when the top and bottom sections are screwed together. The chosen piezo actuators are the Polaris-P20A as they have a suitable size to fit within the chamber and have a suitable resolution of

0.013 µm for a 0.1 V step. All three piezo actuators are controller with a MDT693B piezo controller, also purchased from Thorlabs. Again in a triangular formation, there are two micrometer screws (F2ES15 from Thorlabs) and a singular spring are implemented to be able to move only the mirror attached to the middle segment, such that for the double-array cavity formation, the two arrays can be aligned.

4.3.3 Microfluidic System

A schematic of the described microfluidic system is illustrated in Figure 4.9. In this microfluidic system, the chiral solutions that are under investigation are placed in air tight reservoirs. Nitrogen gas is used in combination with a pressure controller, here an OB1 MKIII, to control the flow of the solutions through the system The nitrogen gas supplies the pressure controller with an overpressure, and a piezo-actuated valve combined with a pressure sensor within the controller is used to regulate the output pressure that is applied to the reservoirs through the tubings that flow the gas out of the controller to the reservoirs. The maximum pressure that the windows can withstand is approximately 4 bar, and to prevent any rupturing of the windows of the microfluidic chamber, a pressure of 200 mbar is chosen. The caps on the reservoirs feature socket for outlet tubing that can be lowered into the solution, and the pressurisation of the reservoirs forces the solutions to flow through the tubings. Due to the single channel of the pressure controller, all of the reservoirs are pressurised simultaneously and therefore all of the solutions will be flowing through the tubings. To have control over which solution is flown through the microfluidic chamber, a 3-to-1 selection valve is implemented into the system. After the selection valve, the solution flows through the microfuidic chamber and finally into a waste reservoir.

4.4 Vibrational Circular Dichroism Spectroscopy

4.4.1 Preparation of Chiral Molecule Solutions

Solutions of 1,1'-Bi-2-naphthol (BINOL) molecules were prepared in five distinct concentrations to demonstrate the concentration dependence on the cavity performance. The highest concentration for the measurements, aimed to be 49 mg/mL, was achieved by dissolving 49.01 mg of S-BINOL and 49.45 mg of (R)-BINOL in 10 mL of deuterated chloroform ($CDCl_3$). To ensure complete dissolution of the molecules, the solutions were ultrasonicated for 5 min. This method was repeated for all of the subsequent concentrations.

For the second concentration, 10.26 mg of (R)-BINOL and 10.09 mg of S-BINOL were each dissolved in 10 mL of $CDCL_3$. The third concentration was prepared by taking 2 mL of both the R- and S-BINOL solutions further diluting them with another 4 mL of solvent, resulting in a concentrations of approximating to 5 mg/mL.

For the final two concentrations, 9.1 mg of (R)-BINOL and 8.6 mg were dissolved in 6 mL of solvent. This produced a concentration of 1.517 mg/mL and 1.433 mg/mL for R- and S-Binol, respectively. Again, 2 mL of these two enantiomer concentrations are taken and both are diluted by a further 10 mL of solvent to achieve the final concentrations in this study, which are aimed at 0.3 mg/mL.

4.4.2 Fourier Transform Vibrational Circular Dichroism Spectrometer Setup

This section will describe the procedure carried out for the spectroscopic measurements on chiral molecules. As previously discussed, the optical components that were used to construct the microcavity were specifically chosen due to their transparency in the mid-infrared region. The chosen period of the arrays is 5.4 µm, allowing for diffraction orders to propagate from wavelengths of 6.7 µm.

The chosen instrument to perform such measurements was a Tensor 27 fourier-transform infrared (FTIR) spectrometer (Bruker Optik GmbH), combined with a polarisation modulation module (PMA50, Bruker Optik GmbH). The fourier transform circular dichroism spectrometer is based on the concepts proposed by Nafie et al. [126, 127]. Figure 4.10 depicts the lightpath in the PMA50 module with the components used for collection and analysis of the recoded data. The function of these components are explain at the end of this section. The light, as an interferogram, travels as a collimated beam from the main spectrometer to the PMA50 module. Circular polarisation of the light is achieved through a ZnSe linear polariser at an angle of 45° and a photoelastic modulator (PEM) that

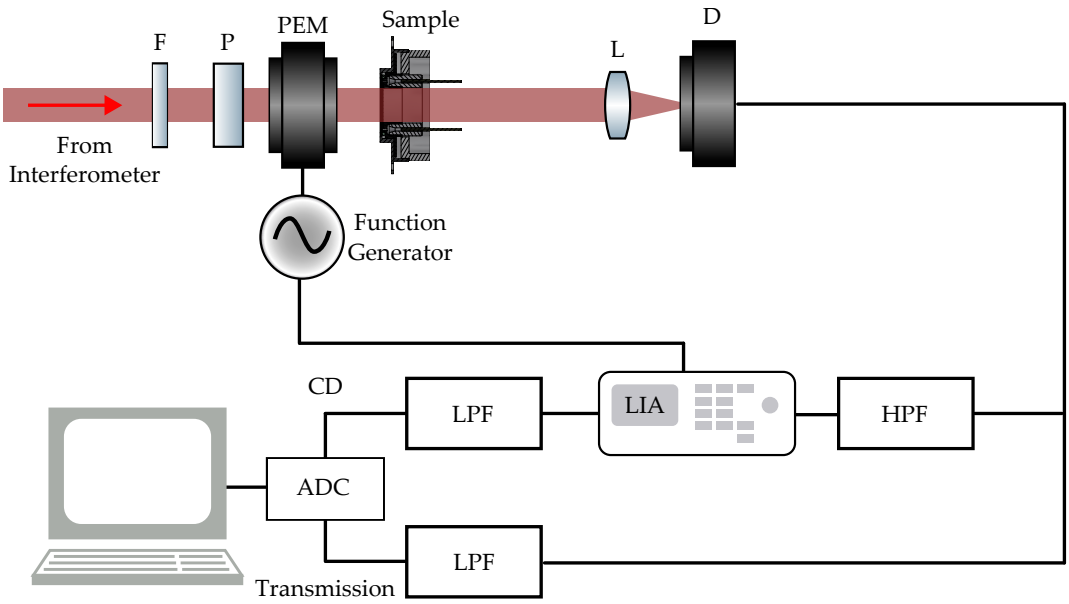

Figure 4.10: Schematic of the optical path for the circular dichroism. From the interferometer, collimated light travels into the polarisation modulation component. The light firstly passes through a filter (F), which truncates wavelengths below 5.5 µm. Thereafter, the light passes a combination of a linear polariser (P) and a photoelastic modulator (PEM) that produces circularly polarised light, which alternates between right- and left-handed CPL at the set PEM frequency. Finally, the light passes through the sample and is focused by a lens (L) onto the detector (D). The digital signal measured by the detector is split into two paths, one for the transmission signal and one for the differential signal. The transmission signal is only processed by a low-pass filter (LPF), while the differential signal is processed by a high-pass filter (HPF), then is demodulated by the lock-in amplifier (LIA) and finally also passes a LPF. Both the signals are converted to a digital signal by the analogue-to-digital converter (ADC).

modulates the polarisation of the light between right- and left-handed circular polarisation at a rate of 50 kHz. After interacting with the sample, a focusing lens is used to focus the light onto a liquid nitrogen cooled mercury cadmium telluride (MCT) detector. A low pass optical filter is implemented in the optical path to remove all wavelengths below 5.5 µm to help improve the signal-to-noise ratio of the measurement. The spectrometer uses a dual channel acquisition to simultaneously record both the sum and the difference signal. The sum signal is the normal transmission spectrum of the sample and the difference signal is the circular dichroism signal, i.e. the difference in transmission between right-handed CPL and left-handed CPL. The sum signal passes through a low-pass filter (LPF) and is sent to a computer for analysis. The difference signal firstly passes through a high-pass filter, then the reference signal from the PEM is used with the lock-in

Amplifier (LIA) to extract the difference signal and finally it also passes through a LPF. The signal recorded is then sent to a PC so that the various measured spectra can be extracted from the interferograms [128, 129].

4.4.3 *VCD Measurement Workflow*

Here will be a concise overview of how the data for the VCD measurements on the Binol molecules in the enhancing optical cavity were accumulated. The solutions of chiral molecules are prepared as described in section 4.4.1. For a measurement on a set concentration of the two enantiomers, the two solutions of molecules are loaded into the microfluidic system as described in Figure 4.9. A spectral range for the measurement was defined from 1000 cm^{-1} to 1800 cm^{-1}, where the spectral resolution of the spectrometer was 4 cm^{-1}. Due to the weak VCD signal, an integration time of 20 min measured to obtain a sufficient signal-to-noise ratio.

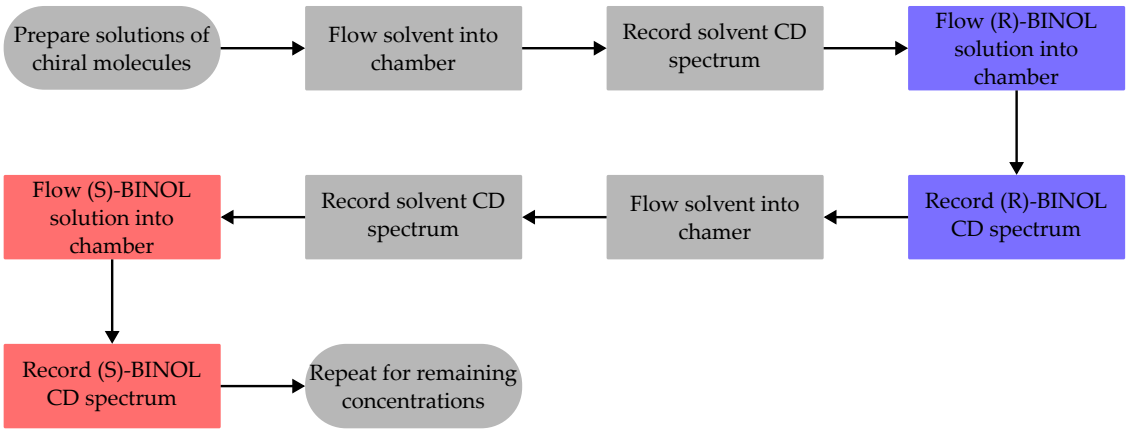

Figure 4.11: Workflow for recording circular dichroism measurements in the metasurface cavities. Firstly the solutions of chiral molecules are prepared. Pure solvent is flowed into the microfluidic chamber to firstly ensure a clean chamber and to record the CD spectrum of the solvent. Recording the solvent spectra is to ensure sufficient cleaning of the chamber and have the solvent spectra as a baseline to subtract. Next, the (R)-BINOL solution is flown into the chamber and the CD spectrum is measured, followed by another cleaning with the solvent and a measurement to check sufficient cleaning. Finally, the (S)-BINOL solution is flown into the chamber and the CD spectrum is measured. The process is then repeated for all subsequent concentrations.

The whole step-by-step workflow for recording the CD data of the two BINOL

enantiomers is illustrated in Figure 4.11. The microfluidic system is used to firstly flow the pure solvent into the cavity, then a measurement is performed to asses if there is any signal coming from chiral molecules that could be present within the cavity. When this is confirmed, the first concentration of chiral molecule can be measured. The valve in the microfluidic system is used to allow the solution of (R)-BINOL molecules to flow into the chamber. This allows simultaneously viewing of the signal reaching the detector until peaks from the BINOL molecules are present in the spectrum. When the peaks are seen, the flow is halted and a measurement is started. After the measurement on the (R) enantiomers is completed, the solvent is again flown into the chamber and measurement is performed to ensure sufficient cleaning of the chamber. Finally, the solution of S-BINOL molecules is flown into the chamber using the microfluidic system and a measurement is recorded. Before moving to the next concentration of the molecule, solvent is again used to clean the chamber and a measurement is done. The same procedure is repeated for the next four concentrations of the chiral molecules.

5 Chapter 5
Experimental Results

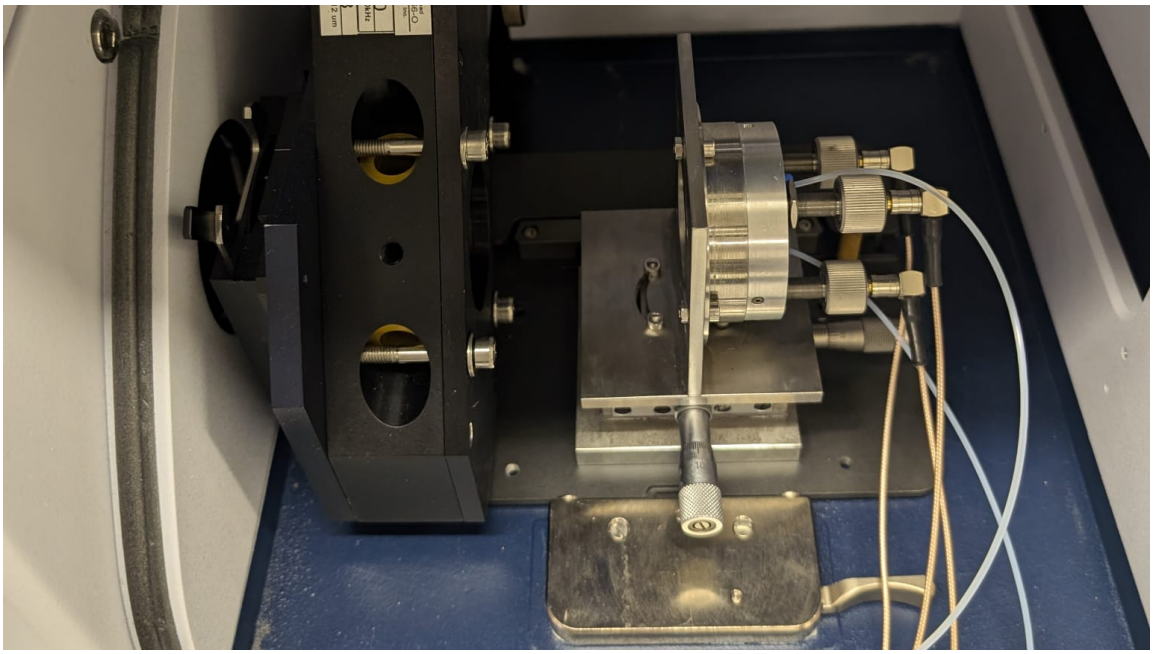

Photograph of the manufactured metasurface cavity in the sample compartment of a vibrational circular dichroism spectrometer

In this chapter, I present the experimental results that arose from the fabrication of the metasurface optical cavity to probe the response of of chiral molecules in solution. To achieve these results I employed the processes described in chapter 4. Here, I present the investigation of the VCD artefacts that emerge from the diffracting array and give an explanation to the origins of these artefacts. Thereafter, I will show the measurements performed on the chiral molecule, BINOL using the enhancing cavity. The data obtained for both enantiomers of the BINOL molecules is presented for five different concentrations combined with a discussion of these results. Finally, I will conclude the chapter with a discussion of potential future ideas that could improve the measurement procedure and results.

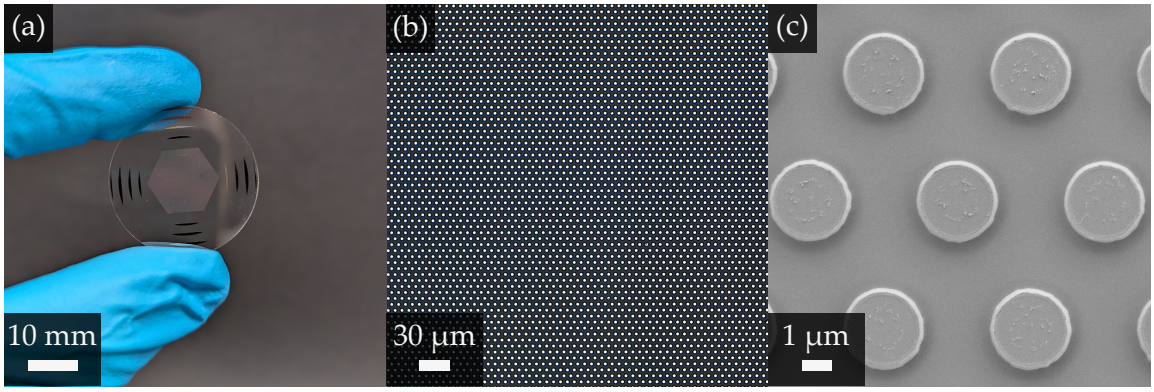

Figure 5.1: Fabricated silicon cylinder array on a CaF_2 substrate. (a) Optical photograph of the CaF_2 arrays fabricated on a 30 mm calcium fluoride substrate. (b) Digital light-microscopy image showing many elements of the silicon cylinder array, the large field of view shows good homogeneity of the fabricated structures. (c) Scanning electron micrograph of seven elements of the silicon cylinder array.

5.1 Vibrational Circular Dichroism Artefacts from Diffracting Arrays

Before looking into the experimental results on the measurements of chiral molecules in an optical cavity. We must first assess the vibrational circular dichroism (VCD) artefacts that arise from the diffracting arrays themselves through misalignments. The arrays are fabricated as described in section 4.2 and two optical images of the arrays are shown in Figure 5.1. The optical images show no clear defects in the fabricated structures that could result in artificial CD signals, also pointing to the artefacts arising from misalignments. The parameters for the diffracting array are as follows, radius $r = 1570\,\text{nm}$, height $h = 1080\,\text{nm}$, pitch $a = 4690\,\text{nm}$, which results in a centre-to-centre distance between the cylinders in the array to be 5415 nm. The fabricated silicon cylinder array is shown in Figure 4.6. The artificial VCD signals from the diffracting arrays were characterised by using both a rotating sample holder to rotate the array around the optical axis and a gimbal mount to vary the angle of incidence of the light onto the array. Additionally, I show how a misalignment between the two cavity mirrors can lead to artifical signals. We will look into how rotating the array around the optical axis, while illuminating from both the front and back side, as well as varying the angle of incidence of the light onto the array will influence the artefact arising from the diffracting array.

The setup used for measuring the artefacts is depicted in Figure 4.10, but with a different sample holder. The array is fastened onto the holder and positioned

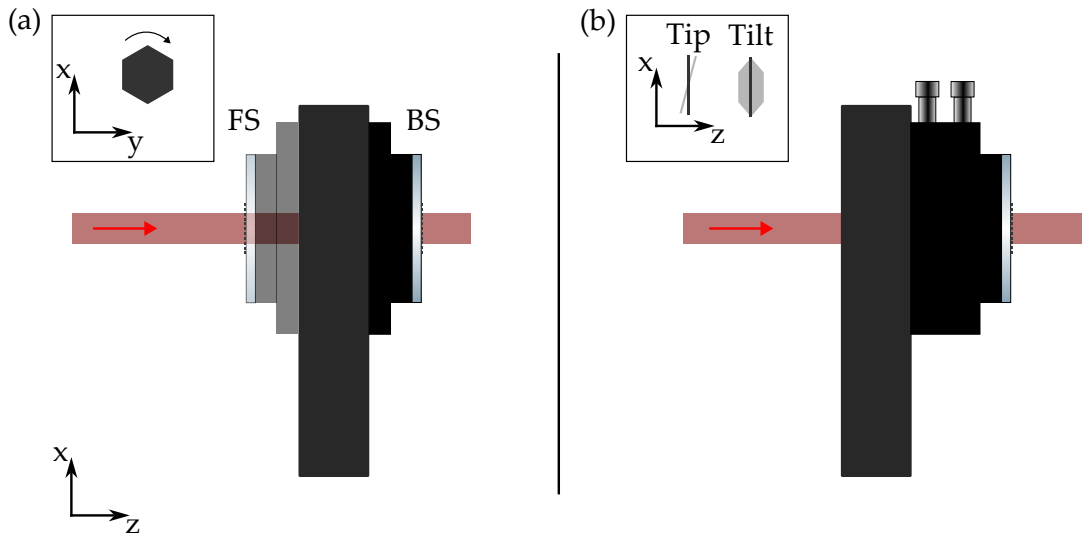

Figure 5.2: Illustration of the holders used for measuring the VCD artefacts from the diffracting arrays on top of a CaF_2 substrate. (a) The holder used for rotating the sample around the optical axis. Back side (BS) configuration is for the illumination on the CaF_2 substrate and front side (FS) is for illumination on the silicon array. The inset denotes the rotation of the sample. (b) The holder used for the rotation of the sample to alter the angle of incidence of the light on the sample. The inset denotes the tip and tilt rotation directions.

such that the long axis of the hexagonal array is vertical and the holder is set to 0°. the sample holder is shown in panel (a) of Figure 5.2.

5.1.1 *Rotation Around Optical Axis*

We initially place the sample in an orientation where the light hits the diffracting array first, as shown in panel (a) and record the VCD signal at angles of 0°, 90°, 180°, and 270°. The sample then gets flipped so that the light impinges onto the CaF_2 substrate first, shown in panel (b) of Figure 5.2, and the measurements are repeated for the same sample rotation angles. The measured VCD artefacts from the diffracting array are shown in Figure 5.3. The data recorded in the spectrometer is the difference in transmission of the sample between the left- and right-handed CPL, therefore the y-axis has been labelled ΔT in all of the measurement plots. Due to the design of the arrays, it is actually unexpected that such large artefacts occur since the arrays are designed to be achiral. To find an explanation to why these artefacts arise, let us firstly take a look at the measured artefacts. The left panel is the illumination onto the substrate first and the right panel is the illumination onto the diffracting array first. Let us focus

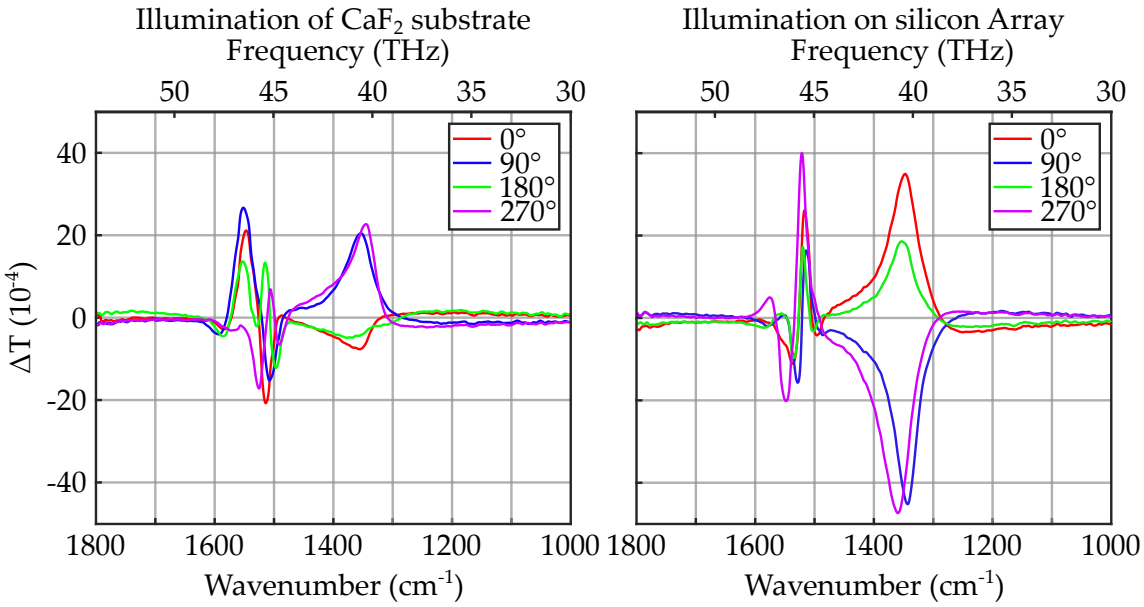

Figure 5.3: VCD artefact dependency on the sample rotation around the optical axis with a pitch of 4690 nm. The left and right panels depict the artefacts for the light hitting the substrate and silicon array first respectively, as shown in panel (a) of Figure 5.2. The insets denote the rotation angle of the sample around the optical axis in degrees.

on only one angle and look at how the artefact changes when switching the side that the sample is illuminated from. For the angle of 0°, we see that for a flip in the illumination side, there is coincidentally a flip in the sign of the artefact. This flipping of the sign is apparent to artefacts produced by linear birefringence (LB) and linear dichroism (LD) that arise from the anisotropy of the sample [130, 131]. As stated that the arrays are designed to be achiral, we can deduced that this anisotropy comes from the light not being at perfect normal incidence, as this will result in a non-isotropic interaction between the sample and the light.

While this LB and LD can be one of the reasoning for these artefacts occurring, it is not the full story. If it was pure LB and LD, then the sign and magnitude of the artefact should stay constant when rotating the sample around the optical axis, but here we see clear changes in magnitude and sign. We can relate this additional source of the artefacts due to non-normal incidence of the light onto the arrays, as even small deviations on the scale of less than a degree, can show large changes in the artefacts. We will look into how the artefacts vary with changing the angle of incidence, but we will firstly see how the artefacts seem through a different array with different parameters.

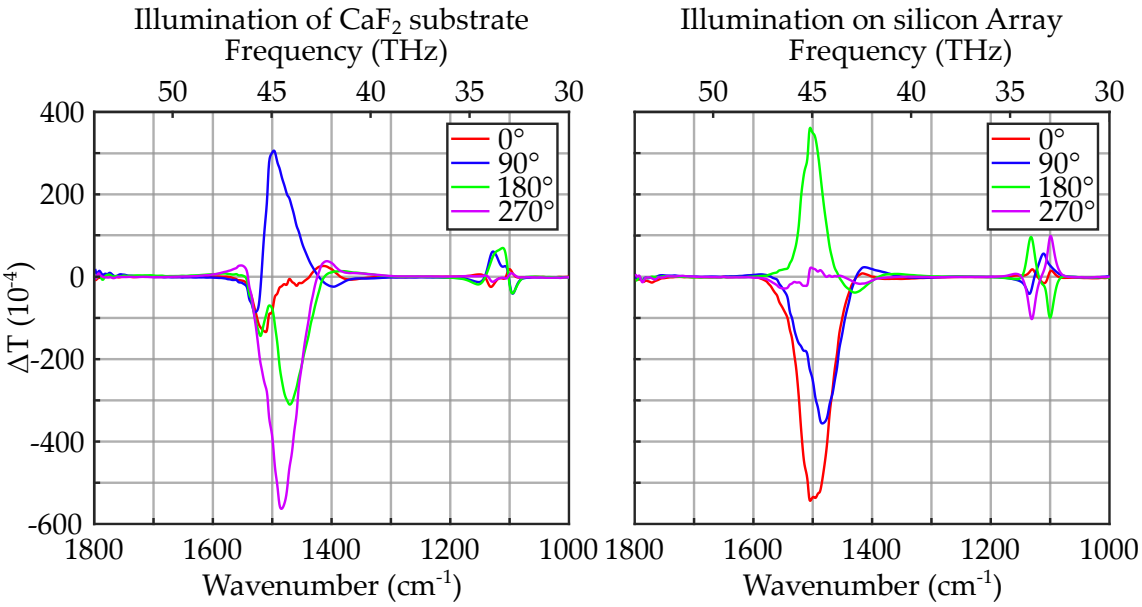

Figure 5.4: VCD artefact dependency on the sample rotation around the optical axis with a pitch of 6590 nm. The left and right panels depict the artefacts for the light hitting the substrate and silicon array first respectively, as shown in panel (a) of Figure 5.2. The insets denote the rotation angle of the sample around the optical axis in degrees.

Figure 5.4 shows the same spectra as the previous Figure, but for an array with the following parameters: radius $r = 2250$ nm, height $h = 1550$ nm, pitch $a = 6590$ nm, giving a centre-to-centre distance of 7609 nm. The first thing to notice, is that the spectral positions where the artefacts occur have changed. The reasoning due to the change in the spectra is due to the change of the pitch of the arrays. The increase in the pitch of the arrays causes the resonances to be shifted to lower frequencies, therefore we deduce that the spectral position of the artefacts is tied to the pitch of the arrays. Namely, the lattice resonances of the arrays that produce drops in the transmission spectra, or essentially absorbance peaks, lead to the VCD signals being produced.

In addition to these measurements, additional rotation angles were measured for the sample shown in Figure 5.3. These additional measurements showed that the artefact can also be minimised through choosing the rotation angle of the array. While this is the case, due to the artefacts dependence on the angle of incidence, this will need to be chosen on a case-to-case basis. Despite this, Figure 5.5 shows the additional measurements performed, which were only performed where the light hits the substrate first, as this is the same configuration as for the when the array is used to form the cavity. We find that we achieve a minimum for the

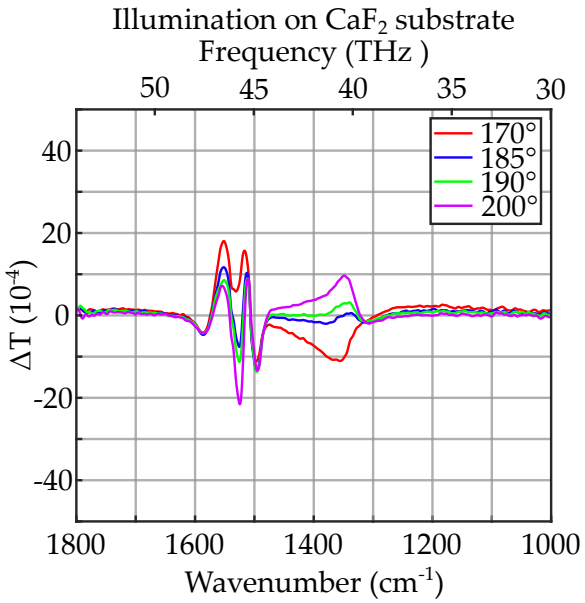

Figure 5.5: Further rotation angle measurements for the array sample with a pitch of 4690 nm. The additional rotation angles are shown in the inset in degrees. In the region from 1300 cm^{-1} to 1500 cm^{-1}, the magnitude of the artefact has been reduced by over an order of magnitude.

artefact at a rotation angle of 185°.

5.1.2 *Varying Angle of Incidence*

As previously stated, the artefacts arise from a combination of LB and LD and the angle of incidence of the light onto the array. Here we will show how the artefacts from the arrays are also dependent on the angle of incidence. To measure this, the array was mounted on a GM200 gimbal mirror mount (Thorlabs). This mount allows us to rotate the array around its central point in the vertical and horizontal axes, therefore keeping the position where the light hits the array the same. The sample holder setup for measuring the artefacts on the tip and tilt of the sample can be seen in Figure 5.2. Before starting the measurements, the array is aligned by eye such that the starting angle of incidence as as close to normal incidence as possible. To be clear, the 0° position is defined as the position assumed to be normal incidence. The measured artefacts from varying the angle of incidence are shown in Figure 5.6. The left panel is for rotating the sample in the horizontal axis and the right panel is for rotating the sample in the vertical axis. We clearly see that the variation of the angle of incidence in both axes has a large effect on the

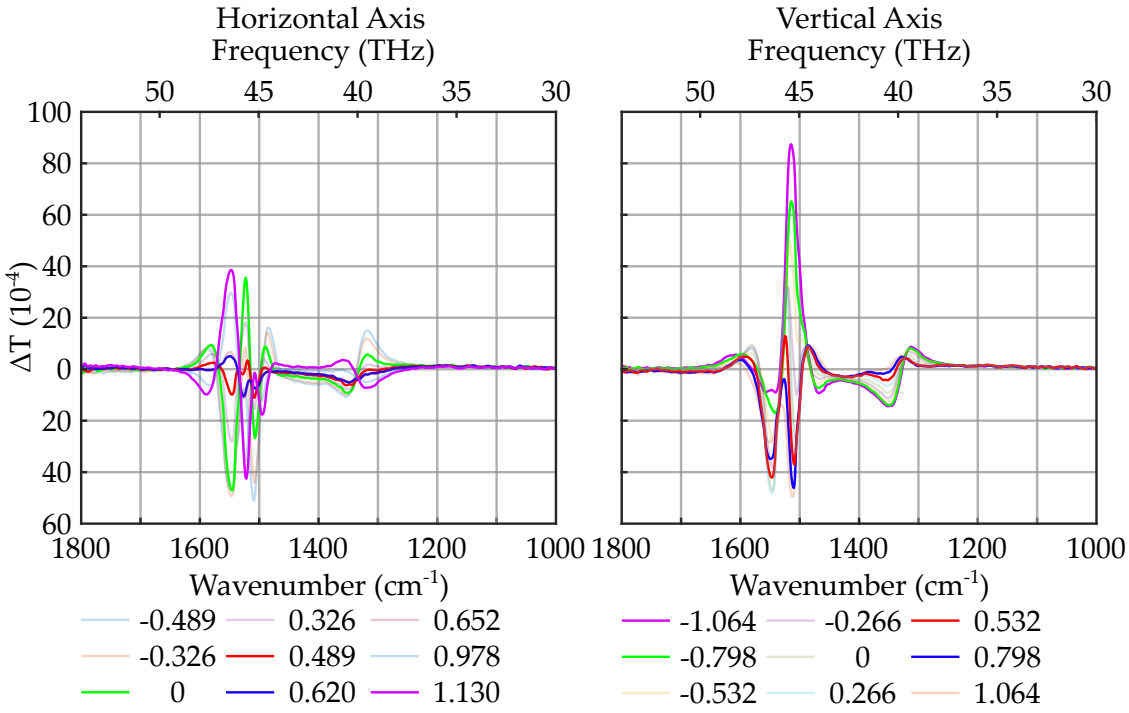

Figure 5.6: VCD artefact dependency on the angle of incidence of incoming light. The sample is mounted on the holder depicted in panel (b) of Figure 5.2. Tip corresponds to the vertical axis and tilt corresponds to the horizontal axis. The legend underneath the two plots depicts the deviation of the angle from what was deemed as 0°. The left and right panels show the variation of the VCD artefact for the horizontal and vertical axes respectively.

resultant artefact.

Although the artefacts produced by the diffracting arrays are unwanted, knowing why the artificial signals originate is beneficial in the analysis the VCD measurements to follow and are also to future works on the of structures for chiral sensing. The magnitude of these artefacts is on the scale of $10^{-3} - 10^{-2}$ and comparing this to the signal from the chiral molecules, it is apparent that these artefacts can be two orders of magnitude larger. This scale would cause any signal from the molecules to be completely drowned out and can become undetectable. Another potential source behind artefacts in the VCD spectrum due to the diffracting array can be from imperfections in the fabrication. The array structures were therefore inspected through the use of scanning electron microscopy and atomic force microscopy (AFM). The structures were of course fabricated to sufficient quality and the fabrication imperfections should not contribute to the artefacts due to their size in comparison to the cylinder structures themselves. We see from the fourier transform analysis on the AFM measurement of the diffracting array,

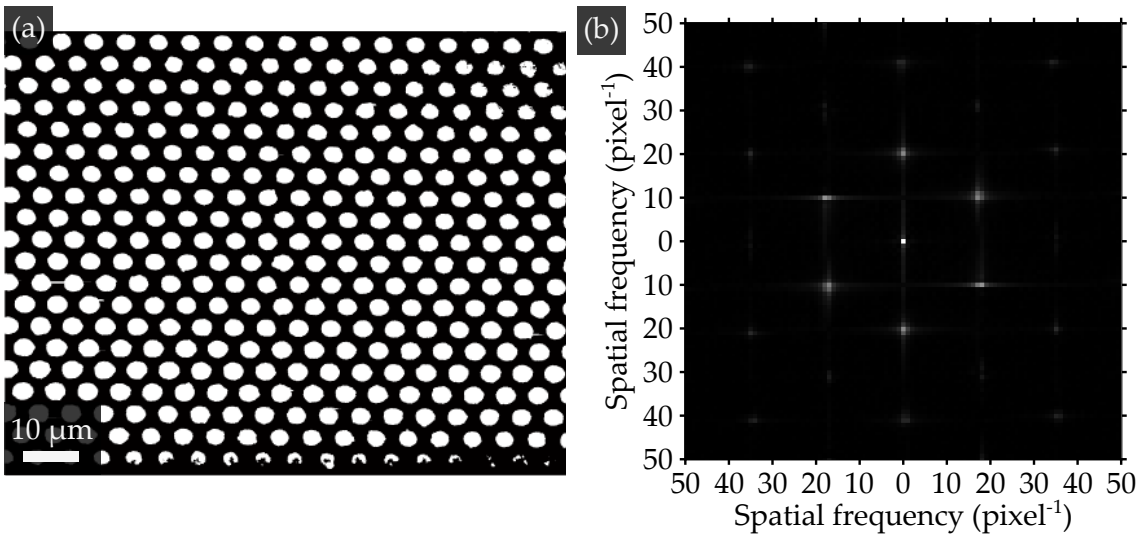

Figure 5.7: AFM micrograph of the fabricated diffracting array with corresponding fourier transformed image. (a) greyscale AFM micrograph recorded over a 94.4 µm × 94.4 µm area (2048 × 2048 pixels), resulting in a pixel size of 46.09 µm/pixel. The AFM measurement has has limits set so that the top part of the cylinders have a z value of 1 and the rest of the image has the z value set to 0. The edge effects on the tops of the cylinders arise from measurement artefacts from the AFM. (b) Fourier transform of the AFM micrograph. The six closest peaks to the central peak denote the average nearest neighbour distance over the array image. A value obtained for the 4697 ± 90 nm. The small variation between the different lattice directions shows high achirality in the array structures.

that the periodicity of the arrays are consistent in all lattice directions, therefore again showing good sample fabrication and also proving that this will not be a large contributing factor to the artefacts shown in section 5.1.

We now have an explanation for the origins of the artefacts produced by the diffracting arrays and have a possibility to minimise or possibly even negate them during measurements on chiral molecules using this diffracting array in an optical cavity, given the correct alignment tools. Unfortunately, for the following measurements on the chiral molecules, using the designed sample holder for the optical cavity did not allow for accurate rotation of the sample around the optical axis, nor to tip or tilt the cavity to bring the angle of incidence closer to normal, therefore minimising the artificial signals was not as good as it could of been. The artefact measurements were performed on the diffracting array when it is surrounded by ambient air, i.e. having a refractive index of 1. This is beneficial for the measurements on chiral molecules because when the array is placed within the cavity and a chiral solution fills the cavity, the medium surrounding the arrays now has a refractive index of approximately 1.43, which will in turn shift these

artefacts to lower wavenumbers, out of the region where we expect enhancements to occur. The measurements on chiral molecules will be discussed in the next section.

5.1.3 *Misalignment Between Cavity Mirrors*

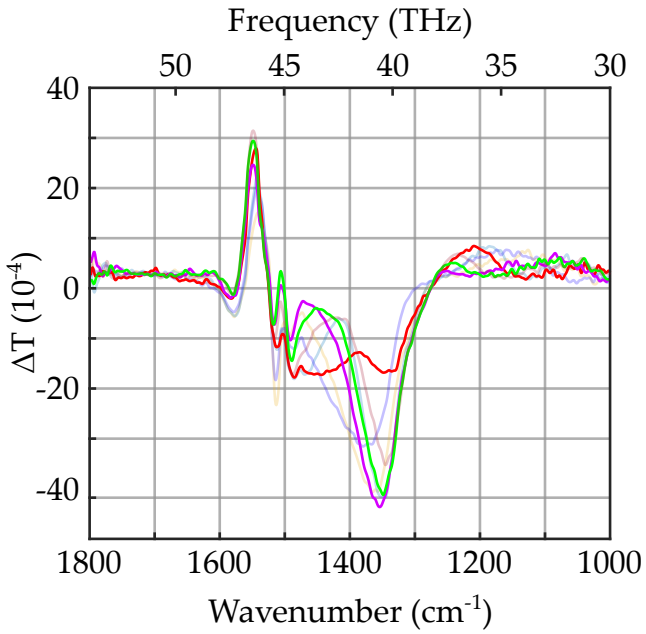

Figure 5.8: VCD artefacts from parallel mirror misalignment. The various curves are from measurements attempting to minimise the magnitude of the VCD artefact. The red curve shows the best achieved result for the minimisation of the artefact, indicating a high level of parallelism between the mirrors. The green and purple curves are the artefacts with the highest magnitude of the artefacts, indicating the worse degree of parallelism between the mirrors. The remaining curves, that are slightly transparent are included to show the full range of artefacts measured during the alignment process.

The previous two sources of the VCD artefacts originate from the diffracting arrays themselves when the angle of incidence is offset from normal incidence. However, when the entire cavity is assembled, there is yet another source for artefacts to occur. This new source of artefact emerges from the misalignment between the two cavity mirrors. Not to be mistaken with the misalignment between the mirrors as explained in section 3.2, this misalignment is from when the two cavity mirrors are not parallel. When the two mirrors are non parallel, there is a broken spatial symmetry within the cavity system and this induces the observed artefacts presented in Figure 5.8. Here we show several different VCD measurements that

were recorded when adjusting the one of the two cavity mirrors to both check the cavity length and attempt to align the cavity such that the two mirrors are parallel. When this alignment procedure is performed, the cavity is only filled with air to prevent any miscalculations in determining the cavity length due to not being completely certain about the refractive index of the solvent at these operating frequencies. Unfortunately, due to the apparatus used in the measurement, it is not possible to know the exact angle between the two mirrors when adjusting the two mirrors, but the Fabry-Pérot interference fringes in the transmission spectrum can be used to ensure sufficient parallel alignment between the two mirrors. What can be taken from these measurements is that it is possible to align the mirrors to be sufficiently parallel that the magnitude of the artefact can be reduced by more than 2-fold when observing the artefact around the $1400\,\mathrm{cm}^{-1}$ wavenumber.

In conclusion to this section, I have shown the artefacts that are produced by the diffracting arrays and shown why the artefacts emerge. The measurements performed showed how the artefacts varied when changing the illumination direction and rotation of the array around the optical axis. Further more, I have shown how artefacts are also related to the non-parallelism between the two cavity mirrors and how the alignment of the mirrors is crucial for both the cavity resonances as well as reducing the VCD artefacts. In the following section, I present the experiments performed on several concentrations of the BINOL molecules within the enhancing cavity and discuss the results acquired.

5.2 Cavity Enhanced Circular Dichroism of BINOL Molecules

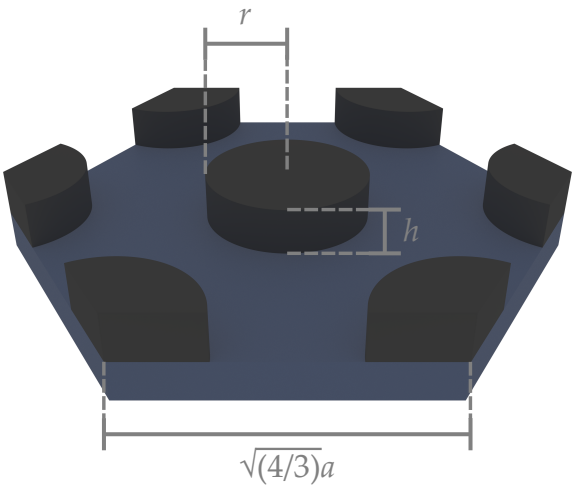

Figure 5.9: Rendered illustration of the unit cell of the diffracting array. The geometrical parameters of the diffracting array are $r = 1562\,\text{nm}$, $h = 1080\,\text{nm}$, $a = 4690\,\text{nm}$.

Now I will report the spectroscopic performance of the CD enhancing cavity, whose principle of operation was explained in section 3.2. The measurement procedure for procuring the following data is described in section 4.4.3 using an FTIR-based VCD spectrometer. The array structures have been tailored such that cavity resonances can be matched to the circular dichroism resonance of the chosen chiral molecule. For this work, we have chosen the molecule to measure as BINOL, due to it's availability, many resonances within the infrared spectrum and the controllability of the concentration in the solvent. Although, there are plenty of other molecules that could of been chosen to investigate such as Limonene or α-pinene. The parameters of the diffracting array used as one of the mirrors are the same as described in the previous section and as described in Figure 5.9. With these array parameters, we are able to vary the cavity length to match the BINOL resonance at $1505\,\text{cm}^{-1}$. The total footprint of the diffracting array is $16\,\text{mm} \times 16\,\text{mm}$, ensuring that none of the light is able to escape out of the sides of the cavity.

The two cavity mirrors are assembled in the microfluidic chamber introduced in section 4.3. The three piezoelectric actuator screws are manually aligned to bring the two mirrors close together and seal the microfluidic chamber section by applying a force to the chemically resistant O-ring. The three screws are again adjusted individually until Fabry-Pérot interference fringes appear in the transmission spectrum and a sufficient cavity length is reached. The presence of the Fabry-Pérot interference fringes provide the information needed to ensure

that the two mirrors are aligned to be sufficiently parallel. These interference fringes are then again used to determine the manually reached cavity length. A voltage is then applied to the piezoelectric elements to then accurately adjust the cavity length to the desired value. Once this cavity length is reached, the cavity is prepared for measurements on the chiral solutions.

Now we can continue with the examination of the experimental circular dichroism spectra that were obtained for five different concentrations of BINOL molecules dissolved in deuterated chloroform ($CDCL_3$) in the optical cavity. The concentrations measured are as follows from the highest to the lowest: 49 mg/mL, 10 mg/mL, 5 mg/mL, 1.5 mg/mL, and finally 0.3 mg/mL. The solutions of chiral molecules were mixed as detailed in section 4.4.1, and the corresponding CD spectra was obtained as described in 4.4.3. The entire wavenumber range that was recorded during the measurements was from 800 cm^{-1} to 1800 cm^{-1}. Wavenumbers below 1000 cm^{-1} are disregard as optics used in the spectrometer are opaque. For the following measurements, unlike the artefact investigation in the previous section, the data is cut to a region of interest between 1450 cm^{-1} and 1550 cm^{-1} as this is where the resonances are expected. Recalling the artefact investigation in the previous section, one might remember that the artefacts spanned from 1300 cm^{-1} to 1600 cm^{-1}, directly covering the region where the enhancements should lie. Fortunately, with the introduction of the chiral solutions into the cavity, this shifts these resonances to lower wavenumbers due to the change in refractive index within the cavity, removing them from this region of interest.

We now take a look at the recorded spectra of the BINOL molecules in the enhancing cavities. For comparison, the same concentrations of molecules were also recorded in a cavity of the same path length, but without the diffracting array present; therefore, no resonant modes will occur. We can now compare the spectra between the plain cavity and the enhancing cavity. What we denote as the plain cavity is the optical cavity formed by a bare calcium fluoride substrate and a bare silicon substrate to form the cavity. The enhancing cavity is described as the cavity that is formed by the diffracting array on a calcium fluoride substrate and the silicon substrate. We first look at the spectra presented in Figure 5.10, where the cavity length is set to 17 µm. The left-hand plot shows the recorded spectra for both (R)-BINOL (blue) and (S)-BINOL (red) in the cavity without the diffracting arrays, and the right-hand plot shows the same spectra but with the diffracting arrays present. What is expected from this concentration of molecules is that there is essentially no enhancement as described in Section 3.4. The narrow vertical grey box serves to guide the eye to the spectral region where the enhancement is expected. This is backed up by the fact that we now see peaks at the wavenumbers where we expect them. Although some signal is seen in the plot with the arrays, we can attribute this to the spectra of the BINOL molecules where no enhancing

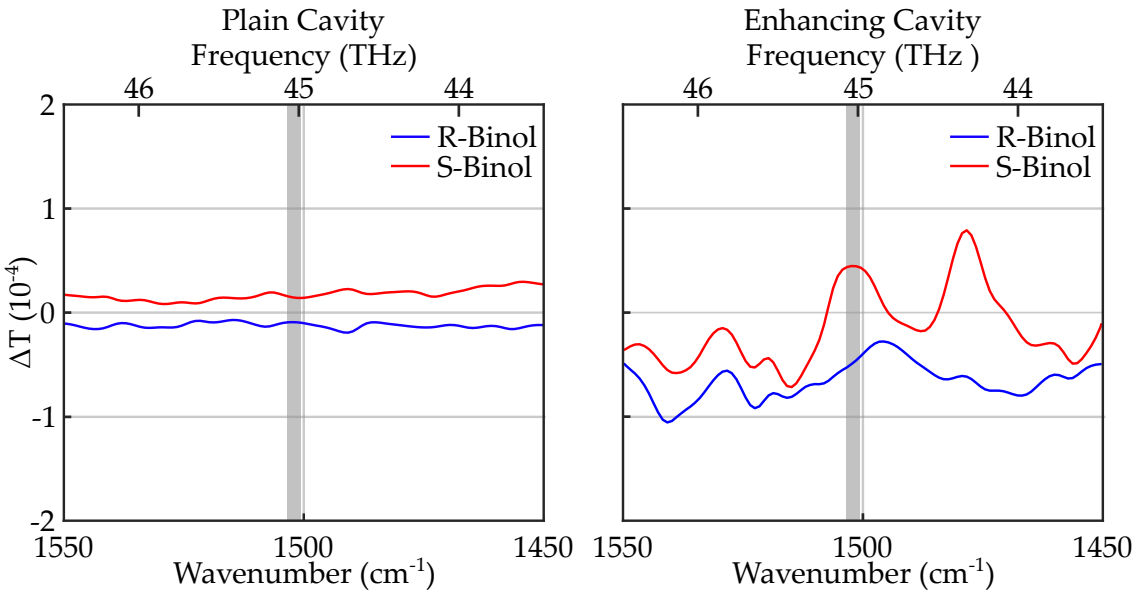

Figure 5.10: Experimental circular dichroism measurement for a concentration of 49 mg/mL. The left panel depicts the data recorded for the concentration of molecules in a plain cavity at a path length of 17 µm. The right panel shows the data recorded for the same concentration of molecules at the same path length but in the cavity with the diffracting array as one mirror. The thick grey line serves to guide the eye to where the enhancing peak is expected.

effect is expected.

Let us now look at the data shown in Figure 5.11. The left plot shows the data recorded for both enantiomers of the BINOL molecules in a plain cavity at a concentration of 10 mg/mL. The right plot shows the data recorded in the enhancing cavity. As expected, in the plain cavity at this concentration and a path lent of 17 µm we don't see any distinctive features from the BINOL molecules. For the enhancing cavity however, a peak centred around 1504 cm^{-1} is present. Let us discuss the features that point towards this feature originating from the resonant modes of the enhancing cavity. Firstly, with the chosen array parameters and the set cavity length, we expect the resonance to occur at a wavenumber of approximately 1504 cm^{-1}, which is what is seen here. Additionally, the first diffraction order, which is the chosen order that couples the light into the resonant waveguide mode for the circular dichroism enhancement, now has a flip of the helicity compared to the input light. While this is unexpected as the intended design of the diffracting arrays is to preserve the helicity of the light, it does not seen to prove to be an issue as in the experimental data, we in fact see a flip in the sign where the resonance is expected. Before continuing, I must define what is meant by a flip in the sign here. In the right panel, at the spectral region indicated

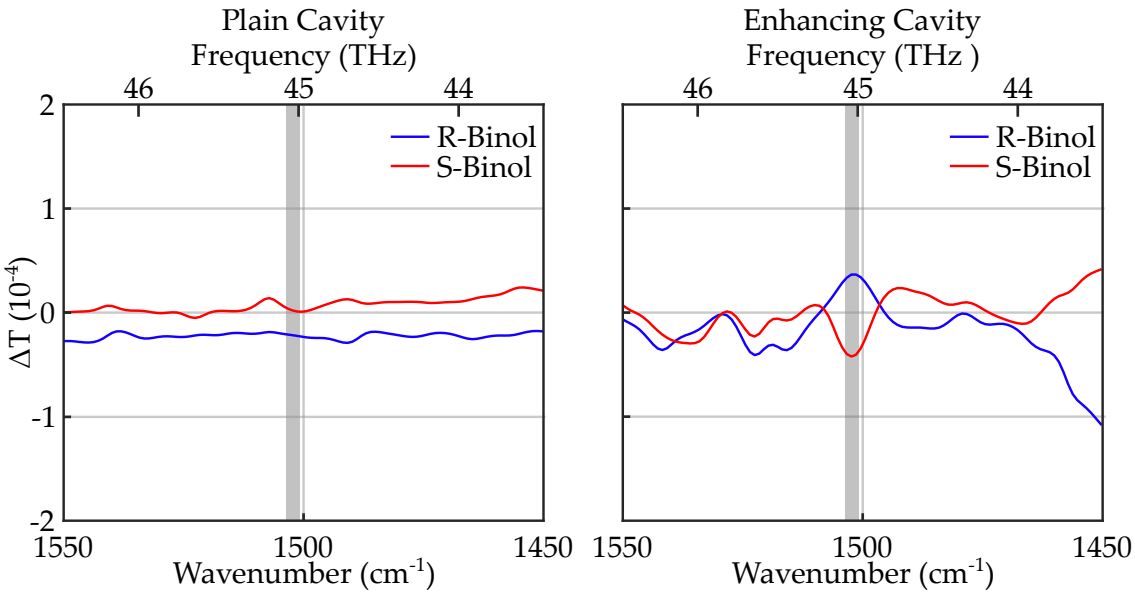

Figure 5.11: Experimental circular dichroism measurement for a concentration of 10 mg/mL. The left panel depicts the data recorded for the concentration of molecules in the plain cavity at a path length of 17 µm. The right panel shows the data recorded for the same concentration of molecules at the same path length but in the cavity with the diffracting array as one mirror. The thick grey line serves to guide the eye to where the enhancing peak is expected.

by the narrow vertical grey box, we see the (R)-BINOL has a signal with positive sign, and the (S)-BINOL has a signal with negative sign. When the same BINOL enantiomers are measured in a cuvette, the CD signal for the (R)-BINOL will have a negative sign, and (S)-BINOL will have a positive sign at the resonance that we have chosen to tailor the cavity for.

The next concentration measurement that we can look at is for 5 mg/mL, shown in Figure 5.12. Again, for the plain cavity measurement, nothing is seen apart from what is deemed to be the inherent noise from the measurement system. In the data recorded for the enhancing cavity, we again observe the resonances centred at 1504 cm^{-1} with a flip in the sign. This shows a consistent trend between this concentration and the previous concentration, where enhancement is expected. As we can also see here that the resonant peak is not a distinct, independent peak but is also slightly broadened. This is seen especially for the (R)-BINOL data in Figure 5.12. A broader peak in the experiment is expected and could be attributed to the beam not being perfectly collimated or a small misalignment within the cavity mirrors. Returning again to the effect of the concentration dependence on the enhancement capabilities of the cavity, for a lower concentration, the enhancement

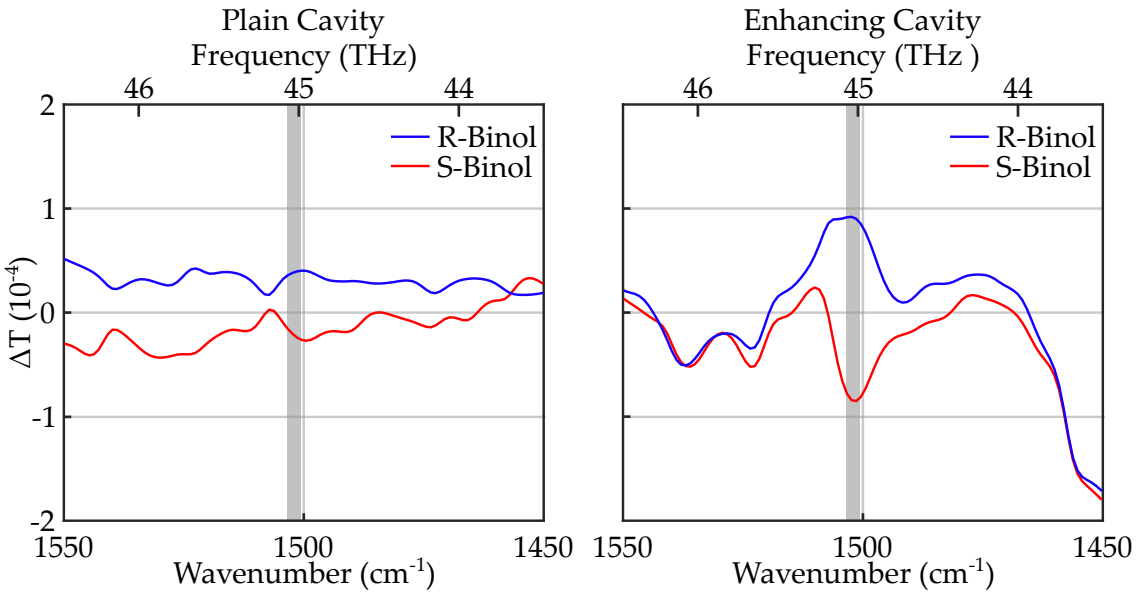

Figure 5.12: Experimental circular dichroism measurement for a concentration of 5 mg/mL. The left panel depicts the data recorded for the concentration of molecules in a plain cavity at a path length of 17 µm. The right panel shows the data recorded for the same concentration of molecules at the same path length but in the cavity with the diffracting array as one mirror. The thick grey line serves to guide the eye to where the enhancing peak is expected.

factor should increase. Between the 10 mg/mL and 5 mg/mL concentrations spectra in the enhancing cavity, there is a noticeable change in the magnitude of the resonant peaks, indicating this increased enhancement factor for the lower concentration.

Finally, let us draw our attention to the final two measurements in Figures 5.13 and 5.14. The same measurements were performed for the final two concentrations of 1.5 mg/mL and 0.3 mg/mL in both the plain cavity and the enhancing cavity. As expected, in the plain cavity measurements, there are no distinguishable features seen. And for the enhancing cavity, we clearly see the resonance peaks. Reiterating what has been stated for the previous plots, we again see in both these cases the sign flip of the CD signal at the resonance and the resonance being centred around 1504 cm^{-1}, with yet another increase in the signal magnitude over the previous concentrations.

In summary, we have shown here the experimental results on circular dichroism measurements on several concentrations of BINOL molecules in a cavity designed to enhance the signal. With a comparison measurement of the same molecules in a cavity without the diffracting array, it is clearly visible the peak that forms in

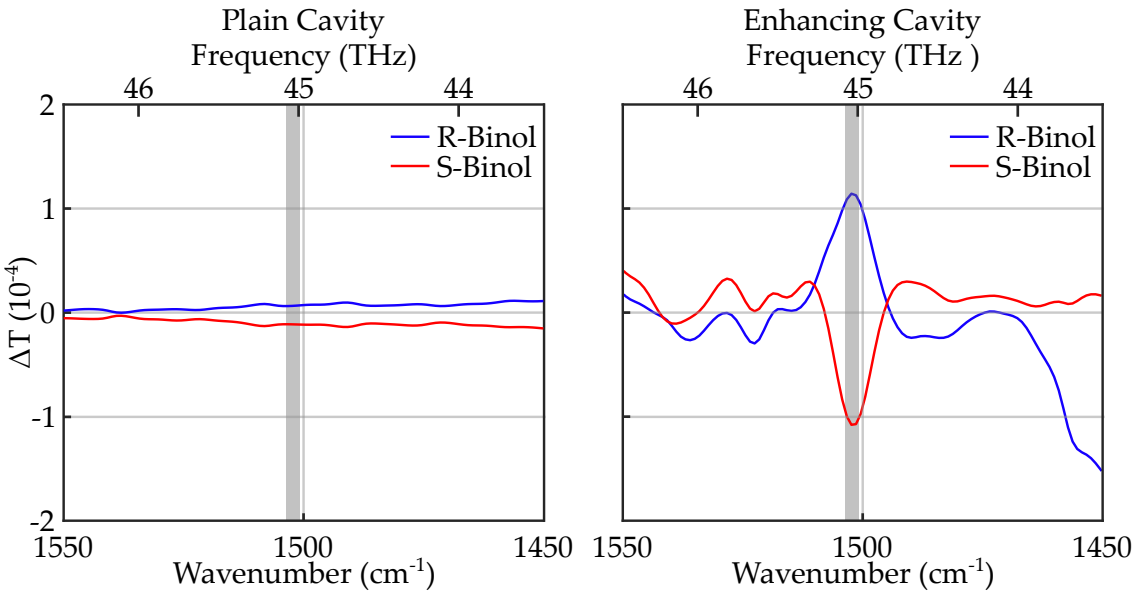

Figure 5.13: Experimental circular dichroism measurement for a concentration of 1.5 mg/mL. The left panel depicts the data recorded for the concentration of molecules in a plain cavity at a path length of 17 µm. The right panel shows the data recorded for the same concentration of molecules at the same path length but in the cavity with the diffracting array as one mirror. The thick grey line serves to guide the eye to where the enhancing peak is expected.

the resonant cavity, indicating that these resonant modes are taking effect. The dependency of the enhanced signal on the concentration of the chiral molecules in the solution that was explained in section 3.4 was also shown to be present in the experiment, showing a qualitative agreement with the theoretical predictions.

In the following section, the experimental results presented here will be summarised and discussed. The advantages and limitations of this method for circular dichroism enhancement are identified.

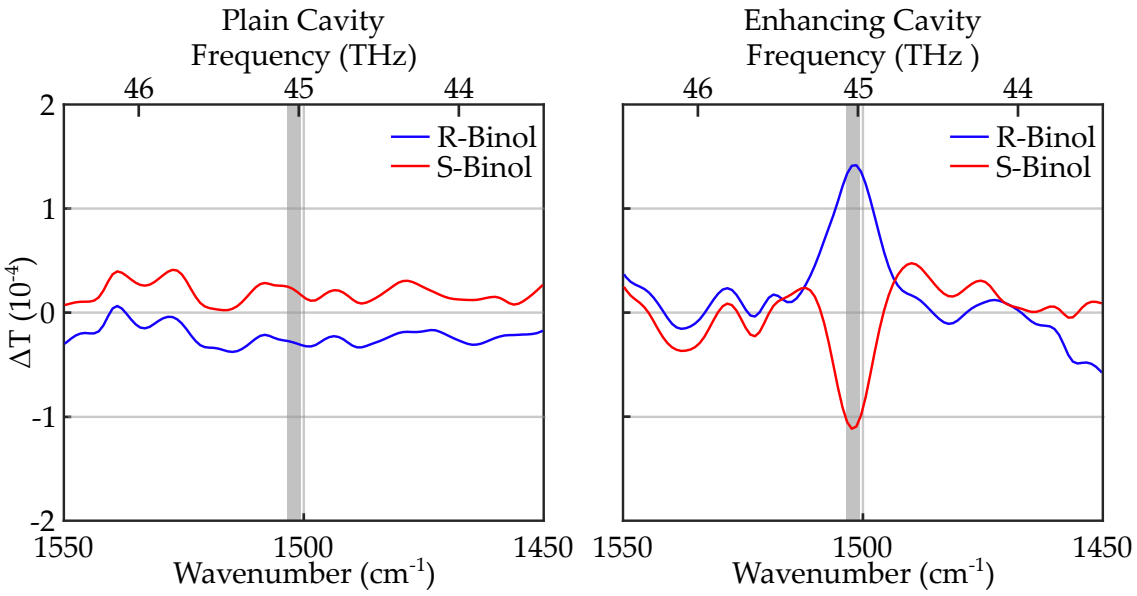

Figure 5.14: Experimental circular dichroism measurement for a concentration of 0.3 mg/mL. The left panel depicts the data recorded for the concentration of molecules in a plain cavity at a path length of 17 µm. The right panel shows the data recorded for the same concentration of molecules at the same path length but in the cavity with the diffracting array as one mirror. The thick grey line serves to guide the eye to where the enhancing peak is expected.

5.3 Discussion

Within this chapter, I have characterised the structures that are placed into an optical cavity designed for the enhancement of circular dichroism signals. Furthermore, I have presented experimental measurements to test the circular dichroism enhancement capabilities of the metasurface based cavity, despite the multitude of experimental challenges that were encountered.

Prior to the measurements on the chiral molecules, the structures used for the exact task of enhancing the circular dichroism signal must be thoroughly understood. To accomplish this, the samples were placed within the sample compartment of the FTIR CD spectrometer. Using various holders to rotate the array sample around the optical axis, as well as in the horizontal and vertical axes to change the angle of incidence of the light on the sample, the CD artefacts that originated from the diffracting array can be understood. The results from these measurements showed the extent of the artefacts produced by the silicon cylinder arrays and presented logical arguments for their origins. It can be deduced that a source of the artefacts is from a combination of the lattice resonance of the array combined with non-normal incidence of the light which induces linear birefringence and linear dichroism effects due to the anisotropy, effectively making the array structure

chiral [132]. The fourier transform analysis of the fabricated arrays, and as well as simply inspecting the sample with a SEM, and the variation of the angle of incidence proved that the anisotropy of the sample arose from the tilt and it was not inherent to the sample itself, again showing good sample fabrication. Yet another source of artificial signals was shown to be resultant from a non-parallel misalignment of the two cavity mirrors, while an exact measurement of the tilt between the two mirrors was not possible due to the equipment at hand, a qualitative result showed that the artefact can be reduced through improved parallel alignment of the cavity mirrors.

To measure the enhancing performance of the metasurface based cavity, the cavity length was tuned to the desired length, and the mirrors were aligned to achieve the lowest magnitude of tilting between them as possible. The measurements that followed were on five separate concentrations of each enantiomer of the BINOL molecules dissolved in a deuterated chloroform solvent. The solutions of the chiral molecules were measured in both the enhancing cavity as well as a plain cavity with the same path length, in order to have a reliable comparison under identical experimental conditions.

The results of the conducted experiments on the solutions of chiral molecules showed a distinct difference between when they were measured in the plain cavity and the enhanced cavity. Throughout every concentration for the plain cavity, no clear signs of vibrational optical activity was seen. However, in the enhanced cavity, a resonant peak is seen for all concentrations except from the largest as expected. The consistent signs of the peaks in the enhanced cavity, along with the trend relating to the concentration of the molecules in the solvent showed convincing trends that and effect was observed when no signal was present.

Although, it must be said that these results serve as a proof of concept for this avenue towards the goal of enhancing the circular dichroism signal of chiral molecules in solution. A rigorous method that could undeniably prove the experimental feasibility of this method would require much more experimentation. One possible route to show a more convincing argument is showing the response of the enhancing cavity when filled with the chiral solution over a range of cavity lengths. However, CD measurements are incredibly time consuming and for measuring only five concentrations at a singular cavity length took approximately 10 hours of collective measurement time to collect the data. To collect a complete dataset for a range of cavity lengths, it would take at least two weeks of constant measuring, including the time needed for adjusting the cavity length and exchanging the solutions.

Improving the performance of the enhancing cavity could be achieved through approaches. An obvious direction would be improving the fabrication methods, such as opting for electron beam lithography, as the resolution is much finer

compared to optical lithography, but the process time would be greatly increased [133, 134]. Other possible avenues could be an optimisation of the current process with more informed choices of the photoresist and developer, as there do exist photoresist that are applicable for smaller structures, although they need to still be suitable for the etching processes employed. Aside from the aspects in the fabrication side, improvements to the sample holder could be made to provide even further alignment processes that would allow use to perform the adjustments to the entire cavity to reduce the artefacts seen, which with the current holder is not currently possible.

In summary, this chapter presented the experimentation on a metasurface-based optical microcavity, which was developed in accordance to the methods described in chapter 4. The fabricated structures that were employed to undertake this task were characterised within the circular dichroism spectrometer. Several concentrations of BINOL molecules in solvent were measured within the cavity, and the obtained results were presented.

6 Chapter 6
Conclusions and Outlook

Within this thesis, I have presented the design and fabrication of a metasurface microcavity for the enhanced sensing of chiral molecules in solution. I have detailed the principle of operation behind the cavity as well as the theoretical predictions for the performance of the cavity. The artificial signals produced from the diffracting array were characterised and understood, providing future works to minimise or even prevent these in future experiments. I demonstrated the effect of the enhancing cavity on BINOL molecules. In the following, I will summarise and put into context the contents of this work and discuss the paths forward for chiral sensing using optical cavities.

The theoretical principles behind the operation of these metasurface cavities was explained in chapter 3. I discuss previously presented structures and methods for circular dichroism enhancement and explain the drawbacks of these methods and show why a route towards optical cavities has many benefits. Here, I have covered the underlying principles of operation of the cavity designs and shown why conventional cavities are not suitable for such tasks. Within, I have discussed the experimental feasibility of the double-array cavity configuration and shown why the single-array cavity was opted for in the experimental fabrication. I then showed the limitations of the initially used calculations, which did not include any realistic resonance of the chiral molecules, which is key to accurately predicting a system to enhance the response of such molecules. This chapter was brought to an end by showing the effect of the real response of a chiral molecule has on the performance of the optical cavities.

In chapter 4, I described the methods that were developed and employed for the fabrication of the silicon cylinder arrays. Firstly, I detailed the process that was developed for the deposition of the silicon thin films onto the calcium fluoride substrate. This proved not to be such a straightforward process due to the properties of both the substrate and the silicon film, thus requiring delicate substrate preparation and additional process steps to ensure sufficient film quality and adhesion. The next section of the chapter discussed the methods used for the

fabrication of the silicon disk arrays. This covered the topics of optical lithography, dry etching and resist stripping. In the third section, I introduced the custom designed microfluidic chamber that was designed to hold the two mirrors for the microcavity. Within the microfluidic chamber, I designed various alignment tools with sub-micrometer precision that were vital for the function of the cavity. I also described the microfluidic system that was used for flowing solutions of chiral molecules into the chamber for measurement. The chapter was closed with a description of the FTIR CD spectrometer used for the experiments and the measurement workflow.

The experimental measurements and results were presented in chapter 5. First, I showed the characterisation measurements of the artificial signals that can arise from various misalignments in the system such as non-normal incident light and a tilt between the cavity mirrors. Solutions to reduce and potentially remove these artifacts that can lead to better measurements were additionally discussed. Thereafter, I presented the experimental results achieved for the measurement of BINOL molecules in the metasurface cavity. The cavity showed a clear signal when compared to the same measurement but in a plain cavity. This cavity design is, to my knowledge, the only experimental investigation of such a route for the enhanced sensing of chiral molecules in a solution, providing an interaction between the light and the molecules over a large volume. Where as many proposed methods in literature are only effective in small volumes near the structure [28, 31, 64]. To display the effect of the concentration of the chiral molecules on the enhancing capabilities of this cavity, I have exhibited this effect in the experimental results by measuring fave different concentrations of the chiral molecules. The effect in the data matches the trend that the theory predicts. In the final section, I have discussed the results.

Outlook

This thesis serves as a significant step towards improved routine sensing of chiral molecules using optical cavities to improve the signal, there is still further work that needs to be done to bring this to the point where it could be used in pharmaceutical laboratories. More than 50% of current drugs in use today are chiral [135] and current devices require large volumes of analyte to obtain a reliable signal due to the inherently weak chiroptical signals [136], this brings a great desire to have a robust system that can provide a greater response of the molecules while keeping the volume constant. There are plentiful approaches for enhancing circular dichroism in the solid, gas and liquid states. Although, the method reported in this work is the first of its kind to my knowledge at this time of writing this dissertation. A resonant system, that does not alter the helicity of the light and be able to probe a solution that is small in volume would be greatly beneficial.

There are several routes that could be taken for the improvement of this type of optical cavity. A relatively straightforward direction would be improving the measurement method, namely, the implementation of such aspects of the sample holder that provide the means to minimise or even remove artefacts that cloud the CD structure of the molecules. Although, the degree of accuracy required for this tuning would need to be rather high, but there indeed exists such equipment that could make this possible.

In terms of the fabrication and design improvements, while the fabrication of these structures was performed to a high degree, there is always room for improvement. For example, a complete fabrication process carried out within a cleanroom environment would prove beneficial, as aberrations from dirt and particles caused many unwanted defects in the structures. Further work could also be spent on some fabrication steps, such as the photoresist choice. While suitable for the expose and etching processes used in this work, there were difficulties encountered. Such as due to the substrate used, removal of this resist after dry etching became a difficult and tedious task as the photoresist needed to be removed without causing damage to the substrate or fabricated structures. The microfluidic chamber, while already having incorporated the required alignment requirements needed for the function of the cavity, also has potential for improvement and coming a long way from the initial idea of a PDMS based cavity, could still be improved. An improved method to determine the cavity length would go a long way. Determining the calibration curves of the piezoelectric actuators was used via an optical coherence tomography (OCT) setup, and having such a system implemented to determine the cavity length in-situ would be highly beneficial for cavity length measurements. Although, such a system would require this to be home built and is far from the

scope of this work.

For optical cavities that are specifically designed for transmission or reflection of only one handedness, these avenues could open up new possibilities of improved chiral sensing [137–139]. Due to the strong resonances of light within optical cavities, I see the potential for various routes towards enhanced chiral sensing.

Recalling to the cavity designs that were presented in this work, there are potentials for further work. Firstly, the height and radius of the silicon cylinders can be further optimised for yet better efficiency into the diffraction orders and improved helicity preservation [64, 140, 141]. With a successful experimentation on the single-array cavity, then an attempt on the more difficult to fabricate double-array cavity could be made as this configuration offers better mode confinement with improved helicity pureness when aligned properly. Ontop of this, the diffracting arrays can be tailored to produce a response at almost any frequency that is desired, with limitations only being from the fabrication processes [142, 143].

While systems that are designed specifically to enhance the CD of a molecule do not by default also enhance the OR, even though the two are related. Fortunately for the system reported here, it can also enhance the OR as reported in [66]. An experimental realisation of the OR enhancing properties of these types of optical cavities could also be an interesting step forward, and could have some benefits such as OR being a non-resonant method to measure the handedness of a molecule. This means that the region of interest can be where no absorption occurs and OR can be studied over a broad wavelength range rather than having to tune parameters to specifically match a CD resonance. These two points also point towards an ease in measurement for opting to enhance the OR of a molecule.

For the final thoughts with potential future improvements to this work, I point out a downside to this approach for enhancing the CD signal, which is the narrow region of enhancement, which is also apparent for many resonant dielectric structures [33, 38]. A possible solution to enhance the circular dichroism response of chiral molecules over a broad wavelength range was proposed by Nyman et al. [100]. The proposed solution is an array of these enhancing cavities, all tailored to enhance a specific wavelength and combined provide an enhancement over a large wavelength range. Although, the experimental realisation of such a device would be a colossal task, and would require high quality fabrication of many arrays with different parameters, both with a suitably sized footprint so that light cannot escape the cavities and also not to have each resonance overlap with resonances of other cavities as this would produce artefacts in the measurement. A method to independently measure the signal from each spectrometer would need to be implemented, which could lead to problems with reaching sufficient signal strengths. Therefore, the experimental feasibility of this may be out of reach, but if possible could be immensely powerful in the future of CD spectroscopy.

I close this discussion with a reiteration of the goals that have been achieved in this thesis. A novel metasurface optical cavity was fabricated and put to the task of enhancing the CD signal of chiral molecules in solution with the use of a custom designed microfluidic chamber. While due to artificial signals produced by misalignment and the inherent difficulties that come with CD spectroscopy, I believe that with these preliminary results, it serves as a step in the direction towards the goal of a commercial CD spectrometer that can be used for easier detection of the handedness of chiral molecules in pharmacology, toxicology, chemistry and biology.

Bibliography

[1] T. Kelvin, "The second Robert Boyle lecture", J. Oxf. Univ. Jr. Sci. Club **18**, 25 (1894) (cited on page 5).

[2] L. L. Whyte, "Chirality", Nature **180**, 513–513 (1957) (cited on page 5).

[3] L. L. Whyte, "Chirality", Nature **182**, 198–198 (1958) (cited on page 5).

[4] S. Capozziello and A. Lattanzi, "Spiral galaxies as enantiomers: Chirality, an underlying feature in chemistry and astrophysics", Chirality: The Pharmacological, Biological, and Chemical Consequences of Molecular Asymmetry **18**, 17–23 (2006) (cited on page 5).

[5] M. Schilthuizen and A. Davison, "The convoluted evolution of snail chirality", Naturwissenschaften **92**, 504–515 (2005) (cited on page 5).

[6] S. Kleinlogel and A. G. White, "The secret world of shrimps: polarisation vision at its best", PLoS One **3**, e2190 (2008) (cited on page 5).

[7] T.-H. Chiou, S. Kleinlogel, T. Cronin, R. Caldwell, B. Loeffler, A. Siddiqi, A. Goldizen, and J. Marshall, "Circular polarization vision in a stomatopod crustacean", Current Biology **18**, 429–434 (2008) (cited on page 5).

[8] J.-S. Wang, G. Wang, X.-Q. Feng, T. Kitamura, Y.-L. Kang, S.-W. Yu, and Q.-H. Qin, "Hierarchical chirality transfer in the growth of Towel Gourd tendrils", Scientific reports **3**, 3102 (2013) (cited on page 5).

[9] U. Meierhenrich et al., *Amino acids and the asymmetry of life: caught in the act of formation* (Springer, 2008) (cited on page 5).

[10] M. Quack, "How important is parity violation for molecular and biomolecular chirality?", Angewandte Chemie International Edition **41**, 4618–4630 (2002) (cited on page 5).

[11] M. G. Weller, "The mystery of homochirality on earth", Life **14**, 341 (2024) (cited on page 5).

[12] D. G. Blackmond, "The origin of biological homochirality", cold spring harbor perspectives in biology **11**, a032540 (2019) (cited on page 5).

[13] I. de France., *Mémoires de l'Institut des Sciences et Arts Sciences math. et phys*, Vol. T.1(1798), https://www.biodiversitylibrary.org/bibliography/16282 (Paris, 1795), p. 720 (cited on page 6).

[14] B. Kahr, "Polarization in France", Chirality **30**, 351–368 (2018) (cited on page 6).

[15] J. Lequeux, *François Arago: A 19th Century French Humanist and Pioneer in Astrophysics*, Vol. 421 (Springer, 2015) (cited on page 6).

[16] J.-B. Biot, *Sur un nouveau genre d'oscillation que les molécules de la lumière éprouvent en traversant certains cristaux:...* (1812) (cited on page 6).
[17] T. M. Lowry, *Optical rotatory power* (Dover publications, 1964) (cited on page 6).
[18] R. S. Cahn, C. Ingold, and V. Prelog, "Specification of molecular chirality", Angewandte Chemie International Edition in English **5**, 385–415 (1966) (cited on page 6).
[19] I. Ali, H. Y. Aboul-Enein, M. M. Sanagi, and W. A. W. Ibrahim, "Chirality and its role in environmental toxicology", Molecular, Clinical and Environmental Toxicology: Volume 3: Environmental Toxicology, 413–436 (2012) (cited on page 6).
[20] Y. Zhou, S. Wu, H. Zhou, H. Huang, J. Zhao, Y. Deng, H. Wang, Y. Yang, J. Yang, and L. Luo, "Chiral pharmaceuticals: environment sources, potential human health impacts, remediation technologies and future perspective", Environment international **121**, 523–537 (2018) (cited on page 6).
[21] B. Knoche and G. Blaschke, "Investigations on the in vitro racemization of thalidomide by high-performance liquid chromatography", Journal of Chromatography A **666**, 235–240 (1994) (cited on page 7).
[22] M. Laska and P. Teubner, "Olfactory discrimination ability of human subjects for ten pairs of enantiomers", Chemical senses **24**, 161–170 (1999) (cited on page 7).
[23] A. Fresnel, *Extrait d'un" Mémoire sur la double réfraction particulière que présente le cristal de roche dans la direction de son axe"* (éditeur non identifié, 1822) (cited on page 7).
[24] A. FRESNEL, *Mémoire sur la loi des modifications que la réflexion imprime à la lumière polarisée (memoir on the law of the modifications that reflection impresses on polarized light)*, 1823 (cited on page 7).
[25] T. Müller, K. B. Wiberg, and P. H. Vaccaro, "Cavity Ring-Down Polarimetry (CRDP): A New Scheme for Probing Circular Birefringence and Circular Dichroism in the Gas Phase", The Journal of Physical Chemistry A **104**, 5959–5968 (2000) (cited on pages 7, 36).
[26] T. Müller, K. B. Wiberg, P. H. Vaccaro, J. R. Cheeseman, and M. J. Frisch, "Cavity ring-down polarimetry (CRDP): theoretical and experimental characterization", J. Opt. Soc. Am. B **19**, 125–141 (2002) (cited on pages 7, 36).
[27] B. Auguié, J. L. Alonso-Gómez, A. Guerrero-Martínez, and L. M. Liz-Marzń, "Fingers Crossed: Optical Activity of a Chiral Dimer of Plasmonic Nanorods", J. Phys. Chem. Lett. **2**, 846–851 (2011) (cited on pages 7, 36, 37).
[28] M. Schäferling, D. Dregely, M. Hentschel, and H. Giessen, "Tailoring Enhanced Optical Chirality: Design Principles for Chiral Plasmonic Nanostructures", Phys. Rev. X **2**, 031010 (2012) (cited on pages 7, 36, 37, 98).

[29] L. Bougas, G. E. Katsoprinakis, W. von Klitzing, J. Sapirstein, and T. P. Rakitzis, "Cavity-Enhanced Parity-Nonconserving Optical Rotation in Metastable Xe and Hg", Phys. Rev. Lett. **108**, 210801 (2012) (cited on pages 7, 36).
[30] M. Hentschel, M. Schäferling, T. Weiss, N. Liu, and H. Giessen, "Three-Dimensional Chiral Plasmonic Oligomers", Nano Lett. **12**, 2542–2547 (2012) (cited on pages 7, 36, 37).
[31] V. K. Valev, J. J. Baumberg, C. Sibilia, and T. Verbiest, "Chirality and chiroptical effects in plasmonic nanostructures: fundamentals, recent progress, and outlook", Adv. Mater. **25**, 2517–2534 (2013) (cited on pages 7, 36, 37, 98).
[32] D. Patterson, M. Schnell, and J. M. Doyle, "Enantiomer-specific detection of chiral molecules via microwave spectroscopy", Nature **497**, 475–477 (2013) (cited on pages 7, 36).
[33] A. García-Etxarri and J. A. Dionne, "Surface-enhanced circular dichroism spectroscopy mediated by nonchiral nanoantennas", Phys. Rev. B **87**, 235409 (2013) (cited on pages 7, 36, 100).
[34] T. Wu, J. Ren, R. Wang, and X. Zhang, "Competition of Chiroptical Effect Caused by Nanostructure and Chiral Molecules", J. Phys. Chem. C **118**, 20529–20537 (2014) (cited on pages 7, 36, 37).
[35] L. Bougas, G. E. Katsoprinakis, W. von Klitzing, and T. P. Rakitzis, "Fundamentals of cavity-enhanced polarimetry for parity-nonconserving optical rotation measurements: Application to Xe, Hg, and I", Phys. Rev. A **89**, 052127 (2014) (cited on pages 7, 36).
[36] D. Sofikitis, L. Bougas, G. E. Katsoprinakis, A. K. Spiliotis, B. Loppinet, and T. P. Rakitzis, "Evanescent-wave and ambient chiral sensing by signal-reversing cavity ringdown polarimetry", Nature **514**, 76–79 (2014) (cited on pages 7, 36).
[37] S. Yoo and Q.-H. Park, "Chiral Light-Matter Interaction in Optical Resonators", Phys. Rev. Lett. **114**, 203003 (2015) (cited on pages 7, 36).
[38] M. L. Nesterov, X. Yin, M. Schäferling, H. Giessen, and T. Weiss, "The role of plasmon-generated near fields for enhanced circular dichroism spectroscopy", ACS Photonics **3**, 578–583 (2016) (cited on pages 7, 36, 37, 51, 100).
[39] M. Schäferling, "Chiral Nanophotonics: Chiral Optical Properties of Plasmonic Systems", Springer Series in Optical Sciences **205** (2016) (cited on pages 7, 36).
[40] R. P. Cameron, J. B. Götte, and S. M. Barnett, "Chiral rotational spectroscopy", Phys. Rev. A **94**, 032505 (2016) (cited on pages 7, 36).
[41] C.-S. Ho, A. Garcia-Etxarri, Y. Zhao, and J. Dionne, "Enhancing Enantioselective Absorption Using Dielectric Nanospheres", ACS Photonics **4**, 197–203 (2017) (cited on pages 7, 36).

[42] Y. Zhao, A. N. Askarpour, L. Sun, J. Shi, X. Li, and A. Alù, "Chirality detection of enantiomers using twisted optical metamaterials", Nat. Comm. **8**, 14180 (2017) (cited on pages 7, 36).

[43] A. Vázquez-Guardado and D. Chanda, "Superchiral Light Generation on Degenerate Achiral Surfaces", Phys. Rev. Lett. **120**, 137601 (2018) (cited on pages 7, 36).

[44] M. Hanifeh, M. Albooyeh, and F. Capolino, "Optimally Chiral Electromagnetic Fields: Helicity Density and Interaction of Structured Light with Nanoscale Matter", arXiv preprint arXiv:1809.04117 (2018) (cited on pages 7, 36).

[45] E. Mohammadi, K. L. Tsakmakidis, A. N. Askarpour, P. Dehkhoda, A. Tavakoli, and H. Altug, "Nanophotonic Platforms for Enhanced Chiral Sensing", ACS Photonics **5**, 2669–2675 (2018) (cited on pages 7, 36, 37, 51).

[46] L. V. Poulikakos, P. Thureja, A. Stollmann, E. De Leo, and D. J. Norris, "Chiral Light Design and Detection Inspired by Optical Antenna Theory", Nano Letters **18**, 4633–4640 (2018) (cited on pages 7, 36).

[47] J. García-Guirado, M. Svedendahl, J. Puigdollers, and R. Quidant, "Enantiomer-Selective Molecular Sensing Using Racemic Nanoplasmonic Arrays", Nano Lett. **18**, 6279–6285 (2018) (cited on pages 7, 36).

[48] K. A. Forbes and D. L. Andrews, "Enhanced optical activity using the orbital angular momentum of structured light", Phys. Rev. Research **1**, 033080 (2019) (cited on pages 7, 36).

[49] F. Graf, J. Feis, X. Garcia-Santiago, M. Wegener, C. Rockstuhl, and I. Fernandez-Corbaton, "Achiral, Helicity Preserving, and Resonant Structures for Enhanced Sensing of Chiral Molecules", ACS Photonics **6**, 482–491 (2019) (cited on pages 7, 36).

[50] J. Feis, D. Beutel, J. Köpfler, X. Garcia-Santiago, C. Rockstuhl, M. Wegener, and I. Fernandez-Corbaton, "Helicity-Preserving Optical Cavity Modes for Enhanced Sensing of Chiral Molecules", Phys. Rev. Lett. **124**, 033201 (2020) (cited on pages 7, 36).

[51] P. Scott, X. Garcia-Santiago, D. Beutel, C. Rockstuhl, M. Wegener, and I. Fernandez-Corbaton, "On enhanced sensing of chiral molecules in optical cavities", Applied Physics Reviews **7** (2020) (cited on pages 7, 8, 36, 41, 42, 44, 45, 52, 53).

[52] D. Ayuso, O. Neufeld, A. F. Ordonez, P. Decleva, G. Lerner, O. Cohen, M. Ivanov, and O. Smirnova, "Synthetic chiral light for efficient control of chiral light-matter interaction", Nature Photonics **13**, 866–871 (2019) (cited on pages 7, 36).

[53] M. L. Solomon, J. Hu, M. Lawrence, A. García-Etxarri, and J. A. Dionne, "Enantiospecific Optical Enhancement of Chiral Sensing and Separation with Dielectric Metasurfaces", ACS Photonics **6**, 43–49 (2019) (cited on pages 7, 36).

[54] J. Garcia-Guirado, M. Svedendahl, J. Puigdollers, and R. Quidant, "Enhanced Chiral Sensing with Dielectric Nanoresonators", Nano Letters **20**, 585–591 (2020) (cited on pages 7, 36).
[55] S. Droulias and L. Bougas, "Absolute Chiral Sensing in Dielectric Metasurfaces Using Signal Reversals", Nano Letters, 10.1021/acs.nanolett.0c01938 (2020) (cited on pages 7, 36).
[56] B. Semnani, J. Flannery, R. Al Maruf, and M. Bajcsy, "Spin-preserving chiral photonic crystal mirror", Light: Science & Applications **9**, 23 (2020) (cited on pages 7, 36).
[57] J. Lasa-Alonso, D. R. Abujetas, A. Nodar, J. A. Dionne, J. J. Saenz, G. Molina-Terriza, J. Aizpurua, and A. Garcia-Etxarri, "Surface-Enhanced Circular Dichroism spectroscopy on periodic dual nanostructures", arXiv preprint arXiv:2003.07653 (2020) (cited on pages 7, 36).
[58] T. Iida, A. Ishikawa, T. Tanaka, A. Muranaka, M. Uchiyama, Y. Hayashi, and K. Tsuruta, "Super-chiral vibrational spectroscopy with metasurfaces for high-sensitive identification of alanine enantiomers", Applied Physics Letters **117**, 101103 (2020) (cited on pages 7, 36).
[59] M. L. Solomon, J. M. Abendroth, L. V. Poulikakos, J. Hu, and J. A. Dionne, "Fluorescence-Detected Circular Dichroism of a Chiral Molecular Monolayer with Dielectric Metasurfaces", arXiv preprint arXiv:2008.11270 (2020) (cited on pages 7, 36).
[60] F. Wang, X. Wang, X. Lu, and C. Huang, "Nanophotonic Enhanced Chiral Sensing and Its Biomedical Applications", Biosensors **14** (2024) (cited on pages 7, 36).
[61] J. Garcia-Guirado, M. Svedendahl, J. Puigdollers, and R. Quidant, "Enhanced chiral sensing with dielectric nanoresonators", Nano letters **20**, 585–591 (2019) (cited on pages 7, 36, 51).
[62] X. Tian, Y. Bai, T. Fu, and Z. Zhang, "Enhanced chiral sensing by optical whispering gallery mode microresonator", Optics Express **32**, 31034–31042 (2024) (cited on pages 7, 37).
[63] J. Ceramella, D. Iacopetta, A. Franchini, M. De Luca, C. Saturnino, I. Andreu, M. S. Sinicropi, and A. Catalano, "A look at the importance of chirality in drug activity: Some significative examples", Applied Sciences **12**, 10909 (2022) (cited on page 8).
[64] F. Graf, J. Feis, X. Garcia-Santiago, M. Wegener, C. Rockstuhl, and I. Fernandez-Corbaton, "Achiral, helicity preserving, and resonant structures for enhanced sensing of chiral molecules", ACS Photonics **6**, 482–491 (2019) (cited on pages 8, 36, 43, 98, 100).
[65] J. Feis, D. Beutel, J. Köpfler, X. Garcia-Santiago, C. Rockstuhl, M. Wegener, and I. Fernandez-Corbaton, "Helicity-preserving optical cavity modes for enhanced sensing of chiral molecules", Physical review letters **124**, 033201 (2020) (cited on pages 8, 40–43, 45).

[66] D. Beutel, P. Scott, M. Wegener, C. Rockstuhl, and I. Fernandez-Corbaton, "Enhancing the optical rotation of chiral molecules using helicity preserving all-dielectric metasurfaces", Applied Physics Letters **118** (2021) (cited on pages 8, 100).
[67] F. G. Smith, T. A. King, and D. Wilkins, *Optics and photonics: an introduction* (John Wiley & Sons, 2007) (cited on page 12).
[68] B. E. Saleh and M. C. Teich, *Fundamentals of photonics* (john Wiley & sons, 2019) (cited on page 12).
[69] E. Hecht, *Optik* (Walter de Gruyter GmbH & Co KG, 2023) (cited on pages 12, 20, 22).
[70] J. C. Maxwell, "VIII. A dynamical theory of the electromagnetic field", Philosophical transactions of the Royal Society of London, 459–512 (1865) (cited on page 12).
[71] O. Heaviside, *Electromagnetic theory*, Vol. 237 (American Mathematical Soc., 2003) (cited on page 12).
[72] J. D. Jackson, *Classical electrodynamics* (John Wiley & Sons, 2021) (cited on pages 16, 22, 33, 39, 40, 43).
[73] Y. Tang and A. E. Cohen, "Optical chirality and its interaction with matter", Physical review letters **104**, 163901 (2010) (cited on page 21).
[74] J. W. Goodman, *Introduction to Fourier optics* (Roberts and Company publishers, 2005) (cited on page 22).
[75] J. Patterson and B. Bailey, *Solid-state physics: introduction to the theory* (Springer Science & Business Media, 2007) (cited on page 22).
[76] J. L. Amorós, *The laue method* (Elsevier, 2012) (cited on page 24).
[77] W. H. Bragg, "X-rays and crystalline structure", Science **40**, 795–802 (1914) (cited on page 25).
[78] I. Fernandez-Corbaton, X. Zambrana-Puyalto, N. Tischler, X. Vidal, M. L. Juan, and G. Molina-Terriza, "Electromagnetic Duality Symmetry and Helicity Conservation for the Macroscopic Maxwell's Equations", Physical review letters **111**, 060401 (2013) (cited on page 26).
[79] I. Fernandez-Corbaton, *Duality Symmetry* (MDPI, 2020) (cited on page 26).
[80] I. Fernandez-Corbaton, "Forward and backward helicity scattering coefficients for systems with discrete rotational symmetry", Optics express **21**, 29885–29893 (2013) (cited on pages 26–28).
[81] M. Decker, R. Zhao, C. Soukoulis, S. Linden, and M. Wegener, "Twisted split-ring-resonator photonic metamaterial with huge optical activity", Optics letters **35**, 1593–1595 (2010) (cited on page 28).
[82] J. Kaschke, J. K. Gansel, and M. Wegener, "On metamaterial circular polarizers based on metal N-helices", Optics express **20**, 26012–26020 (2012) (cited on page 28).
[83] I. Lindell, A. Sihvola, S. Tretyakov, and A. J. Viitanen, *Electromagnetic waves in chiral and bi-isotropic media* (Artech House, 1994) (cited on pages 29, 51).

[84] J. Lekner, "Theory of reflection", Springer Series on Atomic, Optical, and Plasma Physics **87** (2016) (cited on page 29).
[85] L. D. Barron, *Molecular Light Scattering and Optical Activity*, 2nd ed. (Cambridge University Press, Nov. 2004) (cited on page 31).
[86] M. Hesse, H. Meier, and B. Zeeh, *Spektroskopische Methoden in der organischen Chemie* (Georg Thieme Verlag, 2005) (cited on page 32).
[87] M. Nelson, J. Mulloor, B. Lang, M. Ishikawa, Y. Kondo, and B. Toman, "Certification of Standard Reference Material® 17g: Sucrose Optical Rotation", National Institue of Standards and Technology (2022) (cited on page 32).
[88] V. Lucarini, J. J. Saarinen, K.-E. Peiponen, and E. M. Vartiainen, *Kramers-Kronig relations in optical materials research*, Vol. 110 (Springer Science & Business Media, 2005) (cited on page 33).
[89] M. Schäferling, "Chiral nanophotonics", Springer Series in Optical Sciences **205**, 159 (2017) (cited on page 37).
[90] E. Plum and N. I. Zheludev, "Chiral mirrors", Applied Physics Letters **106** (2015) (cited on page 38).
[91] S. Wang and R. Magnusson, "Theory and applications of guided-mode resonance filters", Applied optics **32**, 2606–2613 (1993) (cited on page 39).
[92] A. Watanabe, S. Teranishi, K. Ozawa, A. Taniguchi, J. Inoue, K. Kitntaka, and S. Ura, "Cavity-Resonator-Integrated Guided-Mode-Resonance Mirrors for Hybrid Integration of Wavelength-Multiplexed Light Source", in 2023 IEEE 73rd Electronic Components and Technology Conference (ECTC) (IEEE, 2023), pp. 761–766 (cited on page 39).
[93] H. M. H. AlAameri and M. Shokooh-Saremi, "Guided-mode resonance sensors with high sensitivity and asymmetric structures", Journal of Nanophotonics **18**, 016005–016005 (2024) (cited on page 39).
[94] I. Fernandez-Corbaton and G. Molina-Terriza, "Role of duality symmetry in transformation optics", Phys. Rev. B **88**, 085111 (2013) (cited on page 41).
[95] N. Stefanou, V. Yannopapas, and A. Modinos, "MULTEM 2: A new version of the program for transmission and band-structure calculations of photonic crystals", Computer physics communications **132**, 189–196 (2000) (cited on page 43).
[96] T. G. Mackay and A. Lakhtakia, *The transfer-matrix method in electromagnetics and optics* (Springer Nature, 2022) (cited on page 43).
[97] S. Burger, L. Zschiedrich, J. Pomplun, and F. Schmidt, "JCMsuite: An adaptive FEM solver for precise simulations in nano-optics", in Integrated Photonics and Nanophotonics Research and Applications (Optica Publishing Group, 2008), ITuE4 (cited on page 43).
[98] X. G. Santiago, M. Hammerschmidt, S. Burger, C. Rockstuhl, I. Fernandez-Corbaton, and L. Zschiedrich, "Decomposition of scattered electromagnetic fields into vector spherical wave functions on surfaces with general shapes", Physical Review B **99**, 045406 (2019) (cited on page 43).

[99] C. J. Chang-Hasnain and W. Yang, "High-contrast gratings for integrated optoelectronics", Adv. Opt. Photonics **4**, 379–440 (2012) (cited on page 46).
[100] M. Nyman, X. Garcia-Santiago, M. Krstić, L. Materne, I. Fernandez-Corbaton, C. Holzer, P. Scott, M. Wegener, W. Klopper, and C. Rockstuhl, "A digital twin for a chiral sensing platform", Laser & Photonics Reviews, 2300967 (2024) (cited on pages 47, 50, 54, 100).
[101] I. H. Malitson, "A redetermination of some optical properties of calcium fluoride", Applied Optics **2**, 1103–1107 (1963) (cited on pages 47, 58).
[102] H. Li, "Refractive index of alkaline earth halides and its wavelength and temperature derivatives", Journal of Physical and Chemical Reference Data **9**, 161–290 (1980) (cited on page 47).
[103] Korth Kristalle, *Calcium Fluoride Windows*, https://www.korth.de/en/materials/, [Online; accessed 23-11-2024], 2021 (cited on page 47).
[104] P. Pal and S. Chandra, "RF sputtered silicon for MEMS", Journal of Micromechanics and Microengineering **15**, 1536 (2005) (cited on page 47).
[105] G. Zhao, T. Zhang, T. Zhang, J. Wang, and G. Han, "Electrical and optical properties of titanium nitride coatings prepared by atmospheric pressure chemical vapor deposition", Journal of non-crystalline solids **354**, 1272–1275 (2008) (cited on page 47).
[106] R. Rodríguez-López, G. Soto-Valle, R. Sanginés, N. Abundiz-Cisneros, J. Águila-Muñoz, J. Cruz, and R. Machorro-Mejía, "Study of deposition parameters of reactive-sputtered Si3N4 thin films by optical emission spectroscopy", Thin Solid Films **754**, 139313 (2022) (cited on page 47).
[107] B. Liu, Q. Zhao, and P. Zheng, "Optical properties of amorphous silicon thin films fabricated by RF magnetron sputtering", in Photonics and Optoelectronics Meetings (POEM) 2008: Optoelectronic Devices and Integration, Vol. 7279 (SPIE, 2009), pp. 491–501 (cited on page 47).
[108] E. Márquez, E. Blanco, C. García-Vázquez, J. Díaz, and E. Saugar, "Spectroscopic ellipsometry study of non-hydrogenated fully amorphous silicon films deposited by room-temperature radio-frequency magnetron sputtering on glass: Influence of the argon pressure", Journal of Non-Crystalline Solids **547**, 120305 (2020) (cited on page 47).
[109] P. Nestler and C. A. Helm, "Determination of refractive index and layer thickness of nm-thin films via ellipsometry", Optics Express **25**, 27077–27085 (2017) (cited on page 47).
[110] D. R. Hermann, G. Ramer, M. Kitzler-Zeiler, and B. Lendl, "Quantum cascade laser-based vibrational circular dichroism augmented by a balanced detection scheme", Analytical Chemistry **94**, 10384–10390 (2022) (cited on page 48).
[111] L. Pandiscia, *Measurement of Vibrational Circular Dichroism spectra using the FVS-6000*, Application note 260-PO-0224, JASCO INTERNATIONAL CO., LTD. (Apr. 2011) (cited on page 48).

[112] V. P. Nicu, E. J. Baerends, and P. L. Polavarapu, "Understanding solvent effects in vibrational circular dichroism spectra:[1, 1'-binaphthalene]-2, 2'-diol in dichloromethane, acetonitrile, and dimethyl sulfoxide solvents", The Journal of Physical Chemistry A **116**, 8366–8373 (2012) (cited on page 48).
[113] M. R. Poopari, Z. Dezhahang, and Y. Xu, "A comparative VCD study of methyl mandelate in methanol, dimethyl sulfoxide, and chloroform: explicit and implicit solvation models", Physical Chemistry Chemical Physics **15**, 1655–1665 (2013) (cited on page 48).
[114] K. Le Barbu-Debus, A. Scherrer, A. Bouchet, D. Sebastiani, R. Vuilleumier, and A. Zehnacker, "Effect of puckering motion and hydrogen bond formation on the vibrational circular dichroism spectrum of a flexible molecule: the case of (S)-1-indanol", Physical Chemistry Chemical Physics **20**, 14635–14646 (2018) (cited on page 48).
[115] N. L. McNiven and R. Court, "Infrared Spectra of Deuterated Solvents", Applied Spectroscopy **24**, 296–300 (1970) (cited on page 49).
[116] J. García-Guirado, M. Svedendahl, J. Puigdollers, and R. Quidant, "Enantiomer-selective molecular sensing using racemic nanoplasmonic arrays", Nano letters **18**, 6279–6285 (2018) (cited on page 51).
[117] I. Sersic, C. Tuambilangana, T. Kampfrath, and A. F. Koenderink, "Magnetoelectric point scattering theory for metamaterial scatterers", Phys. Rev. B **83**, 245102 (2011) (cited on page 51).
[118] S. Ghosal, J. L. Ebert, and S. A. Self, "The infrared refractive indices of CHBr3, CCl4 and CS2", Infrared physics **34**, 621–628 (1993) (cited on page 58).
[119] J. E. Bertie, Z. Lan, R. N. Jones, and Y. Apelblat, "Infrared intensities of liquids XVIII: Accurate optical constants and molar absorption coefficients between 6500 and 800 cm- 1 of dichloromethane at 25 C, from spectra recorded in several laboratories", Applied spectroscopy **49**, 840–851 (1995) (cited on page 58).
[120] T. L. Myers, R. G. Tonkyn, T. O. Danby, M. S. Taubman, B. E. Bernacki, J. C. Birnbaum, S. W. Sharpe, and T. J. Johnson, "Accurate measurement of the optical constants n and k for a series of 57 inorganic and organic liquids for optical modeling and detection", Applied spectroscopy **72**, 535–550 (2018) (cited on page 58).
[121] P. Waters, "The effects of moisture on thin film delamination and adhesion", (2005) (cited on page 59).
[122] K. Racka-Szmidt, B. Stonio, J. Żelazko, M. Filipiak, and M. Sochacki, "A review: Inductively coupled plasma reactive ion etching of silicon carbide", Materials **15**, 123 (2021) (cited on page 65).
[123] D. L. Olynick, J. A. Liddle, and I. W. Rangelow, "Profile evolution of Cr masked features undergoing HBr-inductively coupled plasma etching for use in 25nm silicon nanoimprint templates", Journal of Vacuum Science

& Technology B: Microelectronics and Nanometer Structures Processing, Measurement, and Phenomena **23**, 2073–2077 (2005) (cited on page 65).

[124] A. L. Goodyear, S. Mackenzie, D. L. Olynick, and E. H. Anderson, "High resolution inductively coupled plasma etching of 30 nm lines and spaces in tungsten and silicon", Journal of Vacuum Science & Technology B: Microelectronics and Nanometer Structures Processing, Measurement, and Phenomena **18**, 3471–3475 (2000) (cited on page 65).

[125] N. Atthi, O.-u. Nimittrakoolchai, W. Jeamsaksiri, S. Supothina, C. Hruanun, and A. Poyai, "Study of optimization condition for spin coating of the photoresist film on rectangular substrate by Taguchi design of an experiment.", Songklanakarin Journal of Science & Technology **31** (2009) (cited on page 67).

[126] L. A. Nafie and M. Diem, "Theory of high frequency differential interferometry: application to the measurement of infrared circular and linear dichroism via Fourier transform spectroscopy", Applied Spectroscopy **33**, 130–135 (1979) (cited on page 72).

[127] L. A. Nafie, M. Diem, and D. W. Vidrine, "Fourier transform infrared vibrational circular dichroism", Journal of the American Chemical Society **101**, 496–498 (1979) (cited on page 72).

[128] J. Cheng, L. Nafie, and P. Stephens, "Polarization scrambling using a photoelastic modulator: Application to circular dichroism measurement", JOSA **65**, 1031–1035 (1975) (cited on page 74).

[129] E. D. Lipp, C. G. Zimba, and L. A. Nafie, "Vibrational circular dichroism in the mid-infrared using Fourier transform spectroscopy", Chemical Physics Letters **90**, 1–5 (1982) (cited on page 74).

[130] A. von Weber, D. C. Hooper, M. Jakob, V. K. Valev, A. Kartouzian, and U. Heiz, "Circular Dichroism and Isotropy–Polarity Reversal of Ellipticity in Molecular Films of 1, 1'-Bi-2-Naphtol", ChemPhysChem **20**, 62–69 (2019) (cited on page 80).

[131] G. Albano, G. Pescitelli, and L. Di Bari, "Chiroptical properties in thin films of π-conjugated systems", Chemical reviews **120**, 10145–10243 (2020) (cited on page 80).

[132] I. Toftul, P. Tonkaev, K. Koshelev, F. Lai, Q. Song, M. Gorkunov, and Y. Kivshar, "Chiral dichroism in resonant metasurfaces with monoclinic lattices", Physical Review Letters **133**, 216901 (2024) (cited on page 94).

[133] S. Okazaki, "High resolution optical lithography or high throughput electron beam lithography: The technical struggle from the micro to the nanofabrication evolution", Microelectronic Engineering **133**, 23–35 (2015) (cited on page 95).

[134] Y.-W. Chang, R.-G. Liu, and S.-Y. Fang, "EUV and e-beam manufacturability: Challenges and solutions", in Proceedings of the 52nd Annual Design Automation Conference (2015), pp. 1–6 (cited on page 95).

[135] G.-Q. Lin, J.-G. Zhang, and J.-F. Cheng, "Overview of chirality and chiral drugs", Chiral drugs: chemistry and biological action, 3–28 (2011) (cited on page 99).
[136] P. L. Polavarapu and J. He, *Peer reviewed: chiral analysis using mid-IR vibrational CD spectroscopy*, 2004 (cited on page 99).
[137] K. Voronin, A. S. Taradin, M. V. Gorkunov, and D. G. Baranov, "Single-handedness chiral optical cavities", Acs Photonics **9**, 2652–2659 (2022) (cited on page 100).
[138] N. S. Baßler, A. Aiello, K. P. Schmidt, C. Genes, and M. Reitz, "Metasurface-based hybrid optical cavities for chiral sensing", Physical Review Letters **132**, 043602 (2024) (cited on page 100).
[139] R. R. Riso, L. Grazioli, E. Ronca, T. Giovannini, and H. Koch, "Strong coupling in chiral cavities: nonperturbative framework for enantiomer discrimination", Physical Review X **13**, 031002 (2023) (cited on page 100).
[140] I. Staude, A. E. Miroshnichenko, M. Decker, N. T. Fofang, S. Liu, E. Gonzales, J. Dominguez, T. S. Luk, D. N. Neshev, I. Brener, et al., "Tailoring directional scattering through magnetic and electric resonances in subwavelength silicon nanodisks", ACS nano **7**, 7824–7832 (2013) (cited on page 100).
[141] A. B. Evlyukhin, C. Reinhardt, and B. N. Chichkov, "Multipole light scattering by nonspherical nanoparticles in the discrete dipole approximation", Physical Review B—Condensed Matter and Materials Physics **84**, 235429 (2011) (cited on page 100).
[142] V. R. Manfrinato, L. Zhang, D. Su, H. Duan, R. G. Hobbs, E. A. Stach, and K. K. Berggren, "Resolution limits of electron-beam lithography toward the atomic scale", Nano letters **13**, 1555–1558 (2013) (cited on page 100).
[143] L. R. Harriott, "Limits of lithography", Proceedings of the IEEE **89**, 366–374 (2001) (cited on page 100).

Acknowledgments

I would like to express my gratitude and thanks to everyone that contributed to the successful completion of my thesis. Without the help and support from countless people, this would not of been possible.

First and foremost, I would like to thank Prof. Dr. Martin Wegener for granting me opportunity to undertake this doctoral project I especially thank him for his outstanding supervision and support at every part of this project, enabling me to continually improve and grow as a researcher.

I extend the thanks to Prof. Dr. Carsten Rockstuhl, for agreeing to be the co-referee of this project. His insightful discussions on the project have been instrumental in shaping the outcomes of my research.

The project stemmed from a collaboration, and I am deeply grateful to the theoretical team whose groundwork laid the foundation for my experimental studies. I want to express my gratitude to Dr. Ivan Fernandez-Corbaton, his vast theoretical expertise and for the fruitful discussions that greatly expanded my understanding of the subject. I extend these thanks to Dr. Benedikt Zerulla and Dr. Markus Nyman for their significant contributions to the theoretical calculations and providing useful insights to overcome various challenges that were faced.

The circular dichroism measurements were made possible thanks to Prof. Dr. Thomas Bürgi, who welcomed me into his group for multiple visits to conduct these experiments. I thank both him and Dr. Ariel Francis Pérez Mellor for their time and sharing their expert knowledge. I sincerely appreciate the time and care that Ariel took during both of my visits. He insured that my time there was productive as possible and I thoroughly enjoyed the time I had conducting experiments there.

I next thank Lilyn Gao, whose assistance as a HiWi intern was immensely beneficial in advancing several aspects of this project. I hope the work we accomplished together, also helped her in her Master's and doctoral projects.

The fabrication processes essential to this project were carried out in the cleanroom environment of the Nanostructure Service Laboratory. I want to express my gratitude and thanks to Prof. Dr Gernot Goll, Lucas Radtke and Dr. Aina

Quintilla, for their support and expertise, which proved indispensable for all the questions I had regarding the cleanroom processes.

I further want to show appreciation for the many people in the administrative side at the Institute of Applied Physics. I thank Petra Bauer, Gloria Zanda, Monika Brenkman, Ursula Mösle, and Claudia Alaya for their time to manage all of the paperwork required throughout my time here. The working group technician, Johann Westhauser, who was greatly helpful when completing purchases for the items that I needed and for the tremendous help in the design of the microfluidic cavity that was detrimental for my research. To the mechanical workshop, I also want to show my gratitude, who under the leading of Maik Nothdurft, who was the successor to Frank Landhäuser, proved invaluable to my project. They fabricated many of the custom required parts for the microfluidic chamber, that I could not of completed my work without. I also appreciate the many times that they agreed to clean the parts of the sputter coater that I rigorously used. Finally, within the institute, I appreciate the expertise of the electronics workshop, piloted by Michael Hippe, Helmut Lay and Werner Gilde, who always kept the technical side running smoothly.

I am deeply thankful to the Hector Fellow Academy for funding this PhD project. The annual events, such as the symposium, provided me with opportunities to gain insights into a wide range of scientific fields and to connect with fellow researchers. I also extend my appreciation to the International Department for their administrative support and for organizing these enriching events.

This dissertation benefitted greatly thanks to the people who kindly agreed to proofread what I have written, for which I am thankful for their time. I also want to say thanks to every member of the research group, of which I had the pleasure to be a apart of. The friendly and enjoyable atmosphere made my time here truly memorable.

I bring this to a close, by showing my gratefulness to my friends and family, of which many have taken the time to visit me during my time here. Especially to my partner, Kiana, who has been nothing but supportive and also agreed to join me on this journey and experience life in another country. Her support throughout has been undoubtedly invaluable and I look forward to embarking on the next chapter in our lives together.